TECHNISCHE UNIVERSITÄT DRESDEN

Final Report of the BMWi Joint Research Project

Geochemical retention of radionuclides on cement alteration phases (GRaZ)

SUBPROJECT

Interaction of trivalent lanthanides/actinides with cement additives and calcium silicate hydrate phases

F. Taube, M. Acker, T. Zimmermann, B. Drobot, S. Taut, T. Stumpf

Technische Universität Dresden
Sachgebiet Strahlenschutz und Professur für Radioökologie/Radiochemie
01062 Dresden
Germany

DRESDEN concept

Das diesem Bericht zugrundeliegende Vorhaben wurde mit Mitteln des Bundesministeriums für Wirtschaft und Energie unter dem Förderkennzeichen 02E11415G gefördert. Die Verantwortung für den Inhalt dieser Veröffentlichung liegt bei den Autoren.

Verbundvorhaben

Geochemische Radionuklidrückhaltung an Zementalterationsphasen (GRaZ)

Teilprojekt G

Interaction of trivalent lanthanides/actinides with cement additives and calcium silicate hydrate phases

Gefördert durch:

Bundesministerium für Wirtschaft und Energie

aufgrund eines Beschlusses des Deutschen Bundestages

FZK 02E11415G

PTKA
Projektträger Karlsruhe
im Karlsruher Institut für Technologie

Autoren

Franziska Taube, Margret Acker, Thomas Zimmermann, Björn Drobot, Steffen Taut, Thorsten Stumpf

Ausführende Institution

TU Dresden
Bereich für Mathematik und Naturwissenschaften
Fachbereich Chemie und Lebensmittelchemie
Professur für Radioökologie und Radiochemie

01062 Dresden

TU Dresden
Sachgebiet Strahlenschutz

01062 Dresden

Content

List of Abbreviations

ACW	artificial cement pore water
An	actinide
C/A	calcium to aluminate ratio
C/S	calcium to silica ratio
CAH	calcium aluminate hydrate
CSH	calcium silicate hydrate
DFT	density functional theory
DP	differential power (ITC)
DW	Debye-Waller Factor
EXAFS	extended x-ray absorption fine structure
FT	Fourier transformation
HCP	hardened cement paste
HOMO	highest occupied molecular orbital
HSAB	principle of hard and soft acids and bases and bases
HZDR	Helmholtz-Zentrum Dresden-Rossendorf
ICCD	intensified charge-coupled device
I_m / I_M	molal/ molar ionic strength
IR	infra-red
ITC	isothermal titration micro-calorimetry
K_d	distribution coefficient
Lac	lactate
LDH	layered double hydroxides
Ln	lanthanide
log β	stability constant/ complex formation constant
LUMO	lowest unoccupied molecular orbital
Mal	malate
NEA-TDB	Thermochemical database of the Nuclear Energy Agency
NIST	Nationales Institut of standards and technology
NMR	nuclear magnetic resonance
OECD	Organisation for Economic Cooperation and Development
OPO	optical parametric oscillator
Oxa	oxalate
PA	polyacrylate
PARAFAC	parallel factor analysis
PCA	principle component analysis
PCE	polycarboxylate-ether based superplasticizer/polycarboxylate-ether
R	interatomic bond distance

RN	radionuclide
SANS	small-angle neutron scattering
SIT	specific ion interaction theory
s/l	solid-liquid ratio
SP	superplasticizer
TEM	transmission electron microscopy
TRLFS	time-resolved laser-induced fluorescence spectroscopy
TOC	total organic carbon
UV	ultraviolet
Vis	visible
XANES	X-ray absorption near-edge structure
XRD	X-ray diffraction
Z	atomic number, nuclear charge number

Abstract

For the safety assessment of a potential deep geological repository for heat producing high-level radioactive waste, a detailed understanding of the near field processes in the radionuclide-cement interaction is required.
The understanding of sorption and retention mechanisms of actinides on cement phases under the prevailing conditions in the near-field of a repository, such as highly alkaline pH values, medium to higher ionic strengths (relevant for German clay rocks and salt domes), higher temperatures and the influence of organic compounds is a major focus of the joint research project “Geochemical retention of radionuclides on cement alteration phases " (GRaZ).
This report focusses on the retention of trivalent actinides (An(III)) and lanthanides (Ln(III)) on calcium silicate hydrate phases (CSH phases) in the presence of malate (salt of 2-hydroxysuccinic acid). Malate is a typical representative of cement additives based on hydroxycarboxylates which act as retarders, besides tartrate, citrate and gluconate. CSH phases are the main components of hardened cement paste and they are mainly responsible for the actinide retention.
The experimental studies in the binary systems An(III)/Ln(III)-Ligand, An(III)/Ln(III)-CSH and ligand-CSH phase as well as in the ternary system An(III)/Ln(III)-Ligand-CSH phase aim at an improved and extended process understanding of the influence of cement additives on the An(III)/Ln(III)-retention at cement phases.

The present investigations show: 1) Hydroxycarboxylates with medium complexation strengths (example malate, $\beta_1^0 \sim 6$) have no influence on the quantitative An(III)/Ln(III) retention on CSH phases. The presence of such ligands does not result in an increased mobilization of An(III)/Ln(III). 2) Malate shows a Ca^{2+} mediated weak *outer sphere* sorption, while the An(III)/Ln(III) show a nearly quantitative sorption (*inner sphere* sorption) and an incorporation into the CSH phases. 3) The sorption and incorporation processes of the An(III)/Ln(III) and the ligand on/in the CSH phases occur independently of each other. The structure and crystallinity of the CSH phases are clearly influenced by the presence of the ligand. 4) Polycarboxylate-ethers form medium strength 1:1 complexes with An(III)/Ln(III) ($K_1 \sim 4.5$ bis 5.5, I = 0.1 m). Their complex strength is comparable with similar An(III)/Ln(III) complexes with naturally occurring polycarboxylates like humic substances .5) The complexation reactions of An(III)/Ln(III) with (hydroxy)carboxylates and polycarboxylate- ethers are mainly endothermic and entropy driven. The enthalpy decreases with increasing ionic strength. It seems that at higher ionic strengths the complex formation reactions are less favored by higher temperatures.

This project was part of the BMWi joint research project GRaZ between the Karlsruher Institut für Technologie (Institut für Nukleare Entsorgung), Johannes Gutenberg-Universität Mainz (Institut für Kernchemie), Helmholtz-Zentrum Dresden-Rossendorf (Institut für Ressourcenökologie), Universität des Saarlandes (Institut für Anorganische Festkörperchemie), Technische Universität Dresden (Professur für Radioökologie und Radiochemie, Sachgebiet Strahlenschutz), Technische Universität

München (Fachgebiet Theoretische Chemie), Universität Potsdam (Institut für Chemie-Physikalische Chemie) and Ruprecht-Karls-Universität Heidelberg (Physikalisch-chemisches Institut).

Zusammenfassung

Für die Beurteilung der Sicherheit eines potentiellen Tiefenlagers für wärmeproduzierende hochradioaktive Abfälle ist ein detailliertes Prozessverständnis der im Nahfeld auftretenden Radionuklid-Zementwechselwirkungen erforderlich. Die Aufklärung von Sorptions- und Retentionsmechanismen von Actiniden an Zementphasen unter den im Nahfeld eines Endlagers vorherrschenden Bedingungen, wie hochalkalische pH-Werte, mittlere bis hohe Ionenstärken (besonders relevant für deutsche Tongesteine und Salzstöcke), höhere Temperaturen sowie bedeutende Gehalte von im Wirtsgestein vorliegenden organischen Verbindungen ist eine wesentliche Zielstellung des Verbundprojektes „Geochemische Radionuklidrückhaltung an Zementalterationsphasen“ (GRaZ).

Im Fokus dieses Berichtes stehen Untersuchungen zur Retention von dreiwertigen Actiniden (An(III)) und Lanthaniden (Ln(III)) an Calcium-Silikat-Hydratphasen (CSH-Phasen) in Gegenwart von Malat (Salz der 2-Hydroxybernsteinsäure). Malat ist (neben Tartrat, Citrat und Gluconat) ein typischer Vertreter von Zementadditiven auf Basis von Hydroxycarboxylaten, die als Erstarrungsverzöger wirken. CSH-Phasen sind die Hauptkomponenten von erhärtetem Zementstein und im Wesentlichen verantwortlich für die Actinidenretention.

Die experimentellen Studien in den binären Systemen An(III)/Ln(III)-Ligand, An(III)/Ln(III)-CSH und Ligand-CSH-Phase sowie im ternären System An(III)/Ln(III)-Ligand- CSH-Phase zielen auf ein verbessertes und erweitertes Prozessverständnis zum Einfluss von Zementadditiven auf die An(III)/Ln(III)-Rückhaltung an Zementphasen ab.

Die vorliegenden Untersuchungen zeigen: 1) Hydroxycarboxylate mit mittleren Komplexierungsstärken (Beispiel Malat, $\beta_1^0 \sim 6$) haben keinen Einfluss auf die quantitative An(III)/Ln(III)-Rückhaltung an CSH-Phasen. Die Anwesenheit von solchen Liganden führt nicht zu einer erhöhten Mobilisierung der An(III)/Ln(III). 2) Malat zeigt eine Ca^{2+} vermittelte schwache, *outer-sphere* Sorption, während An(III)/Ln(III) eine nahezu quantitative Sorption (*inner-sphere* Sorption) aufweisen und dabei strukturell in die CSH-Phasen eingebaut werden. 3) Die Sorption und Inkorporation der An(III)/ Ln(III) und des Liganden an/in die CSH-Phasen erfolgen unabhängig voneinander. Die Struktur und Kristallinität der CSH-Phasen werden durch die Anwesenheit des Liganden deutlich beeinflusst. 4) Polycarboxylatether bilden mittelstarke 1:1 Komplexe mit An(III)/Ln(III) ($K_1 \sim 4.5$ bis 5.5, I = 0.1 m). Deren Komplexstärke ist vergleichbar mit An(III)/Ln(III)-Komplexen mit natürlich vorkommenden Polycarboxylaten, z.B. Huminstoffen. 5) Die Komplexierungsreaktionen von An(III)/Ln(III) mit (Hydroxy)carboxylaten und Polycarboxylatethern verlaufen überwiegend endotherm und entropiegetrieben. Die Enthalpie nimmt mit zunehmender Ionenstärke ab. Es scheint, dass bei höheren Ionenstärken die Komplexbildungsreaktionen durch höhere Temperaturen weniger begünstigt werden.

Dieses Projekt war Teil des BMWi-Verbundprojektes GRaZ zwischen den folgenden Institutionen: Karlsruher Institut für Technologie (Institut für Nukleare Entsorgung), Johannes Gutenberg-Universität Mainz (Institut für Kernchemie), Helmholtz-Zentrum Dresden-Rossendorf (Institut für Ressourcenökologie), Universität des Saarlandes (Institut für Anorganische Festkörperchemie), Technische Universität Dresden (Professur für Radioökologie und Radiochemie, Sachgebiet Strahlenschutz), Tech-

nische Universität München (Fachgebiet Theoretische Chemie), Universität Potsdam (Institut für Chemie-Physikalische Chemie) und Ruprecht-Karls-Universität Heidelberg (Physikalisch-chemisches Institut).

1 Introduction and objective

Since passing the german law „Gesetz zur Suche und Auswahl eines Standortes für ein Endlager für hochradioaktive Abfälle (Standortauswahlgesetz - StandAG) “ in 2013, the search for a safe repository site for heat-generating high-level radioactive waste has been regulated by law.[1] The safe storage of the nuclear waste produced by nuclear power reactors, which will contain about 10,300 tonnes of heavy metal in the form of irradiated fuel elements until 2022, has to be guaranteed for 1 million years in deep geological formations.[2,3] The safety assessment of a deep geological repository for radioactive waste requires sciences-based data on both the retention of radionuclides in the near-field of the repository and a mechanistic understanding of the relevant processes.

The NORD site model for a possible repository in Northern Germany with clay as host rock developed within the project AnSichT[4] includes the use of concrete and bentonite in the geotechnical barrier around the storage containers. Cement is the binding agent of concrete. The Portland cement commonly used today consists of limestone, clay, sand and iron ore, which are burned to cement clinker and then harden by hydration into cement stone. Calcium silicate hydrates (CSH, $m\mathrm{CaO}\cdot\mathrm{SiO_2}\cdot n\mathrm{H_2O}$) form the main phase of the hardened cement paste with up to 70 weight% and are responsible for the hardness and compressive strength of the concrete.[5,6,7] The structure of CSH phases can be described as a layer structure of CaO-polyhedra and $\mathrm{SiO_2}$-tetrahedra (see *Dreierkette-Modell*[8], chapter 2.1.1). Cement also contains aluminum oxide, iron oxide and sulphate as essential additional constituents. This results in the formation of calcium aluminate hydrate phases (CAH, $m\mathrm{CaO}\cdot\mathrm{AlO_4}\cdot n\mathrm{H_2O}$), whereby the CaO-rich compound, the stable tetracalcium aluminum hydrate $\mathrm{C_4AH_{19}}$ is usually formed in most silicate cements.[9] In presence of various ions like $\mathrm{OH^-}$, $\mathrm{Cl^-}$, $\mathrm{CO_3^{2-}}$, metal ions or organic molecules CAH phases form so-called layered double hydroxides (LDH, like $[\mathrm{M^{2+}_{1-x}M^{3+x}(OH)_2}]^{x+}\ [(\mathrm{X^{n-}})_{x/n}\cdot y\mathrm{H_2O}]^{x-}$) which are positively charged metal oxides/hydroxides layers compensated by anions in the interlayer.[10,11,12] Due to their layered structure both cement phases, CSH and CAH (LDH), show similarities with clay minerals.

In case of water ingress (the hypothetical "worst case scenario") into a repository, the concrete will slowly dissolve over a long time period. The technical containers may also corrode. Therefore, a release of actinides (An) and fission product (Ln) in the geo- and biosphere has to be considered. During the concrete degradation a highly alkaline and highly saline chemical milieu will prevail in the repository due to the leaching of sodium hydroxide and potassium hydroxide solution (and later leaching of portlandite and CSH phases) from the cement.

Due to the prevailing reducing conditions in the repository, the lower oxidation states +III and +IV are expected to be predominant for the relevant actinides U, Np, Am, Cm, and Pu (which will determine the middle and long-term radiotoxicity of a waste repository due to their long half-lives, e.g. Np-237 $2.1\ 10^6$ a, Pu-239 $2.4\cdot10^4$ a, Am-241 $4.3\cdot10^2$ a). It is generally accepted that sorption and precipitation reactions of the actinides will dominate under these chemical conditions (Figure 1.1).[13,14]

CSH phases show a high absorption capacity for positively charged ions and are therefore important for the immobilization process of cationic radionuclides (RN).[15,16] Not only sorption but also

incorporation processes are responsible for the immobilization (Figure 1.1). On the other hand, dissolved complexes and colloidal species can enhance the migration of the RN. Therefore, complexation reactions with inorganic and organic ligands are essential mobilization processes for RN. Various organic ligands, like humic substances, clay organics, cellulose as well as cement additives and their degradation products can be present in a repository. Thus, the organic ligands contain the whole spectrum of low to macromolecular compounds.

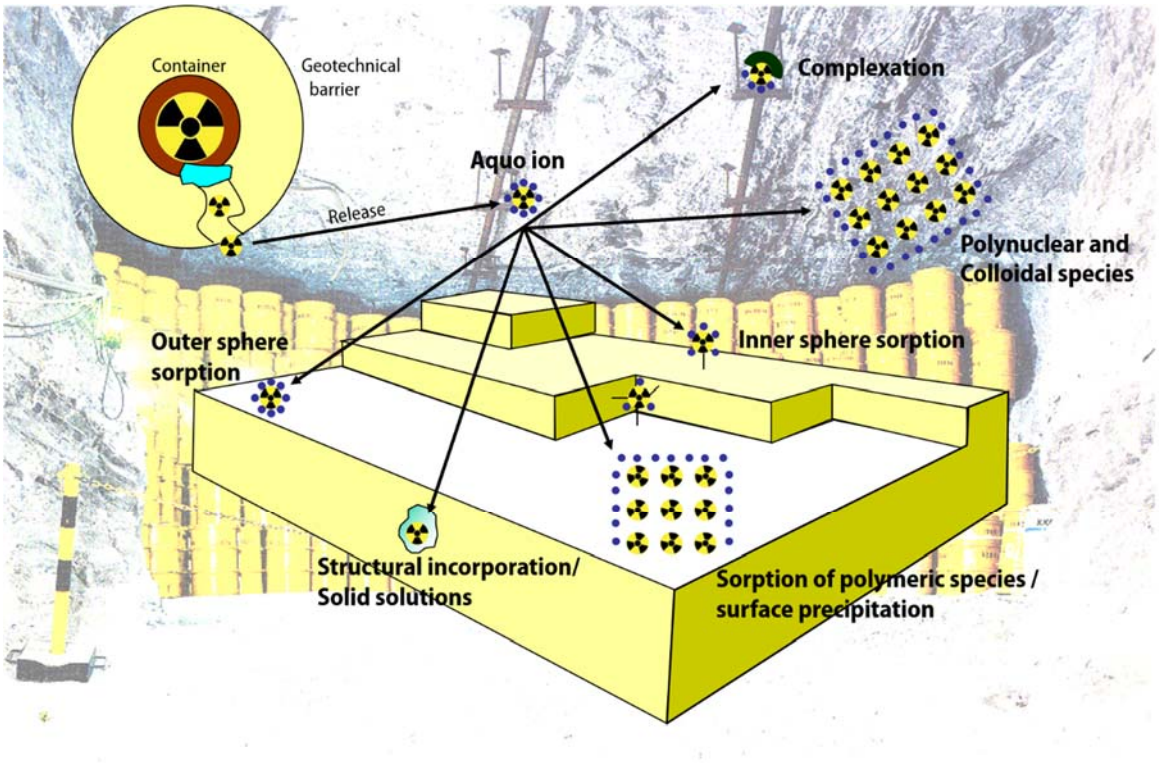

Figure 1.1: Illustration of important interactions of metals with the geosphere, adapted from Manceau et al.[17]

In difference to humic substances and clay organic matter, the role of cement additives for a possible RN mobilization has not been sufficiently investigated so far. Organic cement admixtures are added to cement to optimize its properties. They are mixtures ranging from various low-molecular hydroxycarboxylates (citrate, gluconate, malate, tartrate) up to modified polymers (polycarboxylate ether).[18,19] They are released by cement degradation and can increase the RN solubility by the formation of soluble RN-ligand complexes. Thus, they may influence RN retention in the near-field of a nuclear repository. So far, the influence of cement admixtures on RN retention in cement phases has been scarcely considered in the literature.[20,21,22]

The aim of this work is to study the interactions of trivalent Ln/An with selected α-hydroxycarboxylate containing ligands in the presence and absence of CSH phases, supplemented by CAH phases to describe them on a thermodynamic and molecular level.

The main focus is on detailed investigations with the α-hydroxydicarboxylic acid malic acid (Mal: H_2Mal, COOH-CH_2-CH(OH)-COOH) as a typical representative of the hydroxycarboxylate-containing cement admixtures. Lactic acid (HLac, COOH-CH(OH)-CH_3) and oxalic acid (H_2Oxa, COOH-COOH),

which are considered here in addition to Mal to a lesser extent, are also typical representatives of (hydroxy-)carboxylates (both are widely used in nature and in technical processes, chapter 2.2).

Due to their similar ion radii, Nd(III) and Am(III)[23], and due to their excellent luminescence properties, Eu(III) and Cm(III) were selected as representatives of the 4f and 5f elements, respectively.

The report is divided into two parts. The first part deals with the complexation reactions of Ln(III)/An(III) with Mal, Lac, Oxa and polycarboxylate-ethers using titration calorimetry and spectroscopic methods. In addition to the stability constants, the enthalpies of the complexation reactions, which are rarely given in the literature, are determined and extrapolated to the standard state (I_m = 0, T = 298,15 K, p = 1 bar) using the *specific ion interaction* Theory (SIT). The knowledge of the structure of the complexes is important in order to obtain a detailed understanding of the binding mechanisms and to interpret thermodynamic data.

The second part of the report deals with the ternary Ln(III)/An(III)-Mal-CSH system based on the analysis of the binary systems. The competitive reaction between complexation and incorporation processes of Ln(III)/An(III) at CSH (and CAH) phases under the influence of Mal is investigated by structure-sensitive methods and characterized by thermodynamic constants and K_d-values. The project is summarized schematically in Figure 1.2.

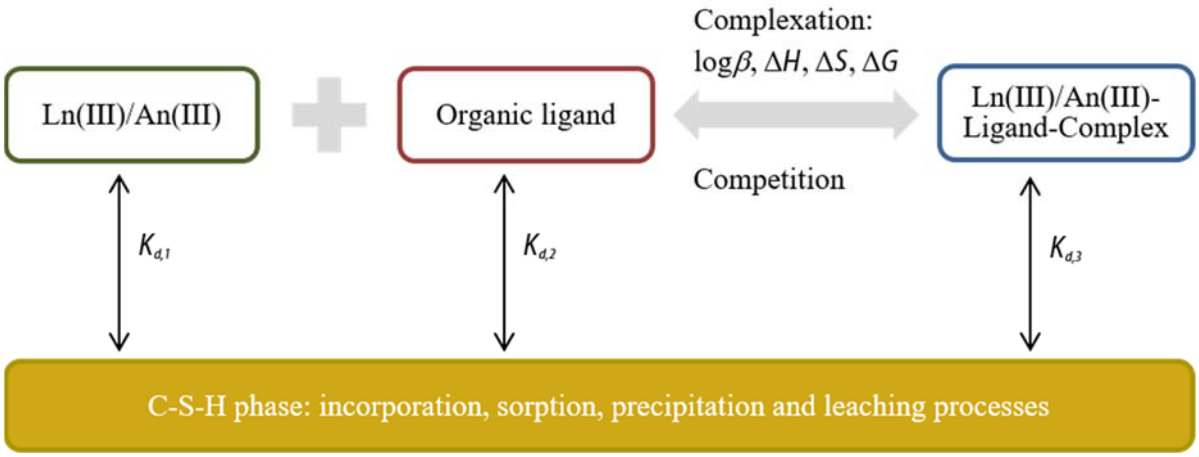

Figure 1.2: Scheme for the scope of this project, adapted from Keith-Roach[24] and Taube[25]

This work contributes to the fundamental understanding of the processes in An(III)-organic ligand-cement phase systems. This understanding is important for the modelling and description of possible mobilisation and immobilization processes of RN in a nuclear repository and, thus, for reliable risk assessment.

2 State of knowledge

2.1 Cement phases for radionuclide retention

2.1.1 Cement composition and structural model

Ordinary Portland cement consists of various clinker materials that react by hydration to form hardened cement paste. Concrete is produced by mixing cement with water, sand and gravel.

Hardened cement paste (HCP) is a heterogeneous mixture, which mineralogical consists of calcium (aluminium) silicate hydrates (C(A)SH), portlandite (calcium hydroxide), calcium aluminates such as AFm (aluminate ferrite monosulphate) and AFt (aluminate ferrite trisulphate, ettringite) and a small percentage of other phases such as hydrotalcite ($MgAlCO_3$) or iron ore. HCP consists of the CSH phases (mCaO·SiO$_2$·nH$_2$O) up to 70 weight%. These phases determine the strength and hardness of the hardened cement paste and are thus the most important cement phases. They are often described as CSH gel due to their amorphous character. The exact chemical composition is given by the molar ratio m(CaO)/m(SiO_2), the so-called C/S ratio. CSH phases in commercially available fresh Portland cement have a C/S ratio of 1.7. In aged cement, the C/S ratio is between 1.2 and 0.9.[16,26] If a cement additive such as fly ash or fine-powdered silica is used, the C/S ratio can also decrease below 1.[7]

Through the ingress of ground water or leachate, hardened cement paste (concrete) is slowly degraded by leaching out the cement phases over long time periods. Degradation begins within a few weeks and stretches over more than 100,000 years.[27,28] These degradation processes and the associated lifetime of concrete/cement are strongly dependent on its properties and on the chemical environment, i.e. on the components of the leaching water and its flow rate. For example, the addition of chlorides and sulphates, carbonation, decalcification, irradiation or heating can lead to enhanced degradation.[29,30]

Cement degradation includes several degradation stages. Figure 2.1 shows a schematic illustration of the different stages of cement degradation, which is associated with the decrease of the pH value as a function of time or the number of pore water exchange cycles.

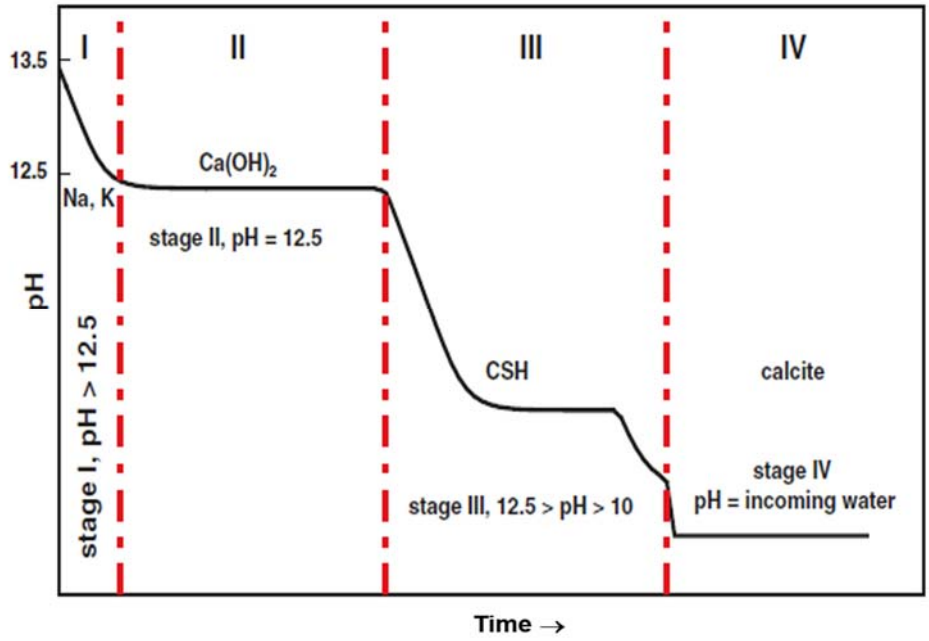

Figure 2.1: Figure 2.1: Changes of pH in cement pore water during cement degradation with time (cycles of pore water exchange); adapted from[28,31]

In the first stage of the degradation of fresh cement paste, mainly Na^+ and K^+ ions dissolve from the cement matrix. The formation of sodium hydroxide and potassium hydroxide solution results in highly alkaline cement pore water ($pH \sim 13$). The second stage is characterized by a stable pH of 12.5, which is controlled by the solubility of portlandite. In the third stage, the pH decreases further to ~ 10, accompanied by the release of the remaining cement phases such as CSH, ettringite and calcium aluminates, with the CSH phase being the most important phase. If the CSH phases age, the C/S ratio decreases from ~ 1.7 to ~ 0.7 (decalcification). In stage IV of the cement degradation, all cement phases are completely dissolved and the pH drops below 10. The composition of the pore water is determined by the remaining aggregates and the leaching water. Calcite, silica gel (silicic acid) and other mixtures of minerals can be formed.[15,28,29,30,31, 32,33]

An accurate description of the CSH structure on both microscopic and macroscopic scales is a major challenge due to its (partially) amorphous character. Many publications deal with this question, using a variety of methods (XRD with Rietveld analysis, NMR, Raman, IR spectroscopy, TEM, SANS).[34,35,36,37,38,39,40] At a C/S ratio of 0.7 CSH phases have a tobermorite-like structure. The mineral tobermorite is a crystalline calcium silicate hydrate, with a structure consisting of linear silicate chains in the form of *Dreierketten*, also called wollastonite-like chains.[41] Bernal et al. [8] postulated the so-called *Dreierketten* model for CSH phases for the first time in a pioneering work (Figure 2.2). Here CaO layers are present in which the Ca ions are 7-fold coordinated by oxygen atoms. These CaO layers are surrounded by silicate chains, which are present in the form of *Dreierketten*. These chains consist of Si-dimers (paired Si-tetrahedra, Q^2_p), which are connected by one bridging Si-tetrahedra (Q^2_b). Si-tetrahedra, each of which has two further siloxane bonds, are called Q^2- tetrahedra (Figure 2.2). At low C/S ratios (< 0.7) both types of Si-tetrahedra (Q^2_p und Q^2_b) are present. The Q^2_p-tetrahedra share one O,O

edge each with an adjacent CaO- polyhedra and the remaining oxygen atoms with further Si-tetrahedra. The $Q^2{}_b$-tetrahedra share only one oxygen atom with the pyramidal tip of a CaO- polyhedra. There is one free oxygen atom in the $Q^2{}_b$-tetrahedra, which is neutralized by a proton; so-called silanols (≡Si-$(OH)_n$). The silicate end groups, called Q^1-tetrahedra, also have free silane (di)ol groups. Water molecules and Ca-ions are present in the intermediate layer. [6,42,43,44,45]

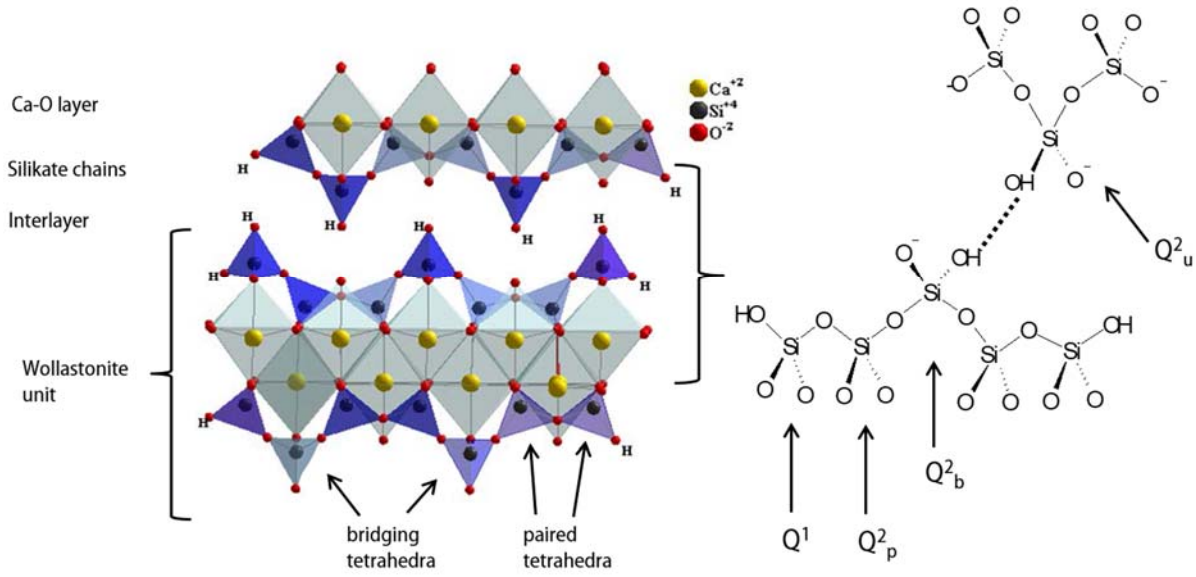

Figure 2.2: Schematic 14 Å-tobermorite-based CSH structure with C/S = 0.7 and with denotation of the Si-tetrahedra; explanation see text; adapted from Richardson[7] and Taube[25]

Some literature describes CSH phases as jennite-like structures.[26,46] Jennite, similar to wollastonite, is a crystalline calcium silicate which has a higher C/S ratio than tobermorite (C/S (J) 1.5) Figure 2.3 shows schematically the development of the CSH phases with increasing C/S ratio. At a C/S ratio > 0.7, i.e. with increasing *pH*, the $Q^2{}_b$-tetrahedra are gradually eliminated and the silan(di)ol groups dissociate in the intermediate layer or at the end groups. This results in potential binding sites for Ca^{2+}- and other cations. Grangeon et al. [35] and Matsuyama et al.[47] showed by XRD and ^{29}Si-NMR measurements a shortening or depolymerization of the Si-chains (mean number of Si-tetrahedra in the wollastonite-like structure) with increasing C/S ratio. Due to the reduced bonding of the eliminated Si-tetrahedra the layer-to-layer distance is increased. A further increasing C/S ratio reduces the layer-to-layer distance again, because the incorporated Ca^{2+} ions hold the layers together. The final distance of the interlayer is determined by incorporated portlandite ($Ca(OH)_2$).

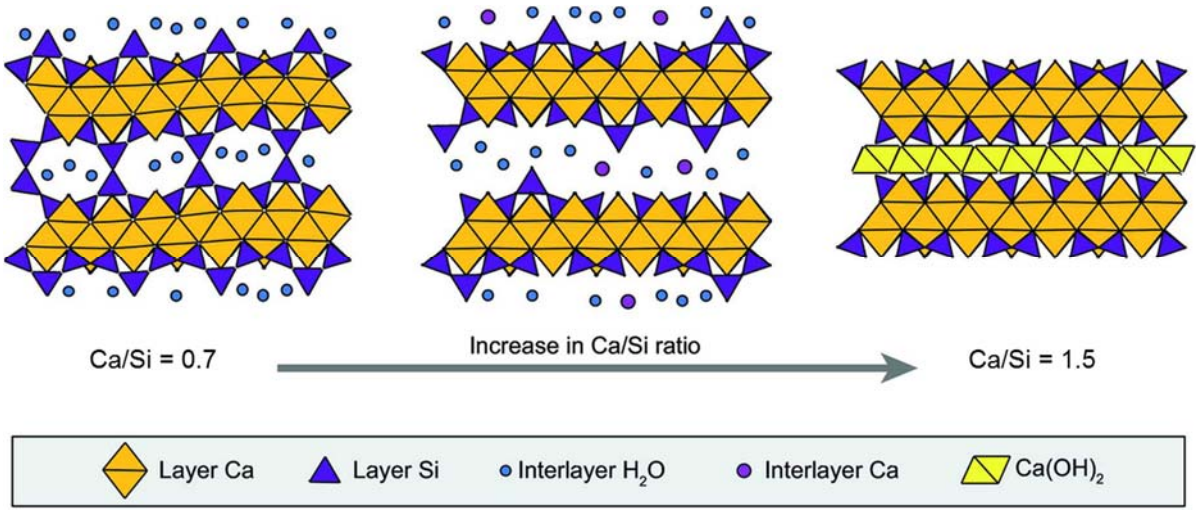

Figure 2.3: Scheme of evolution of the CSH structure as a function of the C/S ratio from Grangeon et al.[35]

Cement also contains several calciumaluminate, like tricalciumaluminate (C_3A), as essential additional constituents. This leads to the formation of multiple calcium aluminate hydrate (CAH) phases. The stable tetracalcium aluminium hydrate C_4AH_{19}, the CaO-richest compound, is formed in most silicate cements.[9] The most dominant and well-known CAH phase at ambient conditions is katoite, C_3AH_6. In contrast to the CSH phases, CAH phases (e.g. katoite) form crystalline structures with defined diffraction patterns, provided that no anions are present. The presence of anions like OH^-, Cl^-, NO_3^-, CO_3^{2-}, SO_4^{2-} induces the formation of layered double hydroxides (LDH).[48] LDH phases have a typical layered structure with a repeating pattern that can be represented by the general formula $[M^{2+}_{1-x}\,M^{3+}_{x}(OH)_2]^{x+}\,(A^{n-})_{x/n}\cdot H_2O$. There is a multitude of layer metal ions (M^{2+}, M^{3+}) and interlayer anions (A^{n-}) possible. In the case of CAH-LDH the metal ions are Ca^{2+} and Al^{3+} in different ratios. The layer metal ions (Al, Ca) are octahedral coordinated by OH^-, leaving a positive charge that is compensated by the interlayer anion.[49]

2.1.2 Cement admixtures

Additives are added to the cement to improve the handling of the cement-based materials and to influence physical properties such as compressive strength, resistance or hardening time. There are many different types of additives: superplasticizer, retarder, accelerator, air-entraining agent, anti-corrosion agent etc. They consist of a multitude of different substance classes, from simple carbohydrates to complex mixtures of macromolecules. The exact composition of the admixtures is many cases not known for reasons of business confidentiality.[5,19,50]

Superplasticizers prolong the phase in which the cement paste is liquid and can be brought into form. They usually also reduce the amount of water required for mixing the concrete (water-reducing additives). This results in a reduction in porosity. Sulfonated naphthalene or melamine-formaldehyde poly-condensates and lignin sulfonates are traditional superplasticizers (Figure 2.4). The most commonly used retarders, which operate similar to superplasticizers are hydroxycarboxylates (gluconic acid, calcium citrate), sugars such as sucrose and glucose, and phosphates (Figure 2.4). Their retarding

effect is attributed to the precipitation of poorly soluble Ca-complexes on the CSH grain surfaces.[21, 51,52,53,54]

Polycarboxylate and polycarboxylate-ether based macromolecules (PCE, e.g. Glenium51, BASF AG, Switzerland) are the most important SP groups (Figure 2.4) since the 1990s due to their high efficiency. They are highly variable due to the large number of possible monomers, monomer combination options and the flexible degree of polymerization of the corresponding main and side chains. The negatively charged carboxylate groups of the so-called comb polymers adsorb on the positively charged cement grain surface. By steric hindrance of the long side chains in combination with electrostatic repulsion a dispersion of the cement particles takes place. Thus, SP retards the binding of the hydration products and the crystallization. This improves the fluidity of the cement paste. After the delayed hydration, the SP are absorbed into the cement phase by adsorption or incorporation.[19,20,36,55,56,57,58]

Although cement additives are only present in small quantities in the final concrete (1-2% related to the dry mass of the concrete), their total mass in the repository will not be negligible.[59] Due to the high number of carboxylic functional groups especially PCEs are highly predestined for the complexation of RN.

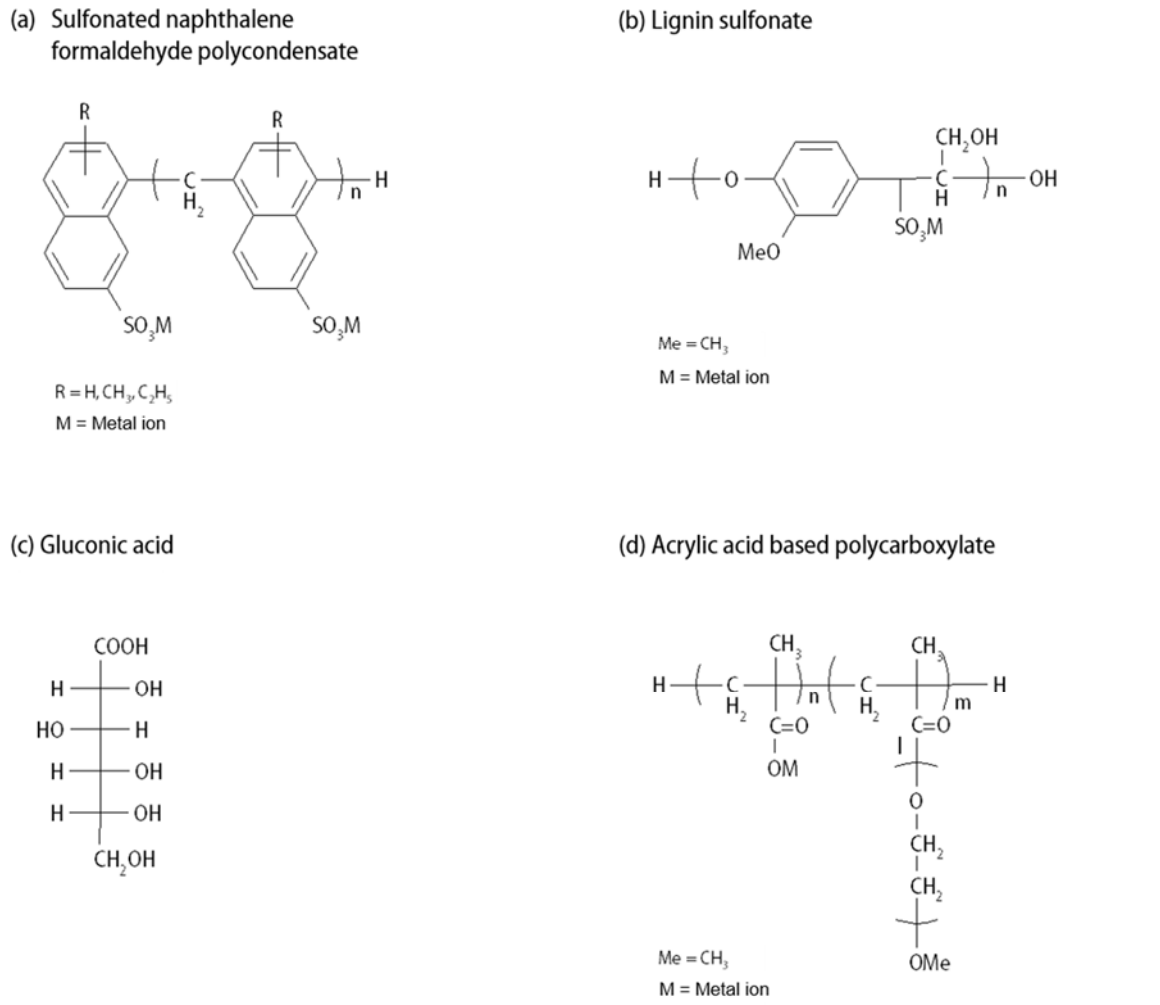

Figure 2.4: Structural formulas of selected cement additives

2.1.3 Interaction of radionuclides with cement

The use of cement-based materials (concrete, mortar) as backfill or construction material in a potential repository requires a detailed understanding of the RN uptake in cement and clarification of the influence of additives. According to the HSAB principle, An(III) and Ln(III) are hard Lewis acids and thus bind strongly to hard Lewis bases such as OH groups. Since CSH phases contain many oxygen atoms as electron donors, a strong Ln(III)/An(III) sorption on CSH phases is to be expected. Thus, the CSH phases play a crucial role in the immobilization process of RN due to the high number of reactive binding sites on the surface (reactive surface of 148 $m^2 \cdot g^{-1}$).[60]

In a large number of publications, the sorption of Ln/An in HCP and CSH phases has already been investigated and corresponding K_d-values were determined (selection for Ln(III)/An(III) in Table 2.1).[15,16,61,62,63] Some studies show also that Ln/An are present structurally in the same chemical environment in HCP and CSH phases, consequently making the CSH phases the main binding partner in HCP.[64,65,66]

The Ln(III)/An(III) sorption at CSH phases is generally very high and is not influenced by the C/S ratio. For Am(III) and Eu(III) an equally strong sorption behavior was observed from Tits and Wieland.[16] In contrast, Ochs et al.[15] found a higher affinity of Eu(III) to CSH phases compared to Am(III). These differences are attributed to the higher Eu(III) hydrolysis constant for the 1:3 complex (main species under highly alkaline conditions), i.e. to the stronger hydrolysis of Eu(III) (see Ref.[16,67]). Nevertheless, all specific K_d-values are in similar regions (10^5 $L \cdot kg^{-1} < K_d < 10^6$ $L \cdot kg^{-1}$,Table 2.1) and the small discrepancies may be caused by different experimental parameters.

Tits et al.[68] and Häußler et al.[62] explain the high affinity of Ln(III)/An(III) to CSH phases by means of the using the concept of inter-ligand electrostatic repulsion between hydroxyl groups in the Am(III) coordination sphere. This concept was originally used by Neck and colleagues[69] to predict stability constants for An-complexes with inorganic ligands. It suggests that for each oxidation state only a limited number of ligands can bind in the first coordination sphere of the corresponding An. For trivalent and hexavalent An, a maximum number of four OH groups or ligands is allowed. Thus, the hydrolysis species $An(III)(OH)_3$, which is present from $pH > 10$, can bind to a surface, and $An(VI)O_2(OH_4)^{2-}$, for example, cannot form any further surface complexes.

While older publications assume a surface complex of Ln/An at the silanol groups in the intermediate layers or at the end groups of the CSH phases, in recent years there has been increasing evidence of an incorporation of Ln/An into the CSH phases. A two-step process has been identified: a fast surface complexation/absorption (inner sphere) or surface precipitation followed by a slow incorporation into the CSH phases. For trivalent An, an incorporation into the CaO and an adsorption in the CSH intermediate layer was found. A substitution of Ca^{2+} by the trivalent Ln/An is assumed.[64,65,66,76,77,70,71,72,73,74,75]

Table 2.1: Distribution coefficients of trivalent Ln/An at CSH phases and HCP from the literature

Metal ion	C/S-ratio	*pH* and medium	S/L $kg \cdot L^{-1}$	$[Metal]_{ini}$ $mol \cdot L^{-1}$	K_d $L \cdot kg^{-1}$	log K_d	Reference
Eu(III)	0.66 – 1.25	H_2O	$2 \cdot 10^{-3}$	$1 \cdot 10^{-4}$	$\geq 2.7 \cdot 10^{4}$	≥ 4.43	[76]
	0.66 – 1.25	H_2O	$2 \cdot 10^{-3}$	$2.6 \cdot 10^{-10}$	$\geq 1.8 \cdot 10^{5}$	≥ 5.26	[76]
	1.0/ 1.1	13.3; ACW	$3.8 \cdot 10^{-4}$. $5.4 \cdot 10^{-3}$	$2 \cdot 10^{-9}$	$(6 \pm 3) \cdot 10^{5}$	5.78 ± 0.24	[77]
	1.0	13.3; ACW	$5 \cdot 10^{-4}$	$10^{-10} - 5 \cdot 10^{-8}$	$(4 \pm 2) \cdot 10^{5}$	5.60 ± 0.24	[16]
	HTS cement	13.3; ACW	10^{-5} - 10^{-3}	10^{-10}	$(5 \pm 2) \cdot 10^{5}$	5.70 ± 0.19	[78]
Am(III)	1.25 – 1.70	H_2O	$1 \cdot 10^{-3}$	$1 \cdot 10^{-11}$	$(6 \pm 2) \cdot 10^{4}$	4.78 ± 0.15	[79]
	0.76 – 1.46	H_2O	0.5 - $2 \cdot 10^{-2}$	$1 \cdot 10^{-8}$	$4 \cdot 10^{5}$	5.60	[62]
	0.7 – 1.3	9.8 - 12.2; H_2O	$5 \cdot 10^{-4}$	$1 \cdot 10^{-6}$	$(86 - 200) \cdot 10^{3}$	4.93 - 5.30	[15]
	CEM I	9.8 - 12.2; H_2O	$5 \cdot 10^{-4}$	$1 \cdot 10^{-6}$	$(40 - 150) \cdot 10^{3}$	4.60 - 5.18	[15]

HTS – Haute Teneur en Silice, sulphate-resistant Portland cement; CEM I – commercially available Portland cement; ACW – artificial cement pore water

During cement degradation additives decompose in the highly alkaline medium to small organic compounds (acetate, oxalate, phthalate, phenol, various hydroxycarboxylates).[21,58,80] Conversely, these organic substances can also accelerate cement degradation, since they cause decalcification of cement by Ca complexation.[81,82] The Ln/An uptake in cement or CSH phases could consequently be increased by the formation of ternary or quaternary surface complexes (Ln/An-ligand-CSH or Ln/An-OH-ligand-CSH).[21,83,84] Furthermore, soluble mixed species (like Ca-Ln/An-OH-ligand)[85] could be also formed which do not sorb on the CSH surface or which compete with Ln/An for sorption sites on the cement surface.

For instance, α-hydroxycarboxylates can form strong complexes in the alkaline *pH* range, thus, having the ability to influence Ln/An speciation even in the presence of cement pore water conditions.[21,83,86,87,88] One important substance in this respect is isosaccharinic acid (ISA), which is a strong complexing agent for Ln/An. It is the main degradation product of cellulose under alkaline conditions.[24,89] Numerous studies have shown that ISA can increase the solubility of Ln/An under alkaline conditions by forming stable Ln/An-ISA complexes depending on the ISA concentration.[80,85,89,90,91,92]

Sorption experiments (e.g. with Eu(III)) do not show a significant influence of polycarboxylate-ether based SPs, sulfonated naphthalene-formaldehyde condensates, lignin sulfonates and their degradation products on the RN sorption on HCP and on the structural properties of the CSH phases (Q^1 and Q^2 fractions). Furthermore, very low distribution coefficients (K_d = 0,85 - 17 $L \cdot kg^{-1}$ cf. Table 2.1) of the SPs or the low-molecular organic compounds on cement phases were found, which indicates a

lower affinity of SP compared to Ln(III)/An(III).[20,21,93] Kitamura et. al. showed that polycarboxylate-ether based superplasticizers did not have a significant effect on the solubility of Th(IV) and Am(III)[94]. Previous work on the influence of cement additives on Ln/An mobilization show that the interactions vary according to the respective composition and the chemical properties of the cement additives. Possible binding mechanisms have hardly been investigated so far.[20,21,22] Therefore, additive-specific investigations are necessary to obtain an understanding of the interactions of Ln/An with the cement additives (in cement phases). Due to the complexity of cement additives, simplified structural models or individual components of the additive mixture must be investigated in order to determine stability constants and stoichiometry of the RN (ligand) complexes.

2.2 Model ligands

The model ligands used in this work are malic acid (H_2Mal, COOH-CH_2-CH(OH)-COOH), lactic acid (HLac, COOH-CH(OH)-CH_3), oxalic acid (H_2Oxa, COOH-COOH) and tartaric acid (H_2Tar, COOH-CH(OH)-CH(OH)-COOH). The focus lies to the investigations with the dicarboxylate malate (Mal, anionic form of malic acid), since almost no thermodynamic and structural data on the Ln(III)/An(III) complexation are available. Lac was considered as a small structural unit of Mal (and Tar with one hydroxy group more than Mal), and Oxa as a further chelating ligand.

They are part of the clay organics and part of the cement additives (those in particularly malic and tartaric acid) or their degradation products.[19,84,95,96,97,98,99,100] These four ligands may also be released into a repository by natural pore or surface waters as degradation products of high-molecular organic substances (like humic substances). Figure 2.5 shows the molecular structures and possible entering paths of the ligands used.

For the extrapolation of stability constants to higher temperatures, as expected in a repository, enthalpy values of the complexation reactions are required.[101] The *Specific Ion Interaction Theory (SIT)* is used for the extrapolation of conditional thermodynamic data into the standard state. The *NEA-TDB* reveals that enthalpy values are not available for a large number of complexing reactions.[102] Therefore, in this project these enthalpy values the investigated ligands were determined and extrapolated to standard conditions. Ionic-strength dependent investigations have been carried out very rarely. However, due to the varying salinities in the host rocks, such investigations are indispensable to provide reliable thermodynamic data for modelling at given salinities.

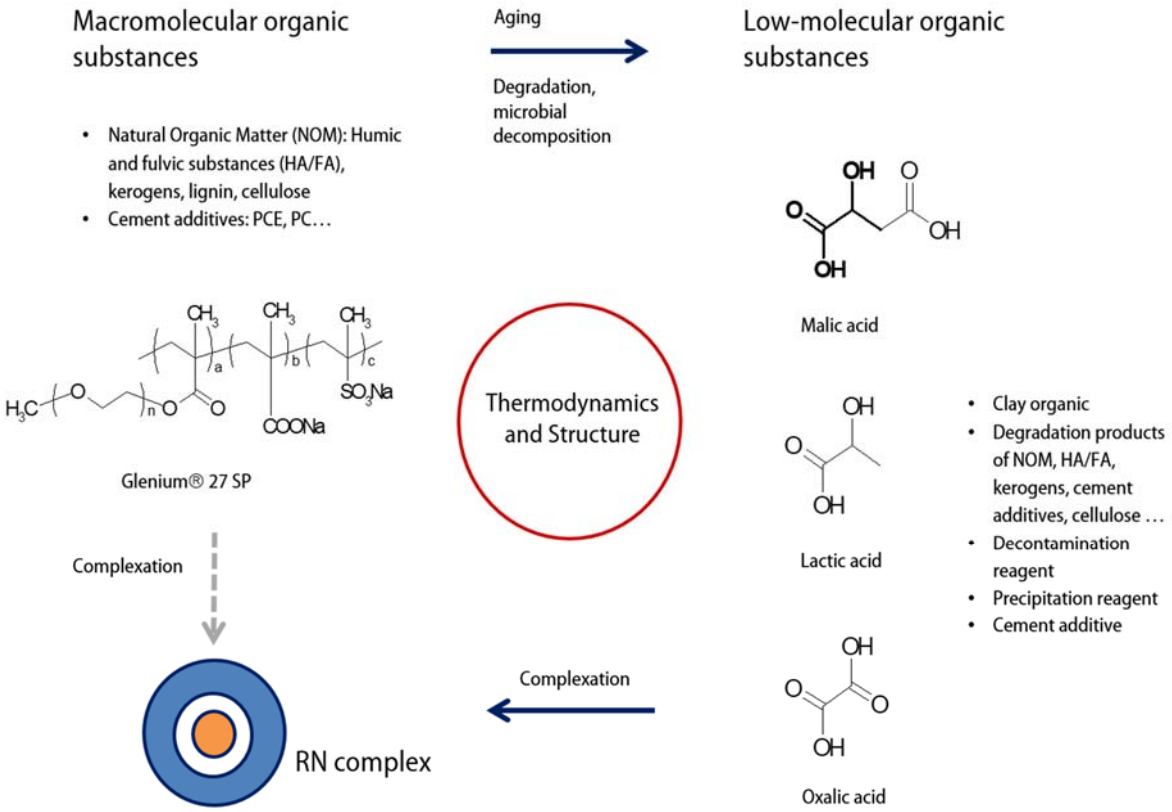

Figure 2.5: Schematic illustration of possible paths of organic substances in a repository. In this work, the degradation products, low-molecular compounds, are used as model substances to determine thermodynamic and structural complexation data, taken with permission from[25]

Malate as well as tartrate have been used since the 1950s (in addition to gluconate and citrate) as a water-reducing cement additive.[19,54] Neither thermodynamic nor structural data are known for An(III)-Mal complexes. For some Ln(III), stability constants of Mal complexes have been published, but they show large discrepancies within one element (Table 7.2). No thermodynamic data are available in the standard state at infinite dilution. In only a few articles the molecular structure of mononuclear Ln(III)-Mal complexes in the acidic *pH* range has been investigated and the formation of a chelate ring has been proposed.[103,104,105,106,107,108] The exact structure of this chelate ring (5, 6 or 7-membered) was not considered.

Lactate is used in the *Talspeak* actinide lanthanide separation process, which may be part of the reprocessing of spent fuel.[109] An(III)/An(III)-Lac complexes have been already investigated in many studies and corresponding stability constants, reaction enthalpies and entropies have been published (Table 7.2).[110,111,112,113,114,115,116,117] However, only conditional thermodynamic data have been determined, mostly with $NaClO_4$ as the background electrolyte at only one ionic strength. Although NaCl is the main constituent of pore waters of clay formations and salt rock with concentrations of 4 to 12 mol·L^{-1}, only few data in this medium are available in the literature.[118] Structural investigations of the Ln(III)/An(III)-Lac coordination show the binding of the metal ions in a 5-membered chelate ring via the carboxylate and the (protonated) hydroxy group.[110,119]

Oxalate is used as Ln and An decontamination, precipitation and separation reagent in several technical processes and therefore can be present in a future repository.[102,120] Therefore, Oxa is present in

large quantities in some repositories (for instance in the *Waste Isolation Pilot Plant*, New Mexico, Nevada ~ 50tons[121]). The *side-on* coordination over both carboxylate groups of Oxa in Ln/An complexes resulting in a 5-membered chelate ring has already been confirmed by TRLFS spectroscopy and molecular dynamic calculations.[122,123] But similar to Lac, no or only few thermodynamic standard data - especially enthalpy values in the standard state - are available.

Until recently, very little was known about the interactions of An with SPs. In some very recent studies, carried out in this GRaZ joint project, thermodynamic and structural data of complexes of lanthanides (which are used as surrogates for An(III)) with polycarboxylat-ether based SPs were determined for the first time. The authors found a slightly endothermic and entropy driven 1 to 1 complexation with a non-chelate coordination of the lanthanide ions through three carboxylic groups (at $I = 0.1$).[124,125,126] Systematic ionic strength dependent thermodynamic data, however, are still missing.

3 Methods and materials

3.1 Chemicals and preparation of aqueous solutions

The samples for UV-Vis, laser fluorescence and ITC measurements were prepared on a molal scale ($mol \cdot kg^{-1}$, "*m*") to avoid concentration changes due to density changes at different ionic strengths. If necessary, the conversion to the molar concentration scale was performed using the conversion factors given in NEA-TDB.[102]

Stock solutions of Nd(III), Eu(III) and the ligands. Ultrapure water (0.1 $\mu S \cdot cm^{-1}$, TKA Micro Pure, JWT, Jena, Germany) was used for the preparation for all samples. All chemicals were used without further purification. The Nd(III), Eu(III), malate, lactate, oxalate and PCE stock solutions were prepared by weighing the respective compound (Table 7.1) and dissolving in ultrapure water. The concentration of the ligand stock solution was checked by determining the total organic carbon content (multiN/C 2100, Analytik Jena, Germany). The concentrations of Nd(III) and Eu(III) were determined by using inductively coupled plasma-mass spectrometry (ICP-MS, NexION 350X, Perkin Elmer, Waltham, USA).

Am(III)-stock solution. ^{243}Am was received from Oak Ridge National Laboratory as AmO_2. The oxide was dissolved in 10 M HCl. The obtained stock solution contains $6.6 \cdot 10^{-2}$ $mol \cdot L^{-1}$ ^{243}Am und $1.97 \cdot 10^{-3}$ $mol \cdot L^{-1}$ ^{241}Am. The purity of the isotopes was checked by α - and γ-spectrometry, whereby only the daughter nuclide ^{239}Np was determined in equilibrium (~ 0.0001 %). Aliquots of this solution were used for ITC, UV-Vis and EXAFS experiments. Due to radiation protection requirements the handling of ^{243}Am was carried out only in a glove box. Therefore, weighing of the substances was not possible and all Am(III) solutions were prepared on the molar scale.

Cm(III)-stock solution. For investigations with Cm a $2.95 \cdot 10^{-4}$ $mol \cdot L^{-1}$ stock solution of the long-lived Cm-isotope ^{248}Cm in 0.04 $mol \cdot L^{-1}$ $HClO_4$ was used. The solution is composed as follows: 97.3 % ^{248}Cm, 2.6 % ^{246}Cm, 0.04 % ^{245}Cm, 0.02 % ^{247}Cm and 0.009 % ^{244}Cm.

pH measurements. The *pH* values of the solutions were measured at low ionic strength ($I_m < 0.1$) using an InoLab pH 730 pH meter (WTW, Weilheim, Germany) and a pH glass electrode (SI Analytics, BlueLine 16 pH, Weilheim, Germany). Two-point calibrations of the pH-electrode were performed with buffer solutions (Certipur, Darmstadt, Germany). By adding HCl and NaOH solutions at different concentrations (standard solution between 0.01 to 5 M, Carl Roth, Karlsruhe, Germany) the required *pH* value was adjusted. Solid sodium chloride was finally added as background electrolyte. The ionic strength was typically 0.5 m NaCl except for the ionic strength dependent measurements. At high ionic strengths the measured pH_{exp} does not correspond to the thermodynamic pH_c due to the ionic strength dependence of the H^+ activity coefficient γ (Equation 3.1).

$$pH_c = -\log [H^+] = -\log \frac{a_{H^+}}{\gamma_{H^+}} \qquad 3.1$$

The thermodynamic pH_c is calculated from the experimental *pH* value (pH_{exp}) and a correction function A (Equation 3.2). The correction function A is determined experimentally by calibrating the electrode using calibration solutions with defined NaCl and H^+ concentrations (Equation 3.3). Thus,

the pH_{exp} value of each salt solution can be corrected.[127,128] For $I_m \leq 0.5$ pH_{exp} is equivalent to pH_c within the uncertainties of 0.05. It should be noted that the correction function A (Equation 3.3) is only valid for the used electrode.

$$pH_c = pH_{exp} + log\,\gamma_{H+} = pH_{exp} + A \qquad 3.2$$

$$A = -0.0050\,(m_{NaCl})^2 + 0.2285\,(m_{NaCl}) - 0.1075 \qquad 3.3$$

3.2 Batch experiments with CSH and CAH phases

All sorption experiments with CSH/CAH phases were performed in a glove box (MBraun, Labmaster, Garching, Germany) under a nitrogen atmosphere ($p_{O_2}, p_{H_2O} < 1$ ppm). Ultrapure water was boiled and then rinsed with nitrogen in the glove box.

For the preparation of the CSH phases, ultrapure water (for alkali-free CSH phases) or artificial cement pore water (ACW) was added to mixtures of AEROSIL 300 (SiO_2) (Evonik, Essen, Germany) and CaO (*Sigma-Aldrich*, *reagent grade*, Darmstadt, German, calcinated at 1000 °C) in PFA tubes or Grainer tubes. The weighed amounts of the used solids and the solvent depended on the C/S ratio (0.4 to 2.0) and the solid-to-liquid ratio (s/l ratio from $2{\cdot}10^{-3}$ to $2.4{\cdot}10^{-2}$ kg·L^{-1}), respectively. The composition of the ACW of [NaOH] = 0.114 mol·L^{-1} and [KOH] = 0.18 mol·L^{-1} is based on an estimation of the cement pore water composition in hardened cement paste before cement degradation.[16] To prepare the alkaline stock solutions, NaOH or KOH pellets were rinsed with boiled ultrapure water and a supersaturated solution was then prepared. Their concentrations were determined by ICP-MS.

For the preparation of the CAH phase (mainly katoite) a solution of 0.1 M NaOH was prepared from NaOH pellets in ultrapure water. The NaOH pellets were rinsed with ultrapure water in a glovebox to remove the carbonate layer. To this solution or pure water a precursor, $Ca_3Al_2O_6$ (C_3A, calcinated at 1000 °C and checked via thermogravimetry for residual carbonate), was added. The C/A ratio was given by the precursor.

Following these preparations, aliquots of metal (Eu, Nd), ligand or metal-ligand stock solution (see above) or weighed amounts of these substances were added to the CSH and CAH suspensions.

The CSH/CAH suspensions of inactive samples were homogenized in an overhead shaker for at least 4 weeks, then filtered via a Büchner funnel with filter paper (*Sartorius*, grade 391, Göttingen, Germany) using a peristaltic pump, the filter cake was briefly washed with ultrapure water, and the solids were lyophilized. Random samples of the supernatant were analyzed by ICP-MS for Ca, Si, Al, Eu/Nd (Na and K). The C/S ratio was determined from the initial amounts of n_i (Ca/Si) (weighed amounts of CaO and SiO_2) minus the Ca and Si concentration in the equilibrium solution of the CSH phases c_{sol} (Ca/Si) measured by ICP-MS (Equation 3.4). The solids were also analyzed by ICP-MS (HF digestion) and used to check the C/S ratio determined by weighing.

$$C{:}S = \frac{n_i(Ca) - c_{sol}(Ca) \cdot V}{n_i(Si) - c_{sol}(Si) \cdot V} \qquad 3.4$$

For the batch experiments with radiotracers, aliquots (in µL) of a ^{243}Am-($1{\cdot}10^5$ Bq/µL), ^{248}Cm-(1 Bq/µL), ^{152}Eu- ($3.5{\cdot}10^2$ Bq/µL) or ^{14}C-labelled Mal stock solution (7.6 Bq/µL) were added to the freshly prepared CSH suspension in water or ACW in addition to their inactive analogues (exception: Am, Cm). The doped CSH suspensions were shaken in an overhead shaker for at least 4 weeks and then centrifuged (*Sigma* Laboratory Centrifuges 3K30H, Osterode, Germany; Cm: 30,000 g, 90 min; Am: 6,000 g, 2x 30 min). The Cm-doped CSH phases were shaken for 14 days. Aliquots of the supernatant of the ^{248}Cm(III)- and C-14-doped samples were analyzed by LSC (*Tricarb* 3100, Perkin Elmer, USA) and aliquots of the supernatant and suspension of the ^{152}Eu and ^{243}Am doped samples by γ-counting (*Hidex* AMG, Finland).

3.3 Analysis of the batch experiments and general experimental uncertainties

The sorption of radionuclides (RN) on solid phases is quantified by using the distribution ratio K_d, which describes the distribution of RN between liquid and solid phase and is defined as follows:

$$K_d = \frac{\{M_S\}}{[M]} = \frac{[M_S]}{[M]} \cdot \frac{V}{m} = \frac{[M_T] - [M]}{[M]} \cdot \frac{V}{m} \qquad \text{L·kg}^{-1} \qquad 3.5$$

$\{M_S\}$ is the concentration of RN on the solid phase in mol·kg^{-1}, $[M]$ und $[M_S]$ are the RN concentrations in the liquid or solid phase in mol·kg^{-1}. $[M_T]$ is the total concentration of RNs in the suspension in mol·kg^{-1}. V is the volume of the liquid phase in liter and m is the mass of the solid phase in kg.

In this work, the K_d values were determined by means of batch experiments with radiotracers, i.e. they are calculated by the ratio of the activity of the RN in the solid phase and in the supernatant solution (liquid phase) (Equation 3.6).

$$K_d = \frac{A_S}{A_l} = \frac{(A_{susp} - A_l)}{A_l} \cdot \frac{V}{m} \qquad \text{L·kg}^{-1} \qquad 3.6$$

A_s is the activity of the RN in the solid phase in cpm·kg^{-1}, A_{susp} is the activity in the suspension in cpm·L^{-1} and A_l is the activity in the state of equilibrium (supernatant solution) in cpm·L^{-1}.

Normally, the statistical error is negligible for activity measurements with a sufficiently high count rate in contrast to other systematic and random errors. However, because the sorption of trivalent Ln/An on CSH phases is very high, very low activities are present in the supernatant solution, which are not significantly higher than the background activity even if the counting times are reasonably long. Therefore, the statistical error of the counting rates can increase significantly, so that the detection limit of the measuring method is reached.

Tits et al.[129] introduced the maximum sorption value, $K_{d,max}$ (Equation 3.7). The $K_{d,max}$ value is the largest distribution ratio that can be measured with sufficient accuracy. It is based on the total activity, the background activity and the s/l ratio

$$K_{d,\,max} = \frac{(A_{susp} - A_{l,\,min})}{A_{l,min}} \cdot \frac{V}{m} \qquad \text{L·kg}^{-1} \qquad 3.7$$

A_{susp} is the total initial activity in the suspension in cpm·ml^{-1}, $A_{l,min}$ the minimum measurable activity in the supernatant in cpm·mL^{-1}, m is the solid mass in kg und V is the volume of the solution in L

$A_{l,min}$ represents the minimum measurable activity that can be determined for the selected measuring time t. It is described by the minimum measurable net count rate in the supernatant $C_{l,min}$ (Equation 3.8). This count rate $C_{l,min}$ (Equation 3.9) is necessary to obtain results with a relative uncertainty < 10 %.

$$A_{l,\,min} = \frac{C_{l,\,min}}{t} \qquad \text{cpm·mL}^{-1} \qquad 3.8$$

$$C_{l,\,min} = 50 \cdot (1 + \sqrt{(1 + 0.08 \cdot B)}) \qquad \text{counts·mL}^{-1} \qquad 3.9$$

$A_{l,min}$ is the minimum measurable activity, $C_{l,min}$ is the minimum measurable net count rate and B the background count rate in counts·mL^{-1} for the measuring time t.

The $K_{d,max}$ values determined in this project are listed in Table 3.1.

The determination of K_d values is influenced by several error sources, which may be of random or systematic origin. The systematic errors can be caused by incorrectly calibrated instruments or incorrect measurement conditions. Random errors can result from a heterogeneous distribution in the solid samples (e.g. in sorption experiments), from sample preparation (e.g. weighing, dilution etc.) or from the measurement of activity or concentrations. The largest uncertainty of the K_d values results from errors of the s/l ratio (thus from the preparation of the CSH suspension) and the activity measurements of the suspension (A_{susp}) and the supernatant (A_l). Uncertainties of the activity of the blank solution and the uncertainty of the volume can be neglected. Insufficient phase separation and the resulting transfer of solid phase into the supernatant can lead to a considerable overestimation of the activities (A_l) in the supernatant solution. Furthermore, aliquots of the CSH suspension were taken by means of a pipette to prepare samples with the same s/l ratio (and different additive additions). The preparation of diluted CSH suspensions depends strongly on the homogeneity of the concentrated suspension. Inhomogeneities can result in large uncertainties of the s/l ratio. These uncertainties are difficult to quantify. For this reason, randomly chosen experiments were repeated to estimate the error of K_d. The errors are within 20 %. In the case of several independent measurements, a mean value with a standard deviation σ is given. For 2σ error specifications, 95 % of all measurement points are within the confidence interval. In this report all error data were calculated according to the recommendations of NEA-TDB.[102]

Table 3.1: $K_{d,max}$ values

experiment	s/l	measure-ment time *t*	backgound count rate B	$C_{l,min}$	$A_{l,min}$	A_{susp}	log $K_{d,max}$
	$kg \cdot L^{-1}$	min	$counts \cdot mL^{-1}$	$counts \cdot mL^{-1}$	$cpm \cdot mL^{-1}$	$cpm \cdot mL^{-1}$	
C-14	$1 \cdot 10^{-2}$	60	430	348	5.8	3605	4.8
Eu-152	$1 \cdot 10^{-2}$	1440	21197	2110	1.5	1167	4.9
Cm-248	$2.4 \cdot 10^{-2}$	60	1601	618	10.3	31980	5.1

3.4 Extended X-ray absorption fine structure spectroscopy

Extended X-ray absorption fine structure (EXAFS) spectroscopy has been widely used for the element-specific structural analysis of actinide complexes, because it allows the investigation of local environments of atoms in liquids and amorphous solids. [130,131,132,133,134,135,136,137138]

Sample preparation

For the EXAFS experiments, aliquots of the Am(III) stock solution described above were used. For the investigation of the Am(III)-Mal complexation, a number of samples with varying *pH* values were prepared (detailed sample composition in Table 3.2). From each sample 250 µL were filled into a PE sample holder, sealed with a cap and placed in a sample tube.

Table 3.2: Experimental details on the aqueous EXAFS samples I_M = 0.25-0.32 (NaCl)

Sample number	***pH* -value**	**[Am(III)] / mol·L^{-1}**	**[Mal]* / mol·L^{-1}**
1	0.9	$1.3 \cdot 10^{-3}$	$2.0 \cdot 10^{-2}$
2	2.5	$1.2 \cdot 10^{-3}$	$1.9 \cdot 10^{-2}$
3	3.0	$1.3 \cdot 10^{-3}$	$1.9 \cdot 10^{-2}$
4	3.7	$1.3 \cdot 10^{-3}$	$1.9 \cdot 10^{-2}$
5	4.1	$1.2 \cdot 10^{-3}$	$1.9 \cdot 10^{-2}$
6	5.0	$1.2 \cdot 10^{-3}$	$1.9 \cdot 10^{-2}$
7	5.5	$1.2 \cdot 10^{-3}$	$1.9 \cdot 10^{-2}$
8	6.0	$1.2 \cdot 10^{-3}$	$1.9 \cdot 10^{-2}$
9	7.1	$1.2 \cdot 10^{-3}$	$1.9 \cdot 10^{-2}$
10	8.2	$1.2 \cdot 10^{-3}$	$1.9 \cdot 10^{-2}$
11$^{\#}$	9.9	$1.3 \cdot 10^{-3}$	$2.0 \cdot 10^{-2}$
12	11.0	$1.3 \cdot 10^{-3}$	$2.0 \cdot 10^{-2}$
13	10.9	$1.4 \cdot 10^{-3}$	-
14	12.0	$1.3 \cdot 10^{-3}$	$1.9 \cdot 10^{-2}$

* – $[Mal]_{total}$ is the concentration of malic acid or sodium salt independent of the protonation state.
# – EXAFS- spectrum of a solid and the supernatant solution were measured.

For the investigation of the Am(III) and the Am(III)-Mal sorption on CSH phases, a series of samples with different C/S ratios and/or Mal concentrations in ultrapure water was prepared (Table 3.3). The CSH phases were transported under liquid nitrogen and measured as wet pastes. Analog CSH pastes were prepared with Eu(III) und measured by PXRD to confirm the presence of CSH phases.

Table 3.3: Experimental details of the sorption samples for EXAFS measurements, s/l = $2 \cdot 10^{-3}$ kg·L^{-1}

Sample number	*pH*-value	C/S	[Am(III)] / mol·L^{-1}	[Am(III)]$^{\#}$ / ppm	[Mal]* / mol·L^{-1}
a	10.0	0.4	$1.1 \cdot 10^{-4}$	1300	-
b	11.8	0.8	$1.1 \cdot 10^{-4}$	1300	-
c	12.0	1.2	$1.0 \cdot 10^{-4}$	1300	-
d	10.1	0.4	$1.1 \cdot 10^{-4}$	1300	$1.6 \cdot 10^{-3}$
e	11.9	0.8	$1.1 \cdot 10^{-4}$	1300	$1.6 \cdot 10^{-3}$
f	12.1	1.2	$1.0 \cdot 10^{-4}$	1300	$1.6 \cdot 10^{-3}$
g	11.8	0.8	$1.0 \cdot 10^{-4}$	1300	$8.2 \cdot 10^{-5}$
h	12.0	1.2	$1.1 \cdot 10^{-4}$	1300	$8.2 \cdot 10^{-5}$

$^{\#}$ – The Am(III)- concentrations were measured by α-spectrometry and are related to the wet mass of the CSH phases. * – $[Mal]_{total}$ is the concentration of malic acid or sodium salt used regardless of the protonation state.

Measurement conditions

The EXAFS measurements at the Am LIII edge (18,510 eV) were performed at *the Rossendorf Beamline* (ROBL, BM20) of the European Synchrotron Radiation Facility (ESRF) at electron energies of 6 GeV and a beam current of 200 mA. The polychromatic synchrotron radiation is focused by two Rh-coated mirrors and directed onto a water-cooled Si(111) double-crystal monochromator, which generates monochromatic light of different wavelengths by changing the angle of the crystals and thus allowing the acquisition of spectra. A gas-filled ionization chamber measures the incident photon flux I_0, followed by the sample in a cryostat (placed in a glove box). In the second ionization chamber I_1 the intensity of the beam behind the sample is measured. A third ionization chamber I_2 measures simultaneously the absorption of a reference sample. In this case the Zr K edge (17,998 eV) of a Zr metal foil is used for energy calibration. For each sample, 16 - 19 energy scans were performed and averaged to obtain a sufficiently high signal-to-noise ratio. The acquisition of the L$\alpha_{1,2}$ signal was performed in fluorescence mode using a 13-element Ge detector, since measurements in transmission mode would lead to a higher experimental error at the used Am(III) concentration

Data analysis[186,139]

The data processing of the measured EXAFS spectra was performed using the EXAFSPAK[140] program, which contains standard procedures for energy calibration, statistical weighting of the 13 fluorescence

channels, their dead time correction, averaging of several scans, the extraction of the EXAFS signal and and the adjustment. In order to extract the EXAFS signal, first a background correction and normalization was performed. For this purpose, a spline function with a fixed number of individual polynomials and degrees is used. In addition, the energy of the incident X-ray photon is converted into the absolute value of the wave vector of the photoelectron k. To calculate the kinetic energy of the photoelectrons, the ionization potential (E_0) of the Am LIII edge was set to 18,515 eV and defined as a free parameter according to $\Delta E_0 = E_0 - E_t$ (ΔE_0- energy shift, E_t - theoretical ionization potential) in the shell fit. Theoretical backscatter phases and amplitudes were calculated ab-initio with the program FEFF 8.20[141].

The radial EXAFS resolution of the Am(III) samples is 0.19 Å, which is given by the used k-interval of 1.7 - 10.0 $Å^{-1}$ ($\Delta R = \pi/2\Delta k$). For the FEFF calculations of the aqueous samples a modified XRD structure of a Nd(III)-Mal/Fumarate solid[108] and AIMD structures of the Nd-$(H_2O)_9(H_2O)_n$, Nd-$Mal(H_2O)_6(H_2O)_n$ and Nd-$Mal_2(H_2O)_3(H_2O)_n$ complexes[186] were used. In all structures Nd(III) was replaced by Am(III) and multiple scattering paths up to the third order were considered. In addition, H atoms were neglected and only scattering paths up to a radial distance of 6 Å were considered. A detailed description of the FEFF calculations, the scattering phase and amplitude functions used for the shell fits is given in Taube et al.[186] For the FEFF calculations of the solid samples the 11 Å-tobermorite structure from Merlino et al. [142] was used, where one Ca was replaced by Am(III).

Furthermore, the i*terative transformation factor analysis* (ITFA)[212] was applied for the decomposition of series of EXAFS spectra into linear independent spectra and for the determination of the corresponding fractions of the spectral components (see also[139,186])

3.5 Time-resolved laser-induced fluorescence spectroscopy

Fluorescence spectroscopy is an excellent method to study the coordination chemistry of Ln/An. Eu(III) is very often used as inactive fluorescence probe due to its excellent luminescence properties (with a detection limit of Eu ~$1 \cdot 10^{-7}$ mol·L^{-1}). Among the fluorescent An(III), especially Cm(III) is used for investigations in the ultra-trace range due to its very sensitive fluorescence (with detection limit of ~$1 \cdot 10^{-9}$ mol·L^{-1}). Am(III) fluoresces only very weakly with a very short fluorescence lifetime in the ns range.

Sample preparation

The TRLFS experiments of the Eu(III)-Mal-speciation were performed with $5 \cdot 10^{-6}$ m Eu(III) and aliquots of 0.01, 0.1 and 0.5 m Mal solutions at different *pH* values. The total Mal concentration was $3 \cdot 10^{-2}$ to $1 \cdot 10^{-1}$ m at the end of the titrations. For the *pH* series [Eu] = $5 \cdot 10^{-6}$ m and [Mal] = 0.01 m were used. The Cm(III) titration with Mal was carried out in a glove box under nitrogen atmosphere. For TRLFS measurements of the Eu(III)- and Cm(III)-CSH sorbent samples, the freeze-dried (not done for Cm(III)) CSH phases were slurried with very little ultrapure water, dropped onto the sample holder and air-dried. The sample holder was then sealed and cooled in a cryostat to < 20 K. The s/l ratio of the CSH

samples was $2.1 \cdot 10^{-2}$ or $2.4 \cdot 10^{-2}$ kg·L^{-1} respectively (for experimental details on all titrations see Table 3.4).

Table 3.4: Experimental details of the TRLFS titrations with Eu(III) and Cm(III) in aqueous solution (concentrations were converted from molal to molar) and on the sorption samples

Sample/series	I_m / medium bzw. C/S	*pH*-value	[M(III)] / mol·L^{-1}	[Mal]* / mol·L^{-1}
Eu(III)-S1	0.5 m NaCl	4.0	$3.35 \cdot 10^{-6} - 5.02 \cdot 10^{-6}$	$0 - 1.33 \cdot 10^{-1}$
Eu(III)-S2	0.5 m NaCl	5.5	$3.12 \cdot 10^{-6} - 4.99 \cdot 10^{-6}$	$0 - 3.34 \cdot 10^{-2}$
Eu(III)-S3	0.5 m NaCl	1.2 – 6.4	$4.14 \cdot 10^{-6} - 4.97 \cdot 10^{-6}$	$8.18 \cdot 10^{-3} - 9.82 \cdot 10^{-3}$
Cm(III)-S1	0.5 m NaCl	7.8	$2.98 \cdot 10^{-7} - 2.29 \cdot 10^{-7}$	$0 - 5.16 \cdot 10^{-2}$
Eu(III)-CSH$^{\#}$	C/S 0.4	10.1	$1.67 \cdot 10^{-4} \triangleq$ 1278 ppm	
Eu(III)-CSH$^{\#}$	C/S 0.4	10.1	$1.68 \cdot 10^{-4} \triangleq$ 1285 ppm	$2.0 \cdot 10^{-4}$
Eu(III)-CSH$^{\#}$	C/S 1.0	12.0	$2.0 \cdot 10^{-4} \triangleq$ 1530 ppm	-
Eu(III)-CSH$^{\#}$	C/S 1.0	12.1	$2.0 \cdot 10^{-4} \triangleq$ 1530 ppm	$4.0 \cdot 10^{-3}$
Eu(III)-CSH$^{\#}$	C/S 2.0§	12.3	$2.0 \cdot 10^{-4} \triangleq$ 1530 ppm	-
Eu(III)-CSH$^{\#}$	C/S 2.0§	12.3	$2.0 \cdot 10^{-4} \triangleq$ 1530 ppm	$4.0 \cdot 10^{-3}$
Cm(III)-CSH	C/S 1.0	13.3$^{\$}$	$2.80 \cdot 10^{-6} \triangleq$ 28 ppm	$1.5 \cdot 10^{-2}$
Cm(III)-CSH	C/S 2.0§	13.3$^{\$}$	$2.80 \cdot 10^{-6} \triangleq$ 28 ppm	$1.5 \cdot 10^{-2}$

* – $[Mal]_{total}$ is the concentration of malic acid or sodium salt independent of the protonation state; $^{\#}$ – The Eu(III)- concentrations were measured by ICP-MS and are related to the dry mass of the CSH phases; $^{\$}$ – in 0.3 M NaOH; § – Portlandite content included.

The TRLFS experiments of the solid Eu(III)-CAH phases were performed with $(10\text{-}50) \cdot 10^{-3}$ m Eu(III) and $(0\text{-}150) \cdot 10^{-3}$ m NaCl at < 20 K

Devices and measurement

For aqueous speciation studies of Eu(III) a pulsed Nd : YAG-OPO laser system (Green PANTHER EX OPO, Powerlite Precision II 9020 Laser, Continuum, USA) was used, which generates an excitation wavelength of 394 nm. The laser pulse energy was ~3 mJ. The sample was placed in a standard 10 mm

cuvette temperature controlled (T = 25°C) sample holder equipped with a stirring magnet. The luminescence from the sample was collected by a glass fiber at 90° and detected by a multi-channel analyzer which consists of an Oriel MS 257 monochromator, a spectrograph with different optical grids and an Andor iStar ICCD-camera (Lot-Oriel Group). The gate width of the camera was set to 1 ms. A grating of 300 lines per mm was used. The resulting spectral range was 470 – 750 nm with a resolution of 0.7 nm. The time interval between two recorded spectra was set dynamically in the range between 0 – 60 µs. A series of time-resolved spectra usually contained up to 30 single spectra.

For the titration of Cm(III) with Mal the same laser system was used and an excitation wavelength of 396.6 nm was set. The time-resolved measurements (35 spectra) were recorded with dynamic step widths or delay times (delay time [ps]= $2{\cdot}10^6 + 5{\cdot}10^5$ x) in the range 0 - 20 µs.

The TRLFS measurements at direct excitation (site-selective) were performed on a pulsed Nd : YAG (Surelite SL I-20, Continuum, USA) dye laser system (Radiant Dyes NarrowScanK, Wermelskirchen, Germany). The luminescence of the samples was guided to the spectrograph (Andor Shamrock 303i) with different optical gratings by means of fiber optic cables and detected by an ICCD camera (Andor iStar DH340T-18H-13). The laser pulse energy and wavelength were measured using an optical power meter (Newport 1918-R, Irvine, USA) and a wavelength meter (High Finesse WS-5, Tübingen, Germany). Excitation spectra for Eu(III) were recorded between 572 and 582 nm in 0.1 - 0.5 nm steps (intensity integrated over the $^7F_2$ peak) and for Cm(III) between 600 and 625 nm in 0.1 - 0.2 nm steps, a gate width of 10 - 20 ms and a slit width of 10 - 100 µm with a 600 lines per mm grating. Additionally, time-resolved spectra with dynamic delay times of 0 - 300 µs and 0 - 200 µs were recorded at selected wavelengths.

For the Cm(III) measurements, a dye change from sulphorhodamine B to rhodamine B and rhodamine 10 was performed at 605 nm.

For Am(III)-TRLFS measurements a Nd : YAG-MOPO laser system (Spectra Physics, Mountain View, USA) was used with an excitation wavelength of 504 nm and laser pulse energy of 10 mJ. The luminescence of the sample was recorded by spectrograph (M270) and an ICCD camera (Spectrum One, Horiba-Jobin Yvon, Japan). The measuring interval (gate width) was 1 µs. The time-resolved spectra were recorded with delay times of 10 - 20 µs.

Data analysis

To calculate the fluorescence decay lifetimes, Equation 3.10 was fitted to the spectral decays of the integrated luminescence signal.

$$I(t) = \sum_{i=1}^{n} I_{0,i} \; exp(-t/\tau_i) \qquad 3.10$$

I(t) – total luminescence intensity at the time t; $I_{0,i}$ – Luminescence intensity of species i at time $t = 0$; τ_i – Fluorescence lifetime of the species i

The lifetime τ is related to the number of water or hydroxide molecules in the first coordination sphere of the metal ion assuming that the coordinating ligand is not a quencher and does not contribute to the relaxation of the excited state (Equation 3.11-3.13)[143,144,145]

$$n_{H_2O} \pm 0.5 = 1.07 \cdot \tau^{-1}_{H_2O}(ms) - 0.62 \quad \text{für Eu(III)} \quad 3.11$$

$$n_{H_2O} \pm 0.5 = 0.65 \cdot \tau^{-1}_{H_2O}(ms) - 0.88 \quad \text{für Cm(III)} \quad 3.12$$

$$n_{H_2O} \pm 0.5 = 2.56 \cdot 10^{-4} \cdot \tau^{-1}_{H_2O}(ms) - 1.43 \quad \text{für Am(III)} \quad 3.13$$

For the Eu(III)-aquo ion a fluorescence lifetime of 110 ± 3 µs was determined in water with nine coordinating water molecules.[143,205] The fluorescence lifetime of the Cm(III)-aquo ion is 65 ± 1 µs (n_{H2O} = 8.9 ± 0.5)[144] and that of the Am(III)-aquo ion is 25 ± 1 ns (n_{H_2O} = 8.8 ± 0.5)[205]. If the water molecules are replaced by other ligands, the fluorescence lifetime increases. An inner sphere complex is present. If the fluorescence lifetime remains constant, an outer sphere complex exists, since the number of water molecules does not change.

Analysis using parallel factor analysis (PARAFAC)

Parallel factor analysis (PARAFAC, implemented as an N-way toolbox in MATLAB software[146]) was used to determine stability constants for TRLFS and UV-Vis measurements. Detailed information on the algorithm can be found in[147]. In the case of TRLFS data, the decomposed matrices contain information about the species distribution, luminescence spectra and luminescence lifetimes. PARAFAC has recently been successfully applied to several RN (in)organic systems using three-dimensional TRLFS data.[148,149,150,151,152,186] The deconvolution of two-dimensional data such as UV-Vis spectra gives the distribution of the species and corresponding single component UV-Vis spectra. The great advantage of PARAFAC - finding a unique solution - does not apply for 2D data. In order to compensate for this disadvantage of the rotational invariance of 2D PARAFAC, these data were decomposed using a global analysis approach. For this case, UV-Vis data of several series (concentration and *pH* series) were analyzed simultaneously. The resulting uniqueness is further optimized by limiting the distribution of the species to their chemical distribution, as already shown in Drobot et al.[149] Multiple PARAFAC runs with randomly selected start vectors result in variations in the obtained minima, which reflect the realistic uncertainties of the values to be determined.

3.6 Isothermal titration micro-calorimetry

Isothermal titration (micro-)calorimetry (ITC) is used for the simultaneous determination of complex stability constants and complexation enthalpies as shown for example in[153,154,178]. The Equation 3.14 is the basis for titration calorimtry. The net reaction heat $Q_{r,p}$ is a function of the enthalpy of the reaction $\Delta_r H_{p,j}$ and the number of moles $\Delta n_{p,j}$, of the jth reaction product at point p (Equation 3.14) $\Delta n_{p,j}$, again

is a function of the cell volume V, of the concentrations of the components p and of the equilibrium constants of the reactions taking place in the reaction vessel (Equation 3.15, 3.16). If the stability constant(s) of the reaction(s) is (are) known, Equation 3.17 is linear and the complexation enthalpy is obtained by fitting the experimental to calculated heat curve using the least square method.

$$Q_{r,j} = \sum_{p} \Delta_r H_{p,j} \cdot n_{p,j} \qquad 3.14$$

$$Q_{r,j} = V \cdot \sum_{p} \Delta_r H_p \cdot [L_{B,p}] \qquad 3.15$$

$$[L_{B,p}] = [M] \cdot \frac{n_p K_p [L]}{1 + K_p [L]} \qquad 3.16$$

$$U\left(K_p, \Delta_r H_p\right) = \sum_{j=1}^{m} \left(Q_{r,p} - \sum_{p} \Delta n_{p,j} \cdot \Delta_r H_p \right)^2 \qquad 3.17$$

$Q_{r,j}$ – heat of reaction at the titration step j , $n_{p,j}$ – number of moles of the p-th species for the titration step j, $\Delta_R H_p$ – molar enthalpy of reaction of p-th species, $L_{B,p}$ – concentration of the bound ligand of the species p, V reaction volume, $[M]$ – total concentration of the metal, K_p – binding constant of the species p, U – sum of least squares, should be minimized

Devices and measurements

Calorimetric titrations were performed with the isothermal titration micro-calorimeter iTC200 (GE Healthcare). The volumes of both the sample and the reference cell are 200 µL. n aliquots ($n_{\min}$ = 19, $V_{\max}$ = 40 µL) of the titrant were titrated into the sample cell in 0.5 - 2 µL steps under continuous stirring with a rate of 750 rpm. The temperature for all experiments was constant at 25 °C. The time intervals between two injection steps were 120 - 180 s. In a typical titration experiment (except the experiments with PCEs and PA) the sample cell contains the metal ion solution ([M] = 1 - 5 $\cdot 10^{-3}$ m, $pH_C \sim 5.5$) and the syringe is filled with the ligand solution ([Mal] = $7 \cdot 10^{-2}$ m bis $2 \cdot 10^{-1}$ m, $pH_C \sim 5.5$) at the same background electrolyte concentration and pH value.

Experiments with PCEs were carried out with PCE in the sample cell ([PCE] = 1 - 8 mg/g) and Eu(III) in the syringe ([Eu^{3+}] = $1 \cdot 10^{-3}$ - $6 \cdot 10^{-3}$ m) also at the same background electrolyte concentration (NaCl or $CaCl_2$) and pH value (pH_C between 4.0 and 6.5). The pH_C was controlled before and after the calorimetric titration to exclude changes of the protonation state of the PCEs and PA ligands.

The ionic strength dependent measurements were performed in a range from 0.5 to 2.5 m NaCl and in the case of PCEs also in 0.5 to 2.5 m $CaCl_2$. With regard to complexation, the protonation enthalpies of Mal, Lac and Oxa were determined in separate experiments. For this purpose, ligand concentrations of $1 \cdot 10^{-2}$ m to $2 \cdot 10^{-2}$ m ($pH_{H_2O} \sim 7$) and HCl concentrations of 0.1 m to 0.2 m were used.

n additions of the titrant produce *n* heat peaks, which give $\Delta Q_{ex,j}$ at each step *j* (with $1 \leq j \geq n$) after integration. The stepwise heats ΔQ_{ex} were corrected for the dilution heat of the titrant and the heat of stirring. The latter two ones were determined in separate experiments using blank solutions containing corresponding concentrations of sodium chloride or calcium chloride. The resulting net heat of reaction is $\Delta Q_{r,j}$.

The calorimeter was validated by measuring the enthalpy of the reaction of $CaCl_2$ with EDTA (in MES buffer at 25 °C and pH 5.6, Test Kit from GE Healthcare), which is well documented in the literature. The obtained value (-16.77 ± 0.19 kJ·mol^{-1}) is in excellent agreement with the literature data (-17.97 ± 1.80 kJ·mol^{-1}).

Data analysis

The integration of the $Q_{ex,j}$ heats was done using Origin 7[155] and NITPIC[156, 157] software. The CHASM[158], SEDPHAT[159] and HypDH[153] software were used to determine the complexing and protonation constants and the corresponding enthalpies.

The conditional molar $\Delta_r H_m$ and $\log \beta_m$ values of the complexation reactions were obtained by fitting the experimental heat with fixed conditional $\log \beta_m$ and $\Delta_r H_m$ of the respective protonation reaction. For the Nd(III)-Mal complexation two complex species with 1:1 and 1:2 stoichiometry and for the Eu(III)-Lac, Nd(III)-Oxa and Eu(III)-PCE complexation only one complex species were considered. The values of the ion product and the enthalpy of formation of water were taken from NIST database 46.6/7[175]. Each ITC experiment was performed at least twice and the values obtained were averaged.

3.7 Supplementary spectroscopic and analytical methods

3.7.1 UV-Vis spectroscopy

The UV-Vis studies with Nd(III) were carried out by using a Cary Variant 300 (Agilent Technologies Inc., USA). Aliquots of a 0.05, 0.1 or 0.5 m Mal solution were titrated into a ~ $1 \cdot 10^{-3}$ m Nd(III) solution at constant pH_c and measured in a 10 mm quartz cuvette (see Table 3.5 for experimental details of the UV-Vis series). At the end of the titration Mal concentrations of 0.01 m to 0.16 m were present. The *pH* series was performed in a 5 cm flow-through cuvette with [Mal] = 0.02 m. All spectra were recorded between 450 - 650 nm. The spectral resolution was 0.25 nm.

Table 3.5: Experimental details of the UV-Vis titrations. Concentrations were converted from molal to molar.

sampe/ serie	I_m / medium	*pH*-value	[M(III)] / mol·L^{-1}	[Mal]$_{total}$ / mol·L^{-1} [a]
Nd(III)-S1	0.5 m NaCl	3.9	$8.14\cdot10^{-4}$ – $1.01\cdot10^{-3}$	0 – $9.42\cdot10^{-2}$
Nd(III)-S2	0.5 m NaCl	5.7	$8.36\cdot10^{-4}$ – $9.88\cdot10^{-4}$	0 – $1.45\cdot10^{-2}$
Nd(III)-S3	0.5 m NaCl	5.9	$7.09\cdot10^{-4}$ – $9.88\cdot10^{-4}$	0 – $1.39\cdot10^{-1}$
Nd(III)-S4	0.5 m NaCl	5.6 – 1.5	$9.87\cdot10^{-4}$ – $9.97\cdot10^{-4}$	$1.98\cdot10^{-2}$ – $1.99\cdot10^{-2}$
Nd(III)-S5	0.5 m NaCl	2.2	$7.01\cdot10^{-4}$ – $9.99\cdot10^{-4}$	0 – $8.44\cdot10^{-2}$
Am(III)	0.3 m NaCl	0.9 – 6.0	$1.3\cdot10^{-3}$ –$1.2\cdot10^{-3}$	$2.0\cdot10^{-2}$ – $1.9\cdot10^{-2}$

[a] – [Mal]$_{total}$ is the concentration of malic acid or sodium salt independent of the protonation state

Am(III) absorption spectra (experimental details in Table 3.5) were recorded between 350 and 750 nm with 1000 accumulations using a multi-channel analyzer (Carl Zeiss MCS601, Jena, Germany) with a resolution of 0.8 nm/pixel. The deuterium halogen light source DH-2000 (Avantes, Eerbeek, Netherlands) was connected to the cuvette holder and the spectrograph by a fiber optic cable.
The Am(III)- and Nd(III)-absorption spectra were baseline corrected, normalized and analyzed using PARAFAC to determine stability constants (see chapter 3.5)

3.7.2 Infrared spectroscopy

Infrared spectroscopic experiments were performed with a Vertex 80/V vacuum FT-IR spectrometer (Bruker Optics Inc., USA) equipped with a mercury cadmium telluride detector. All experiments were performed under normal atmosphere at 24 ± 1 °C.

An attenuated total reflection unit (DURA SamplIR II, Smiths Inc.) with a horizontal diamond with nine internal reflections on top and an incidence angle of 45° was used for the measurements of the aqueous samples (as well as the Nd(III)-Mal solid). A flow cell with a volume of 200 µL was mounted to minimize interference with the background signal. The spectra were recorded with a spectral resolution of 4 cm^{-1}. First, the spectra of the pure Mal ligand at *pH* 1 to 13 were recorded as reference spectra. Complexation with Nd(III) was investigated at a fixed metal-ligand ratio of 1 : 1 (10^{-2} M) at I_M = 0.5 in the *pH* range from 1 to 6. All absorption spectra were obtained using a background spectrum of a pure electrolyte solution. To calculate the difference spectra, the single-channel spectra of the dissolved ligand measured at the same *pH* value were subtracted from the single-channel spectra of the solutions with metal ion and ligand (according to Lambert-Beer's law). Thus the positive and negative bands in the difference spectra represent oscillation modes of the Mal ligand in the presence and absence of Nd, respectively.

The CSH solid samples were prepared as KBr pellets and the spectra were recorded as transmission spectra with a spectral resolution of 4 cm^{-1}. A carbonation of the samples over the period of the measurement could be excluded. The CSH phases were mixed with 0.1 $mol \cdot L^{-1}$ of the respective additive having the same *pH* value, which was adjusted by adding 0.1 $mol \cdot L^{-1}$ NaOH to the CSH suspensions (see chapter 3.2).

3.7.3 NMR spectroscopy

The NMR measurements were performed at room temperature using a Bruker Ascend 800 MHz NMR spectrometer with a H/X MAS BL 3.2 sample head. The MAS rotation frequency is 15 kHz.

The ^{29}Si-MAS NMR spectra were recorded at a resonance frequency of 158.97 MHz with the following parameters: 15 kHz rotation speed; 500 scans; 3.25 µs pulse length; 360 s pulse recovery time. The observed ^{29}Si-resonances were analyzed using the Q^n classification, where one Si trahedra is bound to n further Si tetrahedra (n = 0 to 4).

The chemical shift in the ^{29}Si-NMR spectra was calibrated using DSS (2,2-dimethyl-2-silapentane-5-sulfonic acid, sodium salt) as the external standard (0.0 ppm). Adamantane was used for the referencing of ^{13}C and ^{1}H (29.5 ppm and 1.85 ppm, respectively).

The data acquisition and processing of the NMR spectra were performed with the software TopSpin 3.2 (Bruker, Germany) and the data analysis with the dmfit software[160]. The peak shape of the ^{29}Si-NMR spectra was fitted with a Gauss/Lorentz curve, the FWHM was ≤ 3 ppm. Two peaks each, for Q^1- and Q^2-tetrahedra were fitted. In this work, relatively narrow Si-signals are shown, which allow an integration with an error of 10 % after peak deconvolution.

From the intensities of the Si peaks, the mean main chain length (MCL) can be calculated using Equation 3.18. Here Q^2_p represents the paired, Q^{2B} the bridging and Q^2_u the tetrahedra, which are connected by a hydrogen bridge to another bridging Si tetrahedra (see Figure 2.2). It is assumed that one Q^2_p-and two Q^2_b tetrahedra are present (Q^2_p / (Q^2_b + Q^2_u) = 2).[161,162]

$$MCL = \frac{2\,(Q^1 + Q^2_p + Q^2_b + Q^2_u)}{Q^1} \qquad 3.18$$

^{27}Al-MAS NMR spectra were recorded with a resonance frequency of 208.5 MHz with a pulse length of 4 µs, a recycle delay of 2 s and an accumulation of 5000 scans. The chemical shift was calibrated externally to 0 ppm using $Al(NO_3)_3$(aq).

3.7.4 Thermal analysis

Thermogravimetric (TG) and differential scanning calorimetry (DSC) investigations were carried out with a STA 449 F5 Jupiter (Netzsch, Selb, Germany) instrument. For this purpose 20 - 40 mg of the sample were weighted and heated using a heating rate of 20 K/min from 25 to 1000 °C under an argon flow rate of 200 mL/min. The sample chamber was evacuated immediately after the positioning of the sample crucible and flushed with argon to prevent the sample carbonation. The onset temperature, peak

areas, the derivation and smoothing of the DSC curves were performed using the Netzsch Proteus TA software.

3.7.5 PXRD measurements

X-ray diffraction (XRD) measurements of the CSH/CAH powders were performed between 5° and 70° 2θ with a Bragg-Brentano diffractometer (Rigaku MiniFlex 600, Tokyo, Japan) using Cu Kα radiation and a graphite monochromator. The resolution was 0.02 - 0.03° 2θ with a scanning time of 1°/min. The diffractometer was calibrated before the measurements. An inert gas sample holder was used for the measurements. For the solid phase characterization, the ICDD PDF database was used.

3.8 Ab-initio molecular dynamics (AIMD) simulations

Ab-initio molecular dynamics (AIMD) simulations were performed using the FROG module implemented TURBOMOLE program.[163] A time step of 1 fs was chosen for the simulations. Initial velocities were set randomly according to a temperature of 300 K. The average temperature was adjusted by coupling the system to a Nosé-Hoover thermostat of 300 K.[164] The Nd(III) ion was described by an ECP49MWB f-in-core potential and corresponding basis sets in triple zeta quality.[165,166] On all other atoms, basis sets of double-zeta quality were used as a compromise between accuracy and feasibility. Density functional theory (DFT) calculations employing the BP86 function[167,168] were performed on the Nd(III)-aquo ion as well as the Nd(III)−MAL 1:1 and 1:2 complexes including three hydration shells. After an equilibration time of 0.5 ps and a sampling time of 3 ps, radial distribution functions of the Nd−O and Nd−C distances were computed.

The combinations of EXAFS experiments with quantum chemical calculations has already been successfully demonstrated for several systems [169,170,171,172,214]. The EXAFS spectra and the radial particle distribution function (RPDF) were calculated for each complex, while replacing Nd by Am (details in Taube et al.[186]).

3.9 Specific Ion Interaction Theory (SIT)

The complex formation of metal ions with a ligand L is described by the mass action law (Equation 3.19, the charges and the hydrate shells were neglected for better understanding):

$$M + nL \rightleftharpoons ML_n \qquad \beta_n = K_1 \cdot K_2 \cdot \ldots \cdot K_n = \frac{a_{ML_n}}{a_M \cdot a_L^n} \qquad 3.19$$

a –activity of the species, K_n – stability constant, β_n – stability constant of the complex ML_n

The activity a_p of the species p is linked to the concentration c_p by the following equation

$$a_p = \gamma_p \cdot c_p \qquad 3.20$$

a_p – activity of the species p; γ_p – activity coefficient of species p; c_p – concentration of species p

Only at infinite dilution the activity coefficient is equal to 1. Under real conditions, however, it depends on the ionic strength, pressure and temperature. Using the *Specific Ion Interaction theory* (SIT)[102] the determined conditional data $\log \beta'_{m,n}$ and $\Delta_r H'_{m,n}$ were extrapolated to zero ionic strength (standard state: $I_m = 0$; $T = 298{,}15$ K; $p = 1$ bar) under consideration of the following relations (Equations 3.21-3.25)

According to SIT the activity coefficients γ_p are calculated with Equation 3.21

$$\log \gamma_p = -z_p^2 \cdot D + \sum_k \varepsilon(i, k, I_m)\, m_k \qquad 3.21$$

γ_p – activity coefficient of the species p; z – charge of the ion i; D – Debye-Hückel-Term; ε – interaction coefficient between cation i and anion k; I_m – ionic strength [mol·kg^{-1}]; m – concentration [mol·kg^{-1}]

with D as Debye-Hückel term

$$D = \frac{A \cdot I_m^{1/2}}{1 + B \cdot a_i \cdot I_m^{1/2}} \qquad 3.22$$

A and B are Debye-Hückel-constants, a_i is a ion size parameter. $A = 0.509$ kg$^{1/2}$·mol$^{-1/2}$ and $B \cdot a_i = 1.5$ kg$^{1/2}$·mol$^{-1/2}$ at $T = 25°$ C

If $\log \gamma_p$ is substituted by Equation 3.21 in the mass action law (Equation 3.19), the linear SIT Equation 3.23 results.

$$\log \beta'_{m,n} - \Delta z^2 \cdot D = \log \beta^0_{m,n} - \Delta \varepsilon_n \cdot I_m \qquad 3.23$$

with

$$\Delta z^2 = \sum z^2_{Produkte} - \sum z^2_{Edukte} \qquad 3.24$$

and

$$\Delta \varepsilon_n = \sum_j \nu_j \cdot \varepsilon_n(i, k) \qquad 3.25$$

$\log \beta'$ – conditional stability constant; $\log \beta^0$ – thermodynamic stability constant; z – charge of the ion i; ν – stoichiometric coefficient

The stability constant $\log \beta^0_{m,n}$ ($I_m = 0$; $T = 298{,}15$ K; $p = 1$ bar) can be obtained by linear plotting of $\log \beta'_{m,n} - \Delta z^2 D$ vs. I_m by extrapolation from the intercept. The slope results in the specific sum interaction coefficient $\Delta \varepsilon_n$.

Due to the fact that the concentrations of the ions of the background electrolyte (in this work NaCl) are usually several orders of magnitude higher than the concentrations of the educts, only the molarities m_{Na+} and m_{Cl-} are considered for the interaction coefficients (in Equation 3.25). Thus, the ion interaction coefficients ε describe the specific short-range interactions of the ionic species with the respective counterion of the background electrolyte. They depend on the charge and the size of the ion. If the reactant i has no charge $\varepsilon = 0$

Similarly, standard enthalpies can be obtained using Equation 3.26

$$\Delta_r H'_{m,n} - \Delta z^2 \cdot D_L = \Delta_r H^0_{m,n} - RT^2 \, \Delta \varepsilon_{L,n} \cdot I_m \qquad 3.26$$

with

$$D_L = \frac{3}{4} \frac{A_L \cdot I_m^{1/2}}{\left(1 + B \cdot a_i \cdot I_m^{\frac{1}{2}}\right)} \qquad 3.27$$

$\Delta_r H'$ – conditional enthalpy of reaction; $\Delta_r H^o$ – thermodynamic enthalpy of reaction; z – charge of the ion i; D_L – enthalpic Debye-Hückel-Term; ε_L – enthalpy coefficient of interaction between cation i and anion k; I_m – ionic strength, A_L – enthalpic Debye-Hückel-constants with 1.986 kJ·kg$^{1/2}$mol$^{-1/2}$ and $B \cdot a_i$ = 1.5 kg^{½}·mol$^{-1/2}$ at T = 25° C

The enthalpic Debye-Hückel term D_L (Equation 3.27) is different from D (Equation 3.22). The relation between the specific enthalpy interaction coefficient $\varepsilon_{L,n}$ (i, k) and $\Delta\varepsilon_{L,n}$ (i, k) is analog to Equation 3.23. Similar to log $\beta^0_{m,n}$, $\Delta_r H^o_{m,n}$ can be obtained by linear plotting $\Delta_r H^o_{m,n} - \Delta z^2 D_L$ against I_m as an intercept. The slope is $\Delta\varepsilon_{L,n}$ (i, k).

Finally, the standard entropy $\Delta_r S^o_{m,n}$ and the free Gibbs energy $\Delta_r G^o_{m,n}$ can be calculated according to Equations 3.28 and 3.29 (Gibbs-Helmholtz Equation), respectively.

$$\Delta_r S^0_{m,n} = \frac{\Delta_r H^0_{m,n}}{T} + R \cdot lnK^0 \qquad \text{J·mol·K}^{-1} \qquad 3.28$$

$$\Delta_r G^0_{m,n} = \Delta_r H^0_{m,n} - T \cdot \Delta_r S^0_m \qquad \text{kJ·mol}^{-1} \qquad 3.29$$

R – ideal gas constant

4 Complexation reactions of An(III)/Ln(III) with organic ligands

4.1 Investigations by isothermal titration microcalorimetry

4.1.1 Malate, lactate, oxalate

Protonation reaction

The enthalpies, entropies and Gibbs energies of the protonation reactions of the ligands malate (Mal), lactate (Lac) and oxalate (Oxa) were determined by ITC. This is a requirement for studying the complexation reactions with Ln and An. For Oxa and Lac the ionic strength dependent ITC measurements published in[173] have been re-evaluated and reported in[25] together with the new results for Mal obtained in this project. Here, a short summary is given.

The calorimetric heat curves of the protonation reactions of the Mal and Lac at different ion strengths are shown in Figure 4.1 as a function of the respective molar ratios. Both ligands show exothermic protonation reactions and similar enthalpy values $\Delta Q_{r,j}$ at small HCl/ligand ratios at the same ionic strength. However, differences can be seen in the characteristics of the heat curves which can be explained by the different number of carboxyl groups of the ligands. In the case of Mal, therefore, two overlapping exothermic heat effects are observed, whereas one sigmoidal heat curve is shown for Lac which corresponds to one protonation reaction. Oxa also has two protonation steps, but the species H_2Oxa is only present under very acidic *pH* conditions ($\log K^{\circ}_{2} = 1.40 \pm 0.03$).[102] These conditions (*pH* < 2) cannot be realized with the used calorimeter (MicroCal iTC$_{<}$ „< Therefore only the complex enthalpy of the first protonation step $\Delta_r H^0_{1,HOxa}$ has been re-evaluated.[25]

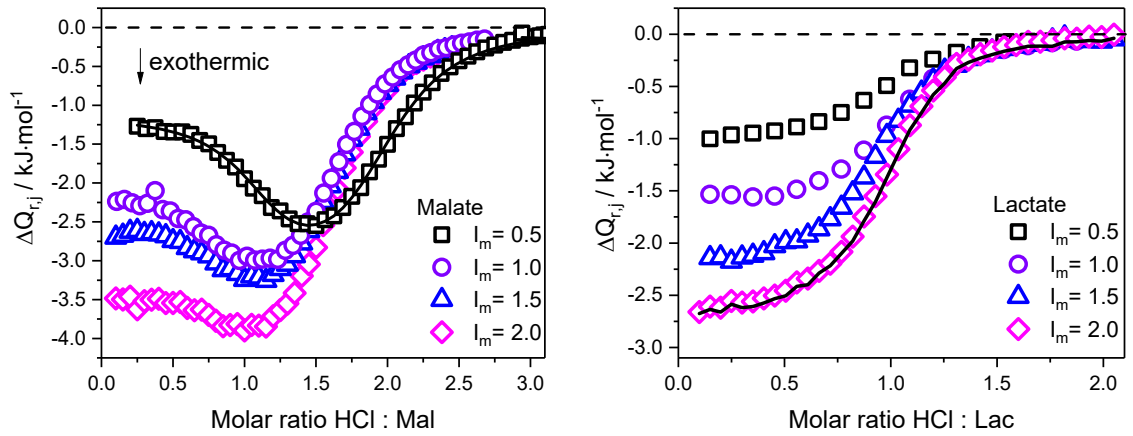

Figure 4.1: Calorimetric heat curves of the Mal and Lac protonation reaction at different ionic strengths with an example of a fitted curve (line), $\Delta Q_{r,j}$: integrated stepwise heat at the respective titration step *j*; $[Mal]_{ini} = 1{\cdot}10^{-2}$ m, $pH_C = 7.1$; $[Lac]_{ini} = 1{\cdot}10^{-2}$ m, $pH_C = 6.7$; [HCl] = 0.05 – 0.17 m

For the determination of the protonation enthalpies, the protonation constants were taken from the literature and kept constant for the fit of the heat curves in order to minimize the uncertainties of the fit (exception: for Oxa, log β and $\Delta_r H_m$ were determined simultaneously). The ionic strength-dependent plot of the determined conditional reaction enthalpies according to Equation 3.26 (SIT extrapolation, see chapter 3.9) is shown for the three ligands in Figure 5.2. From the negative slopes of the SIT extrapolation it can be seen that the enthalpy values of the protonation reactions become more exothermic with increasing ionic strength. The calculated extrapolated enthalpies $\Delta_r H^o_m$ and the specific sum interaction coefficients $\Delta\varepsilon_L$ of the protonation reactions of the three ligands are listed in Table 4.1 together with the calculated entropies $\Delta_r S^o_m$ and Gibbs energies $\Delta_r G^0_m$.

For Mal the reaction enthalpy $\Delta_r H^o_{m,1}$ of the first protonation step is endothermic, while $\Delta_r H^o_m$ is exothermic. For the protonation of Lac, no conditional $\Delta_r H'_m$ and $\Delta_r S'_m$ values in NaCl are available so far; only $NaClO_4^-$ and NaTf electrolytes were used for investigations.[117,174] The $\Delta_r H^o_m$ und $\Delta_r S^o_m$ values of the Lac protonation determined here in NaCl are in good agreement with literature values of the NIST database.[175] The determined enthalpy of the first Oxa protonation step shows a deviation of 8 % from the literature value of the NEA-TDB.[102] The deviations of the enthalpy values of the ligands (see Table 4.1) from the literature data may be caused by the use of the Van't-Hoff approximation (Equation 4.1) in the literature.[176,177] Here, according to Equation 4.1, log K^o_n vs. 1/T is plotted and $\Delta_r H^o_{m,n}$ and $\Delta_r S^o_{m,n}$ are determined from the slope or from the intercept, respectively. As result, the $\Delta_r H^o_{m,n}$ values are fitted over the examined temperature range and therefore, they are more prone to errors. For reactions, which show only a small temperature dependence, the direct calorimetric determination of enthalpies is more accurate.[178]

$$\log K_n^0(T) = \frac{-\Delta_r H^0_{m,n}}{R\ln(10)} \cdot \frac{1}{T} + \frac{\Delta_r S^0_{m,n}}{R\ln(10)} \qquad 4.1$$

R – ideal gas constant

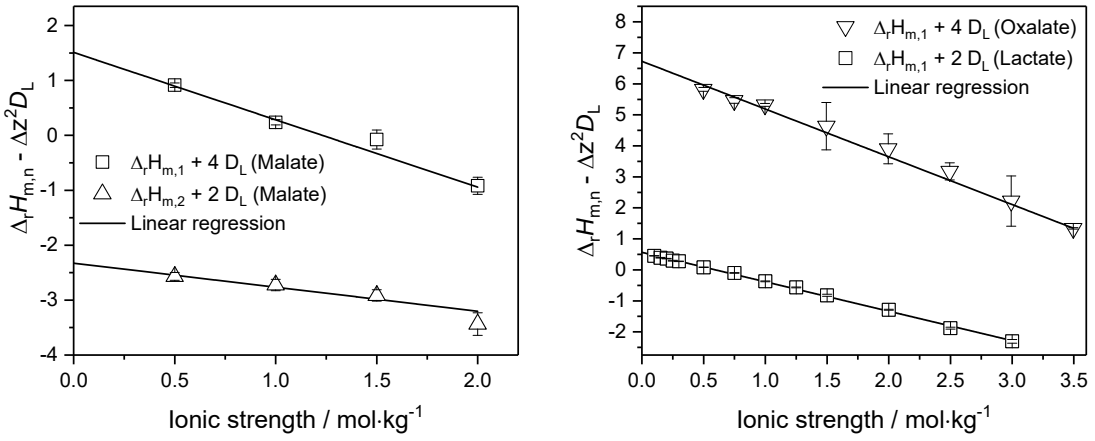

Figure 4.2: SIT extrapolation of the enthalpy values of the protonation reaction of Mal (left), Lac and Oxa (right)

Table 4.1: Determined standard thermodynamic data from the SIT extrapolation for Mal, Lac and Oxa protonation at $T = 25$ °C and $I_m = 0$ compared to literature values

reaction	$\Delta_r H^0{}_m$ / kJ·mol^{-1}	$\Delta\varepsilon_L \cdot 10^{-3}$ / kg·mol^{-1}·K^{-1}	$\Delta_r S^0{}_m$ / J·mol^{-1}·K^{-1}	$\Delta_r G^0{}_m$ / kJ·mol^{-1}
$H^+ + Mal^{2-} \rightleftharpoons HMal^-$	1.51 ± 0.18 1.18 ± 0.32*	1.7 ± 0.1	97.4 ± 0.4	−29.0 ± 0.1
$H^+ + HMal^-$ $\rightleftharpoons H_2Mal$	−2.33 ± 0.21 −2.92 ± 0.28*	0.6 ± 0.1	65.9 ± 0.4	−19.6 ± 0.1
$H^+ + Lac^- \rightleftharpoons$ HLac	0.56 ± 0.04 0.33#	1.29 ± 0.02	76 ± 4 75#	−22 ± 1 −22#
$H^+ + Ox^{2-} \rightleftharpoons$ HOxa$^-$	6.7 ± 0.1 7.3 ± 0.1$	2.09 ± 0.07 3.3 ± 0.2$	105 ± 2 105 ± 0.5$	−24.6 ± 0.6 −24.0 ± 0.2$

* – De Robertis *et al.*[179], # – NIST-data base[175], $ – NEA-TDB[102] in $NaClO_4$. All uncertainties were calculated according to OECD NEA-TDB recommendations and are shown in 2σ values[102]

The sum of the specific interaction coefficients $\Delta\varepsilon$ was determined from the slope of the SIT extrapolation of the protonation constant according to Equation 3.23 (see chapter 3.9) using data from De Robertis et al.[179] For Mal $\Delta\varepsilon_1$ is -0.158 ± 0.001 kg·mol^{-1} and $\Delta\varepsilon_2$ is -0.099 ± 0.004 kg·mol^{-1}. With these values and with ε (H$^+$, Cl$^-$) = 0.12 ± 0.01 kg·mol^{-1} (from NEA-TDB[102]) and ε (NaCl, H_2Mal) = 0 the ion interaction coefficients ε (Na$^+$, HMal$^-$) und ε (Na$^+$, Mal^{2-}) can now be calculated. They are listed in Table 4.2 together with values of similar ligands. The ion interaction coefficients of equally charged species of the considered ligands decrease in the order Lac > Mal > Oxa. The ion interaction coefficient ε (Na$^+$, Lac$^-$) does not correlate with ε(Na$^+$, Ace$^-$) for actetate (Table 4.2), as widely assumed in literature. The additional OH group of Lac (compared to acetate) has a significant influence on the ion interaction coefficients. This is also indicated by the differences of the ε (Na$^+$, Mal^{2-}) and ε (Na$^+$, Suc^{2-})-values as well as of the ε (Na$^+$, HMal$^-$)- and ε (Na$^+$, HSuc$^-$) values, respectively.

The specific enthalpic sum interaction coefficients $\Delta\varepsilon_L$ of the first protonation step increase in order Lac > Mal > Oxa corresponding to the endothermic nature of the protonation reaction (Table 4.1). The specific ion interaction coefficient of enthalpy ε_L cannot be calculated due to the lack of literature values.

Table 4.2: Specific ion interaction coefficients ε(i,k) for cation *i* and anion *k*.

Species	ε(i,k) / kg·mol^{-1}	Referenz
$\varepsilon(Na^+, HMal^-)$	−0.02 ± 0.01	d. A.[$]
$\varepsilon(Na^+, Mal^{2-})$	0.02 ± 0.01	d. A.[$]
$\varepsilon(Na^+, Lac^-)$	0.01 ± 0.05	[185]
$\varepsilon(NaClO_4, H_2Oxa)$	0.00 ± 0.01	[102]
$\varepsilon(Na^+, HOxa^-)$	−0.07 ± 0.01	[102]
$\varepsilon(Na^+, Oxa^{2-})$	−0.08 ± 0.01	[102]
$\varepsilon(Na^+,Lac^-)$/ $\varepsilon(Na^+,Ace^-)$[#]	0.08 ± 0.01	[180.183]
$\varepsilon(Na^+, HCit^{2-})$	−0.04 ± 0.02	[102]
$\varepsilon(Na^+, HSuc^-)$	0.02 ± 0.01	[181,182]
$\varepsilon(Na^+, Suc^{2-})$	0.09 ± 0.01	[181,182]

[$] – Calculated with literature data of Ref[179] [#] – Acetate (Ace) as analogous to lactate (Lac) as proposed in[183] . Suc – Succinate. Cit – Citrate. All uncertainties were calculated according to OECD NEA-TDB recommendations and are shown in 2σ values[102]

In accordance with literature values of similar small organic molecules[102,179,184] the protonation reactions are entropy-driven. i.e. the reactions are favored by a positive entropy change ($-T\cdot\Delta_r S_m$ is negative and $-T\cdot\Delta_r S^o_m > -\Delta_r G^o_m >> -\Delta_r H^o_m$). With increasing ionic strength, the contribution of entropy decreases while the contribution of enthalpy increases (here not shown, see also[25,185]) i.e. the driving force of the reaction changes towards an enthalpy-driven reaction. This is explained by the decreasing energy required for the partial dehydration of the reacting species during the protonation or complexation reaction at higher ionic strength. These findings are in good agreement to literature and more explanations are given in[25,110,178,179,184,185,186] and references therein.

Complexation reaction

As mentioned in the introduction, Mal was considered to be the major ligand, while Lac and Oxa play a minor role in these report. The complexation with Lac and Oxa were already investigated in the previous project[173], for Lac here an extended data set was determined. Lac was considered because its structural motif represents a subunit of Mal, Lac has one COOH group less than Mal. The determined thermodynmaic data are published in our reference[185]. Oxa was considered as a chelate ligand to consider the influence of ring size on the stability constant.

The Nd(III)-Mal, Eu(III)-Lac and Nd(III)-Oxa complexation were investigated as function of ionic strength by ITC to determine stability constants and complexation enthalpies. The determined protonation enthalpies (and protonation constans) of the ligands were used for the analysis of the ITC data. The heat curves of the Nd(III)-Mal complexation (Figure 4.3, left) and Am(III)-Mal complexation (Figure 4.3, right, for Pu(III) see Figure 7.1) show two main characteristics: At low Mal/Me(III) ratios a negative slope can be seen. At Mal/Me(III) ratios > 2 the heat curves show a positive slope which means the occurrence of second reaction independent of the first one. The speciation in Figure 4.3 (right, gray) was obtained by fitting of the heat curve. From this, it can be seen that the first slightly exothermic heat effect can be attributed to the 1:1 complex, while the second exothermic heat effect corresponds to the 1:2 complex.

At $I_m = 0.5$ (NaCl) the Nd(III)-Mal complexation begins in the positive $\Delta Q_{r,j}$-range i.e. it is initially endothermic (Figure 4.3, left). At higher I_m the reaction becomes exothermically. This transition from an endothermic to an exothermic complexation reaction with increasing ionic strength is also found in the Eu(III)-Lac[185] and the Nd(III)-Oxa[173] complexation reactions. Explanations of have already been given in[25,102,110,178,179,184,185].

For each investigated ionic strength conditional thermodynamic data log β_n, $\Delta_r H_{m,n}$ were obtain, which were used for the SIT extrapolation (Figure 4.4). The resulting standard thermodynamic data are summarized in Table 4.3. The Am(III)-Mal and Pu(III)-Mal complexation were not investigated as a function of ionic strength. Table 4.3 shows the conditional values for Am(III)-Mal complexes at I_m = 0.65, which were then converted to standard data using the SIT parameters of the Nd(III)-Mal system. The thermodynamic data of the Mal complexes of both metal cations Am(III) and Nd(III) are identical within the errors. This match confirms the analogy of the two cations with respect to their coordination properties.

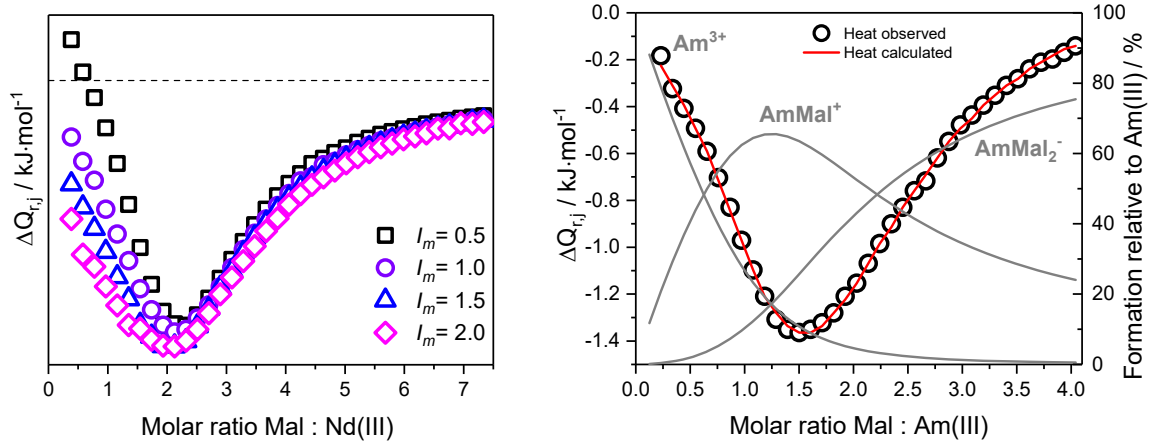

Figure 4.3: Calorimetric heat curves of Nd(III)-Mal titration at different ionic strengths; [Nd] = $2 \cdot 10^{-3}$ m; [Mal] = $7 \cdot 10^{-2}$ m; pH_C = 5.5 (left). Fitted (red) calorimetric heat curve (black) and speciation (grey) for Am(III) Mal titration; [Am] = $3 \cdot 10^{-3}$ mol·L^{-1} and [Mal] = $7 \cdot 10^{-2}$ mol·L^{-1}; pH_C = 5.5; I_M = 0.65 NaCl (right). $\Delta Q_{r,j}$ – integrated stepwise heat for each titration step j

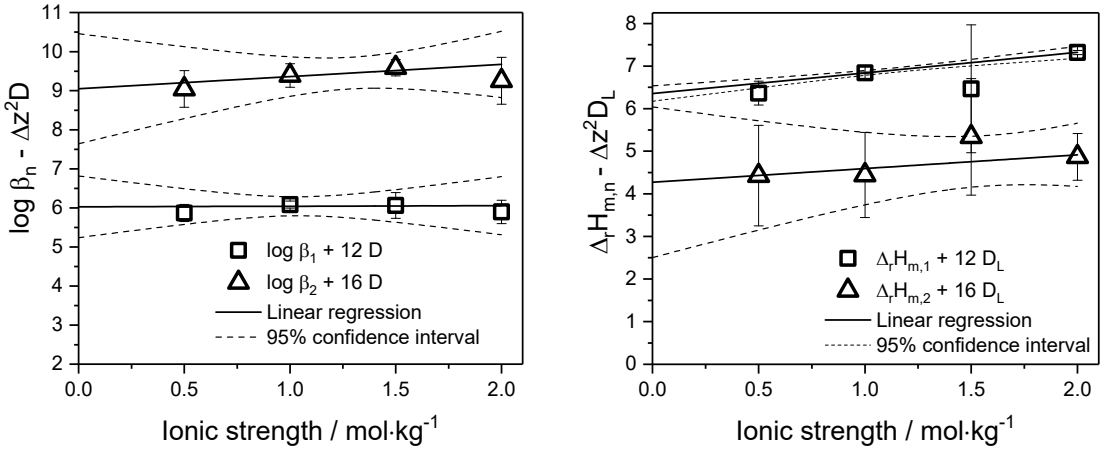

Figure 4.4: SIT extrapolation of the stability constants (left) and the enthalpy values (right) of the Nd(III)-Mal complexation

Since there are no standard data for Ln(III)/An(III)-Mal complexes in the literature so far, standard data of similar organic systems are considered to compare the results (see Table 7.3). The Cm(III) succinate complexation shows smaller complexation constants than the Nd(III)-Mal complexation (log β^0_1 = 5.13 ± 0.13 und log β^0_2 = 7.48 ± 0.16 from[182]) This seems plausible with respect to the similar ligand structure, which only differs in the α–hydroxyl group. A contribution of the α–hydroxyl group of Mal to the Nd(III) coordination can explain the stronger complexation of Mal (see chapter 4.2.3, IR studies). The even stronger complexation of the Ln(III)/An(III) citrate system is plausible due to the additional carboxyl group of citrate.[187] Consistently, the complexation of the monocarboxylic acid, propionic acid, is weaker than the Mal-complexation.[188] Therefore the stability constants of the Nd(III)-Mal complexes are a strong indication that Mal forms a chelate ring similar to succinate and citrate.

Oxa also forms a chelate ring, with both carboxylate groups stabilizing the metal in a 5-membered ring (side-on coordination).[123] Lac has also been identified as a chelating ligand which forms a 5-membered ring with Eu(III).[110] Obviously, the stabilization of a 5-membered ring by a hydroxyl group, as present in Lac, is less efficient than stabilization by the two carboxylate groups of Oxa. This is reflected in the much smaller complex formation constant of the 1:1 Eu(III)-Lac complex. This compared to the 1:1 Nd(III)-Mal complex indicates that the Mal complex is stabilized by a 5-membered chelate ring and an additional chelate ring.

For Mal the overall enthalpies for both complexation steps $\Delta_r H^o_m$ are endothermic and in the same range as those of the Cm(III) complexation with acetate[188] and dicarboxylic succinate[123]. The standard enthalpy of the first Nd(III)-Mal complex is more endothermic than that of the 1:1 Eu(III)-Lac complex (Table 4.3). This can be attributed to the size of Mal and the corresponding larger hydration shell compared to Lac, which means, that more energy must be expended for the dehydration of Mal. The second stepwise reaction enthalpy of the Nd(III)-Mal complexation is −2 ± 1 kJ·mol^{-1}. Consequently, for the second complexation step less dehydration energy is needed. The $NdOxa^+$ complex has a slightly negative reaction enthalpy. This can be caused by a higher binding strength, whereby a lower solvation means a less strongly bound solvation shell of the oxa ligand.

The high entropy values of Nd(III)-Mal complexes (much higher than the values for the monocarboxylic acetate[189] and propionate[188]) are consistent with the high values of the Nd(III)-Mal stability constants: Mal forms chelate complexes with Nd(III), similar to succinate, citrate and oxalate.

Figure 4.5 shows the fractions of $\Delta_r H_m$ and $-T\cdot\Delta_r S_m$ relative to $\Delta_r G_m$ of the first step of Nd(III)-Mal and Eu(III)-Lac complexation as a function of I_m. It can be seen that both complexation reactions are favored exclusively by the change of the reaction entropy (entropy driven reaction) at $I_m = 0$. The fractions of $\Delta_r H_m$ and $-T\cdot\Delta_r S_m$ relative to $\Delta_r G_m$ are changing with increasing ionic strength similar to the protonation reactions. The contribution of the enthalpy increases by ~ 20 % up to $I_m = 2$ - 3 m NaCl due to the changes in the dehydration processes already described in[25,102,110,178,179,184,185].

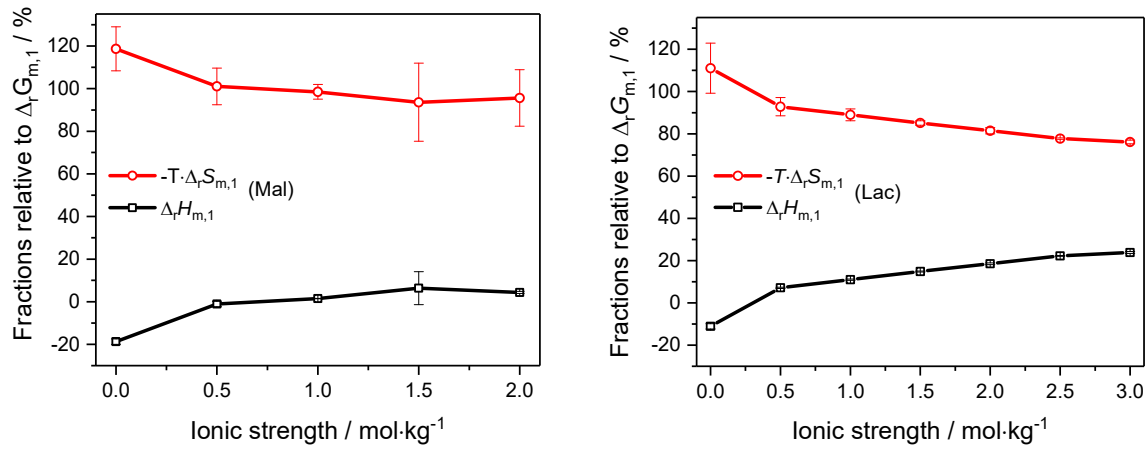

Figure 4.5: Fraction of $\Delta_r H_m$ and $-T\cdot\Delta_r S_m$ in relation to $\Delta_r G_m$ of the 1:1 Nd(III)-Mal-complexation (left) and of the 1:1 Eu(III)-Lac-complexation (right) as fuction of I_m.

To calculate the specific ion interaction coefficients ε_1 ($NdMal^+$, Cl^-) and ε_2 ($NdMal_2^-$, Na^+) ε (Nd^{3+}, Cl^-) $\approx \varepsilon$ (Eu^{3+}, Cl^-) = 0.23 ± 0.02 was assumed as recommended by NEA-TDB[102] and ε (Na^+, Mal^{2-}) from Table 4.2 and the respective $\Delta\varepsilon_{o,n}$-values from Table 4.3 were used. The values listed below have been calculated to the recommendation of the NEA-TDB[102], uncertainties are reported at the 2σ level:

$$\varepsilon_1\,(NdMal^+, Cl^-) = 0.2 \pm 0.2\ \ kg{\cdot}mol^{-1}$$

$$\varepsilon_2\,(NdMal_2^-, Na^+) = -\,0.04 \pm 0.24\ kg{\cdot}mol^{-1}$$

These specific ion interaction coefficients ε_n are slightly higher than the values determined for the Cm(III) succinate and oxalate system but follow the same trend: They all decrease with increasing complexation degree.[182] The specific ion interaction coefficients $\varepsilon(EuLac^{2+}, Cl^-)$ and $\varepsilon(NdOxa^+, Cl^-)$ are 0.08 ± 0.11 kg·mol^{-1}K^{-1} and 0.02 ± 0.28 kg·mol^{-1}K^{-1}, respectively (for details see[25])

The use of the enthalpic SIT equation yields the enthalpic sum interaction term $\Delta\varepsilon_L$ of the complexing reactions (Table 4.3). Since no further $\Delta\varepsilon_L$ values are found in the literature, no specific enthalpy values ε_L(X, Na^+/Cl^-)-values can be calculated.

Table 4.3: Thermodynamic standard data from the SIT extrapolation for Nd(III)-Mal-, Am(III)-Mal-, Eu(III)-Lac- und Nd(III)-Oxa-complexation at $T = 25$ °C and $I_m = 0$.

n	$\log \beta^0_n$	$\Delta_r H^0_{m,n}$ / kJ·mol^{-1}	$\Delta_r S^0_{m,n}$ / J·mol^{-1}·K^{-1}	$\Delta_r G^0_{m,n}$ / kJ·mol^{-1}	$\Delta\varepsilon_n$ / kg·mol^{-1}	$\Delta\varepsilon_{L,n} \cdot 10^{-3}$ / kg·mol^{-1}K^{-1}
$Nd^{3+} + n\,Mal^{2-} \rightleftharpoons Nd(Mal)_n^{3-2n}$						
1	6.0 ± 0.4	6.4 ± 0.1	137 ± 7	−34 ± 2	−0.02 ± 0.34	−0.66 ± 0.07
2	9.1 ± 0.7	4.4 ± 0.9	188 ± 13	−52 ± 4	−0.31 ± 0.24	−0.4 ± 0.5
$Am^{3+} + n\,Mal^{2-} \rightleftharpoons Am(Mal)_n^{3-2n}$ bei $I_m = 0{,}65$						
1	3.9 ± 0,1	−0.4± 0,2	73 ± 2	−22 ± 1		
2	6.6 ± 0,2	−6 ± 1	109 ± 4	−38 ± 1		
$Am^{3+} + n\,Mal^{2-} \rightleftharpoons Am(Mal)_n^{3-2n}$ bei $I_m = 0$**						
1	6.1 ± 0.3	5.8 ± 0.5	136 ± 6	-35 ± 2		
2	9.4 ± 0.5	3 ± 1	190 ± 20	-54 ± 6		
$Eu^{3+} + n\,Lac^{-} \rightleftharpoons Eu(Lac)_n^{3-n}$						
1	3.8 ± 0.3	2.4 ± 0.2	74 ± 3	−19.9 ± 0.9	−0.16 ± 0.10	0.92 ± 0.17
1	3.48 ±0.15[#]	1.65 ± 0.90[#]	71.2 ±6.38[#]	−19.85 ±2.80[#]	−0.13 ± 0.06[#]	0.94 ± 0.14[#]
1	3.14 ± 0.28*	9.3 ± 6.2*	92 ± 29*	−18.2 ± 6.2*		
$Nd^{3+} + n\,Oxa^{2-} \rightleftharpoons Nd(Oxa)_n^{3-2n}$						
1	6.2 ± 0.6	−6.0 ± 1.8	99 ± 23	−36 ± 7	−0.29 ± 0.28	−2.9 ± 0.6
1	6.51 ± 0.15[§]				−0.33 ± 0.10[§]	
1	6.86 ± 0.03[$]	−2.7 ± 1.8[$]	121.8 ± 2.9[$]	−39 ± 2[$]	−0.206 ± 0.008[$]	

** – extrapolated using the SIT parameters of the Nd(III)-Mal system; [#] – from Skerencak *et al.* [185]; * – from Barkleit *et al.* [110] in Perchlorate; [§] – values of the Am(III)-Oxa system from the NEA-TDB[102] ; [$] – values of the Cm(III)-Oxa system from Skerencak-Frech *et al.* [123] at 20 °C. All uncertainties were calculated according to OECD NEA-TDB recommendations and are shown in 2σ values[102]

4.1.2 Polycarboxylate-ether (PCE)

For the first time the complexation of Eu(III) by polycarboxylate-ether and sodium polyacrylate (PA) as a PCE model compound were studied as function of ionic strength using ITC. The investigated PCEs are summarized Table 7.1 and Figure 4.6.

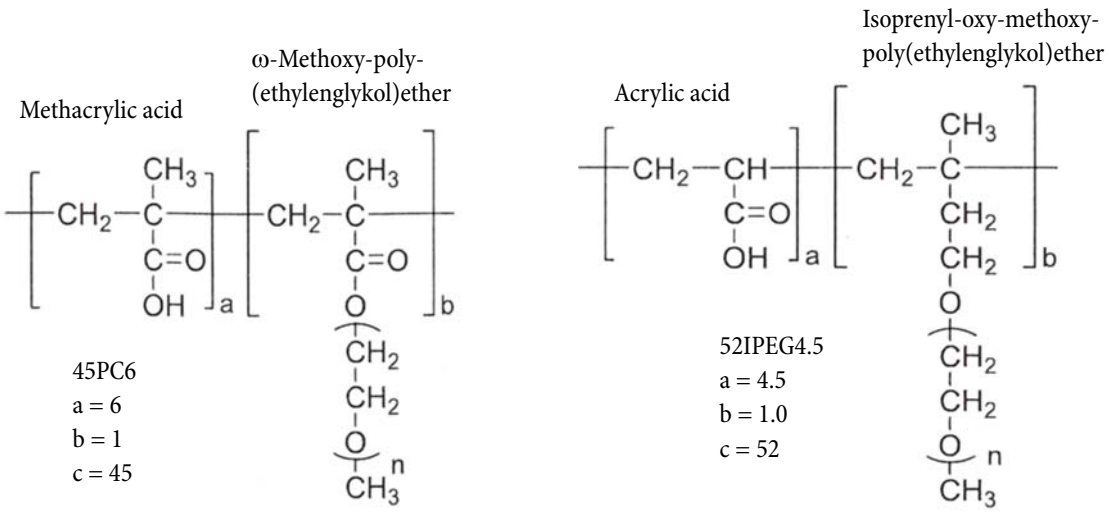

Figure 4.6: Used synthetic polycarboxylate-ether (obtained via the group of Prof. Dr. P. Panak , Physikalisch-Chemisches Institut, Ruprechts-Karls-Universität Heidelberg, synthesized by group of Prof. Dr. J. Plank, Lehrstuhl für Bauchemie, TU München)

Figure 4.7 shows representative thermograms and calorimetric heat curves for Glenium®[51] and for the synthetic PCE 45PC6 binding to Eu(III). All investigated PCEs and PA show a strong endothermic reaction with Eu(III) indicated by positive peaks in the heating power, which become smaller with additional injection of Eu(III) due to the increasing saturation of the Eu(III)-PCE complexation. The integrated heat curves are s-shaped, which at the first glance indicate a 1:1 complex formation. However, at the beginning of the calorimetric titrations deviations from the typical sigmoidal curve shape of a pure 1:1 complex formation can be observed (see in Figure 4.7 fitted heat curves). These deviations are significant, not within the uncertainties of the method. Possibly, they are caused by further complexation or transformation reactions of the PCEs. The *pH* values of the samples measured before and after ITC experiments remained constant. Thus, significant changes in the protonation state of the ligands can be excluded. Furthermore, in all investigated PCEs and PA the ITC signals show no hints to kinetically controlled processes or precipitation.

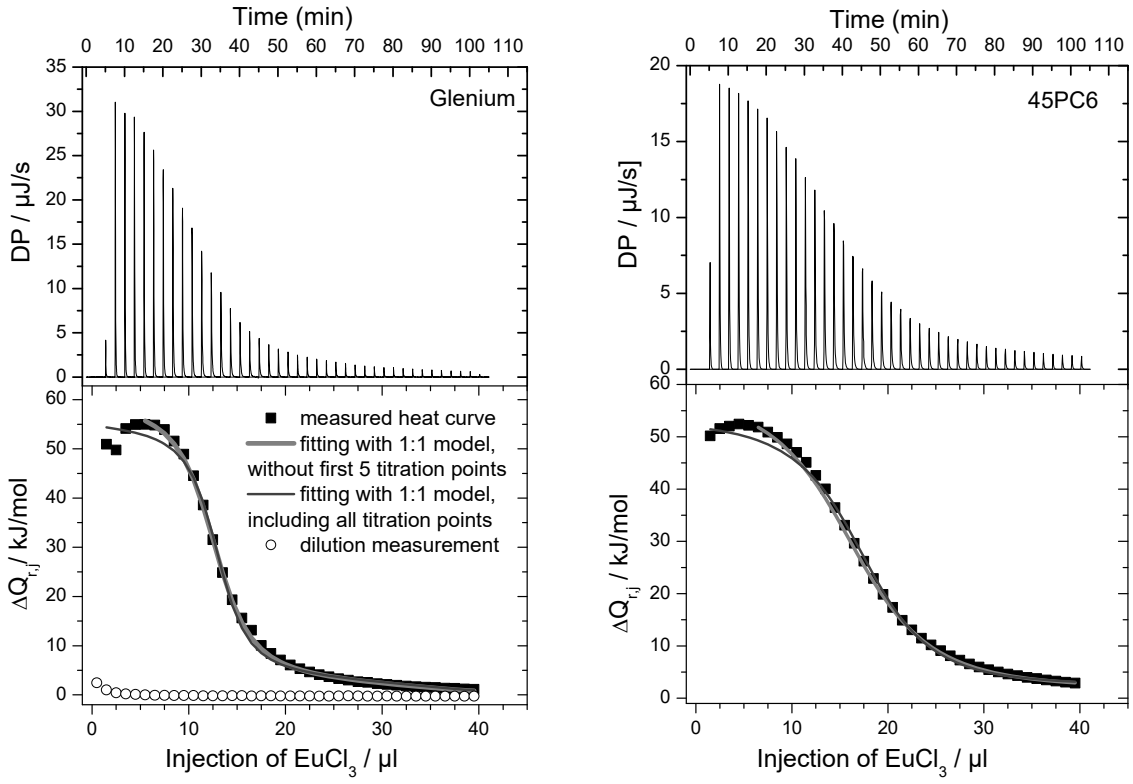

Figure 4.7: Thermogram (top) and calorimetric heat curves (bottom) of addition of Eu^{3+} to Glenium®51 (left) and 45PC6 (right), $[Eu^{3+}] = 4{\cdot}10^{-3}$ m, [Glenium®51] = 3 mg/g, [45PC6] = 3 mg/g, I = 0.1 m NaCl, $pH_c = 6.0$
Heat curves were corrected for the dilution heat of the titrant Eu^{3+} in 0.1 m NaCl and for the injection (stirring) heat of addition 0.1 m NaCl in the PCE solution. Both provide a negligible contribution to the total heat absorbed on each addition of Eu^{3+} to the PCE in the sample cell.

As seen in Figure 4.8, the measured calorimetric heat curves of the PCEs and PA show dependencies on the ionic strength. With increasing ionic strength the heat being released with every injection step decreases, whereby this effect is more pronounced in the $CaCl_2$ medium than in NaCl.

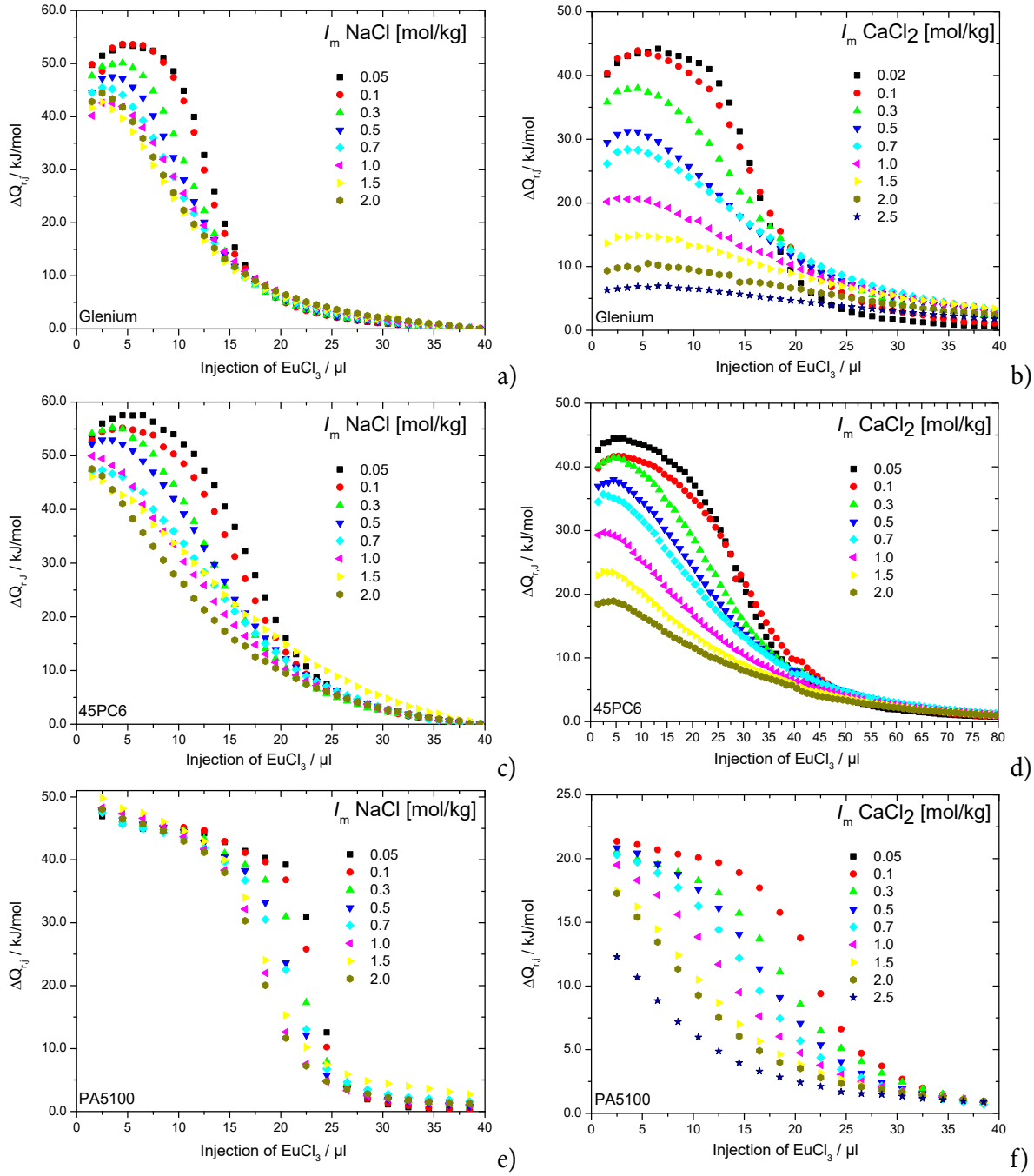

Figure 4.8: Examples of calorimetric heat curves of the addition of Eu^{3+} to Glenium®[51] (top a and b), synthetic PCE 45PC6 (middle c and d) and sodium polyacrylate PA5100 (bottom e and f) as function of ionic strength of NaCl (left a, c, e) and $CaCl_2$ (right, b, d, f); Glenium®[51]: $[Eu^{3+}] = 4{\cdot}10^{-3}$ m, [Glenium®[51]] = 3 mg/g, $pH_c = 6.0$; 45PC6: $[Eu^{3+}] = 4{\cdot}10^{-3}$ m, [45PC6] = 3 mg/g, $pH_c = 6.2$; PA5100: for NaCl $[Eu^{3+}] = 4{\cdot}10^{-3}$ m, [PA5100] = 0.3 mg/g, $pH_c = 6.5$; for $CaCl_2$ $[Eu^{3+}] = 6{\cdot}10^{-3}$ m, [PA5100] = 0.45 mg/g, $pH_c = 5.2$

Heat curves were corrected for the dilution heat of the titrant Eu^{3+} in the medium with the corresponding ionic strength and for the injection (stirring) heat of addition of medium in the ligand solution with the corresponding ionic strength. Both provide a negligible contribution to the total heat absorbed on each addition of Eu^{3+} to the ligand in the sample cell. The curves are shown on the molar scale, for the analysis the molal scale was used (with conversion factors from[102,190]).

TRLFS and EXAFS studies of the complexation of PCE and PA with Eu(III) and Cm(III) have revealed only one complex species at $pH < 6$: a 1:1 complex with a An^{3+}/Ln^{3+}-coordination by three carboxylic groups in a bidentate end-on-fashion.[124,125,126,191] However, it cannot be completely excluded that there is more than one binding environment for the Eu(III) ion in the Eu(III)-PCE and Eu(III)-PA complexes. The binding of Eu(III) to carboxylate groups with slightly different environment can still result in different binding enthalpies. Various factors, such as pH value, molar ratio and concentrations of the reactants, background electrolyte and its ionic strength influence strongly the formation of the Eu(III)-PCE/PA complexes. But currently, no reliable (structural) data of Eu(III)-PCE/PA complexes of higher order are available. Therefore, the analysis of the ITC curves was carried out under the assumption of a 1:1 complex with the program SEDPHAT[159]. Besides the determination of the conditional stability constants and enthalpy values, also the effective concentration of the ligand was fitted. The total concentration of Eu(III) was kept constant. Global fits of up to three ITC experiments including samples with different ligand and/or Eu(III) concentration but with the same pH_c and ionic strength were performed. For an improved fitting of the heat curves, the first 2 to a maximum of 5 titration points were not included in the fits (see also in Figure 4.7 fitted heat curves). This has only little impact on the values to be fitted. The deviations are less than 3 % and thus significantly smaller than the experimental error which can be up to 10 % between multiple measurements.

The determined conditional stability constants and enthalpy values for Glenium®51, 45PC6 and PA5100 are summarized in the Table 4.4, Table 7.4 and Table 7.5, respectively. The conditional stability constants decrease considerably with increasing ionic strength by an average of one order of magnitude between the lowest and the highest used ionic strength. There are no significant differences in log K between the electrolytes NaCl and $CaCl_2$ as well as between the ligands. Furthermore, the stability constants decrease with decreasing pH_c, shown exemplarily for Glenium®51 in Table 7.6 for 0.1 m NaCl. It has been also found that in the pH_c range from ~ 5.5 to ~ 6.7 (here the carboxyl groups are mainly deprotonated) the conditional stability constants are almost constant within the errors of about log K_{11} ± 0.4 at constant ionic strength.

The determined conditional stability constants for all investigated PCEs and for the sodium polyacrylate are in the same order of magnitude of log K_{11} between ~ 4.5 and 5.5 (at I_m = 0.1 m). They are 1-2 orders of magnitude smaller than the constants obtained in [124,125,126] by TRLFS measurements. Possible reasons for these differences could be, first, the used concentrations of trivalent metal ion (ITC: mM; TRLFS: tracer to µM), and second, the different models for the calculations of the constants (ITC: 1:1 complexation, direct determination of the effective ligand concentration from the fitting of the ITC heat curves; TRLFS: calculations of the complexation constant with the charge neutralization model). Our constants are comparable with the log β_{11} values from Hahn et. al.[192] (ranging from 6.8 to 4.5 in 0.1 NaCl, based on a simple single site model) obtained for different humic substances, which are also naturally occurring polycarboxylic macromolecules and known to play an important role for a mobilization of actinides in a disposal of radioactive waste.[192]

Table 4.4: Conditional stability constants and enthalpy values of the complexation of Eu(III) with Glenium®51 as function of ionic strength of NaCl and $CaCl_2$ at $T = 25$ °C

I_m / mol·kg^{-1}	$pH_{exp} \pm 0.05$	log $K_{11} \pm 2\sigma$	$\Delta_r H_{11} \pm 2\sigma$ / kJ·mol^{-1}	$pH_{exp} \pm 0.05$	log $K_{11} \pm 2\sigma$	$\Delta_r H_{11} \pm 2\sigma$ / kJ·mol^{-1}
	NaCl, $pH_c = 6.10 \pm 0.05$			$CaCl_2$, $pH_c = 5.78 \pm 0.05$		
0.1	5.98	4.9 ± 0.1	63 ± 2	5.68	4.7 ± 0.1	47 ± 2
0.3	5.73	4.7 ± 0.2	62 ± 2	5.44	4.3 ± 0. 2	*49 ± 3*
0.5	5.58	4.6 ± 0.2	60 ± 2	5.40	4.1 ± 0.2	*44 ± 3*
0.7	5.44	4.4 ± 0.2	65 ± 2	5.35	4.1 ± 0.2	*39 ± 5*
1.0	5.37	4.3 ± 0.2	60 ± 2	5.21	3.9 ± 0.3	*31 ± 4*
1.5	5.26	4.2 ± 0.3	65 ± 4	5.15	3.9 ± 0.3	*22 ± 5*
2.0	5.21	4.1 ± 0.3	67 ± 4	5.14	3.9± 0.3	*14 ± 5*
0.1[124] a)	$[H^+]_{total} = 8 \cdot 10^{-5}$ mol·kg^{-1}	7.52 ± 0.33	2.7 ± 13.3			
0.1[193] b)	6	4.6				

a) T = 20 °C, TRLFS, data analyzed with charge neutralization model by Kim and Czerwinski[194]

b) 152-Eu radiotracer and ultrafiltration, data analyzed with charge neutralization model by Kim and Czerwinski[194]

The interaction of Eu(III) with PCEs/PA is strongly endothermic and consequently driven by entropy ($T \cdot \Delta_r S$ exceeds the $\Delta_r H$ by far) which is primarily due the release of water from the first hydration spheres around the Eu(III) ions and also due the exchange of three Na^+ ion or 1.5 Ca^{2+} ions by one Eu(III) ion. The total amount of released water molecules is given by the dehydration of the Eu^{3+} ions and COO^- groups minus the partial rehydration of the released Na^+ or Ca^{2+} ions. Enthalpy and thus entropy values tend to be slightly lower in the $CaCl_2$ solutions than in the NaCl solutions (see Table 7.7 for the entropy values). This can be related to the different contributions of the (re)hydration of Na^+ and Ca^{2+}: The hydration number for the sodium is 5 or 6 water molecules, whereas the hydration number of Ca^{2+} varies between 6 and 8. Na^+ has a stronger interaction with its first hydration shell than Ca^{2+}, which has a more flexible structure of the hydration shell.

In the NaCl solutions and for the PA ligand in both media, changes in enthalpy and entropy are not as pronounced with increasing ionic strength. Probably in this case the influence of the ionic strength on the hydration spheres of the polymer polycarboxylates and thus on the dehydration energy and water release is less strong. For the PCEs in the $CaCl_2$ solutions, a clear decrease of the enthalpy and entropy values at higher ionic strength (at > 0.7 m) is observed.

In general the determined enthalpy values are much larger compared to those calculated via van't Hoff equation from the spectroscopic data in[124,125] (see Table 4.4 and Table 7.4).

The enthalpy via the van't-Hoff equation reflects the enthalpy which is directly associated to the complexation that causes the change of the spectroscopic signal. The enthalpy change measured by ITC is an overall property of the system. This might include enthalpy contributions from nonspecific effects or reactions which are not part of the complexation equilibrium itself (which is observed by spectroscopy), but are mediated by the Eu(III).

In general, in polyelectrolyte/multivalent metal ion systems additional metal ion-induced reactions may be possible, e. g.:

- encapsulation of the metal ion by several carboxylate groups before the final complexation
- transformation from initial monodentate to bidentate coordination of metal ion (intramolecular complexation) or vice versa
- phase transformations or structural changes coupled with continued collapse of the metal ion-PCE-polymer, whereby the remaining binding sites for the metal ion are buried in the inner hydrophobic coils of the polymer
- cross-linking of polymer chains via the interaction of metal ion with the carboxyl groups (metal ion can act as cross-linker to form a polymer-network)

The complex formation and additional metal ion-induced reactions can occur simultaneously, so that the single peak in the ITC data reflects all effects. In our ITC studies such effects to the measured overall enthalpy cannot be excluded. A quantification of these effects via additional, separate ITC experiments was not possible. The heat contributions of the non-specific effects such as dilution of Eu(III) in pure medium and injection of medium in the pure ligand solution were determined in separate experiments. Both provide only a negligible contribution to the total heat released by each addition of Eu(III) to the ligand in the sample cell.

These thermodynamic studies using titration calorimetry show that the interactions of Eu(III) with polycarboxylate-ether superplasticizer have a medium strong complexation strength decreasing with ionic strength. This means that the complexation of trivalent actinides with superplasticizers will decreases with higher ionic strength. The enthalpy of the interactions is clear endotherm but almost ionic strength independent. At present, it is not clear which other heat-releasing/absorbing processes besides the complexation reaction are involved in the interaction of Eu(III) with polycarboxylate-ether based superplasticizers.

4.2 Spectroscopic studies on the Ln(III)/An(III)-Malate complexation

4.2.1 UV-Vis spectroscopy

Five UV-Vis titration series of the Nd(III)-Mal complexation were analyzed: four titration series with Mal at fixed pH_c values (pH 2.2, 3.9, 5.7 and 5.9) and one at fixed Mal concentration in a pH range of 1.5 to 5.6 (experimental details of the UV-Vis series in Table 3.5). Using a global factor analysis (PARAFAC) of all measured series, spectra of the individual components and their stability constants were determined. Three pure component spectra were determined (Figure 4.9). The Nd(III)-aquo ion shows a characteristic band at 575.0 nm with a shoulder at 578.5 nm corresponding to the hypersensitive $^4I_{9/2} \rightarrow {}^4G_{5/2}$, $^4G_{7/2}$-transition.[195,196] During the complexation with Mal, this band is bathochromic shifted. For the 1:1 Nd(III)-Mal complex the maximum of the band is 577.0 nm (shoulder at 579.8 nm), whereas the 1:2 Nd(III)-Mal shows a maximum at 578.8 nm (shoulder at 580.8 nm). Similar shifts can be observed for the spectral transition around 520 nm.

A first PARAFAC analysis was performed with fixed protonation constants (taken from De Robertis et al.[179]). The determined complexation constants are $\log \beta_1 = 3.6 \pm 0.2$ and $\log \beta_2 = 5.5 \pm 0.3$ (Table 4.5 and Figure 4.9). In a second PARAFAC analysis the protonation constants of Mal were optimized as well. Here, the resulting complexation constants and the first protonation constant $\log \beta^H{}_1$ are identical to the previous analysis, the second protonation constant $\log \beta^H{}_2$ is significantly smaller. This parameter has probaly only a minor influence on the UV-Vis data. However, since the complexation constants do not change, the $\log \beta^H{}_2$ value obviously has only a small influence on the spectra and the obtained thermodynamic data.

The determined stability constants agree well with the ITC results (chapter 4.1.1). Thus these two independent methods, titration calorimetry and photometry, complement each other well.

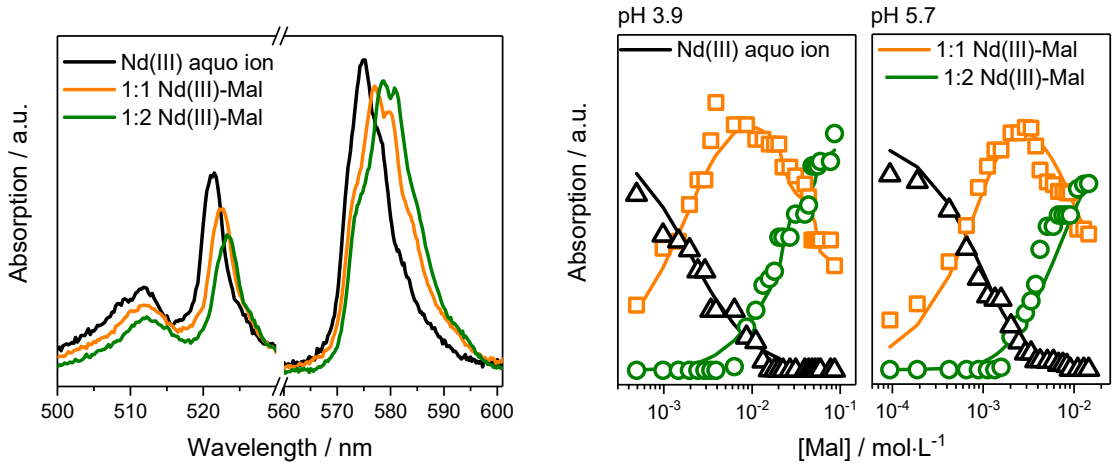

Figure 4.9: Global analysis of Nd(III)-Mal UV-Vis spectra using PARAFAC: normalized single component spectra (left) and the corresponding speciation of two titration series (right). The points represent the experimental data and the lines represent the corresponding PARAFAC modelling.

Our conditional stability constants differ significantly from literature values at similar ion strengths (Table 4.5 and Table 7.2). They show differences of almost one log unit. Depending on the background electrolyte and the stoichiometry's on which the analyses are based, the literature values itself show great differences. Sukhno et al.[197] and Ali et al.[198] included the protonated species $Nd(HMal)^{2+}$ and $Nd(HMal)_2^{+}$ (up to *pH* 7) for their calculations. However, the chelate bond in a 7-ring, which was supported by IR and EXAFS (see following chapters), makes the existence of these species very unlikely. The existence of a 1:3 complex is controversially discussed in the literature.[107,199] In our PARAFAC analysis with the inclusion of the 1:3 complex, the fitting of the experimental data could not be improved. Therefore the formation of a 1:3 complex cannot be confirmed here.[25] Furthermore, in the majority of publications only potentiometric titrations are described. This method is not suitable for buffering systems such as Mal, because the *pH* curves usually do not show any characteristic features.[200] This means that the uncertainties of the data obtained by potentiometric titrations intrinsically increased for such buffering systems.

Table 4.5: Protonation and stability constants determined from the UV-Vis spectra using PARAFAC for the Nd(III)/Am(III) Mal-complexation at I_m = 0.5 und T = 25 °C compared to ITC data

$\log \beta^H_1$	$\log \beta^H_2$	$\log \beta_1$	$\log \beta_2$	Bemerkungen
4.48 ± 0.01	7.64 ± 0.01	3.6 ± 0.2	5.5 ± 0.3	global analysis 1: Nd(III) protonation constants fixed[179]
4.5 ± 0.1	6.8 ± 0.3	3.6 ± 0.2	5.5 ± 0.4	global analysis 1: Nd(III) protonation constants non fixed
		3.9 ± 0.4 §	6.4 ± 0.7 §	
		4.7 ± 0.7	7 ± 2	results for Am(III), I_m = 0.25, p.w
		4.3 ± 0.4§	6.8 ± 0.7§	
		3.7 ± 0.2	5.7 ± 0.3	mean values from TRLFS studies with PARAFAC analysis

§ – Conditional Nd(III)/Am(III) Mal data from the ITC investigations interpolated to the respective ionic strength. All uncertainties were taken from the literature or calculated according to the recommendations of the OECD NEA-TDB and are shown in 2σ values. [102]

UV-Vis titrations were also carried out with Am(III) (but with a limited number of series). In the presence of Mal, a continuous bathochromic shift of the hypersensitive transition $^7F_0 \rightarrow {}^5L_6$ from 504 nm to 507 nm with increasing pH_c is observed (Figure 4.10). The stability constants from the PARAFAC analysis are listed in Table 4.5 in comparison with the Nd(III)-Mal data at the same ionic strength. The stability constants for Am(III) from UV-Vis and ITC measurements agree within the errors with those of Nd(III).

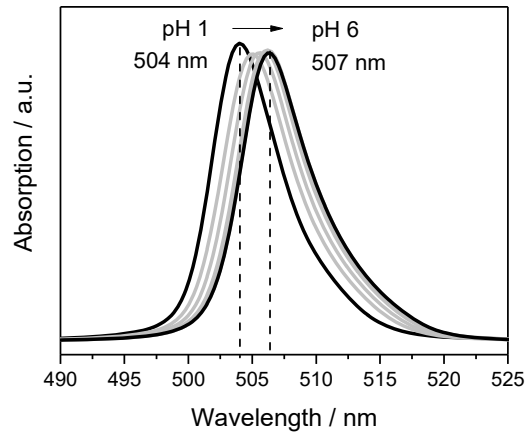

Figure 4.10: Normalized UV-Vis spectra of the Am(III) Mal titration of pH 1 – 6, $[Am]_{ini} = 1.3 \cdot 10^{-3}$ mol·L^{-1} und [Mal] = $2 \cdot 10^{-2}$ mol·L^{-1}, I_m = 0.25

4.2.2 Time-resolved laser-induced fluorescence spectroscopy

It is known, that Nd and Eu form isostructural complexes with carboxylic acids[201,202], so that complementary analysis using TRLFS can be performed with Eu(III) which was applied due to its excellent fluorescence properties.

The Eu(III) emission spectra (Figure 4.11, left) show significant changes due to complexation of Eu(III) with Mal: The peak of the forbidden $^5D_0 \rightarrow {}^7F_0$-transition appears at ~ 578 nm. The intensity of the hypersensitive $^5D_0 \rightarrow {}^7F_2$transition increases while the peak of the $^5D_0 \rightarrow {}^7F_1$transition is only slightly affected. Consequently, the $^5D_0 \rightarrow {}^7F_2/{}^5D_0 \rightarrow {}^7F_1$-ratio increases from ~ 0.5 (which is in good agreement with literature values for the Eu(III)-aquo ion[187,203,204]) to ~ 2.4. This is identical to the $^5D_0 \rightarrow {}^7F_2/{}^5D_0 \rightarrow {}^7F_1$- ratio of the Eu(HCitrate)$_2^{3-}$-complex.[187] There are no shifts in the fluorescence spectra.

The PARAFAC analysis shows that a fitting with 2 complex species is sufficient for a description of the experimental data. This is in accordance with the ITC and UV-Vis data (see the respective chapters above). The determined mean stability constants from several TRLFS titrations agree well with those of the ITC and UV-Vis measurements (see Table 4.5) assuming of 1:1 and 1:2 complex stoichiometry (Figure 4.11, right). In addition, the PARAFAC analysis gives the fluorescence lifetimes of the pure species (Table 4.6). The fluorescence lifetime the Eu(III)-aquo ion is in good agreement with corresponding literature values.[205,206,207,208] During complexation, the lifetime increases with increasing ligand concentration or increasing *pH* due to the exchange of the quenching water molecules surrounding the luminescent metal cation. The fluorescence lifetime of the 1:1 Eu(III)-Mal complex with 177 ± 28 µs corresponds to a number of 5 - 6 water molecules in the first hydration shell of Eu(III). This means that 3 - 4 water molecules have been replaced by one Mal molecule. This is comparable to the Eu(III)-citrate system, in which a similar lifetime of 165 ± 10 µs was found for the 1:1 complex. Here, comparable to Mal, 3 water molecules are replaced by one citrate molecule.[187] The fluorescence lifetime of the 1:2 Eu(III)-Mal complex shows that 5-6 water molecules are replaced by two Mal ligands, which is consistent with the number of replaced water molecules in the first complexation step.

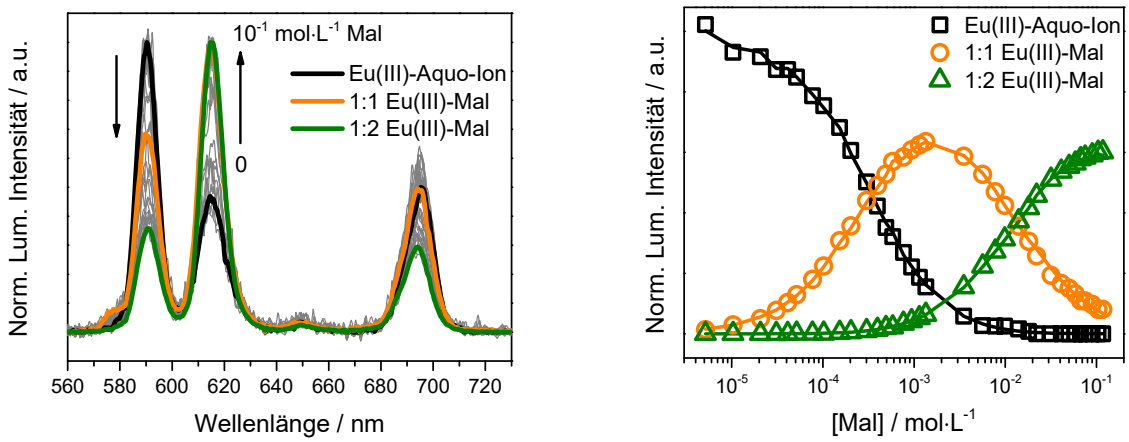

Figure 4.11: Normalized emission spectra and the corresponding single component spectra of the Eu(III) mal titration at pH 4.0 (left) and the speciation obtained from PARAFAC analysis (right). The dots represent the experimental data and the lines represent the corresponding PARAFAC modelling.

Table 4.6: Fluorescence lifetimes determined from TRLFS measurements using PARAFAC for the Eu(III)-Mal complexation at I_m = 0.5 (NaCl) and T = 25 °C

***pH*-value**	**τ_1 / µs**	***n*(H_2O)***	**τ_2 / µs**	***n*(H_2O)***	**τ_3 / µs**	***n*(H_2O)***
4.0	111 ± 3	9.0	157 ± 28	6.2	277 ± 32	3.2
1.2 – 6.4	111 ± 8	9.1	197 ± 18	4.8	261 ± 45	3.5
specis	Eu(III)-aquo ion		1:1 Eu(III)-Mal		1:2 Eu(III)-Mal	

* – uncertainty of $n(H_2O)$ ± 0.5, all other uncertainties are showed at 2σ values.

4.2.3 Infrared spectroscopy

The analysis of the possible configuration of Mal in the An(III)/Ln(III)-Mal complexes was extensively investigated by IR and EXAFS spectroscopy (latest, see next chapter).

The three functional groups of the Mal molecule, two carboxyl and one α hydroxyl group, are potentially available for coordination with a metal cation. According to the geometry and the resulting steric properties of the ligand, seven possible configurations of the 1:1 metal complex have to be considered (Figure 4.12): a monodentate or bidentate coordination of a carboxyl group (A or B), 5- and 6-membered ring structures (C or D) and 7-membered chelate ring structures with and without participation of the (deprotonated) hydroxyl group (E, F and G).[25]

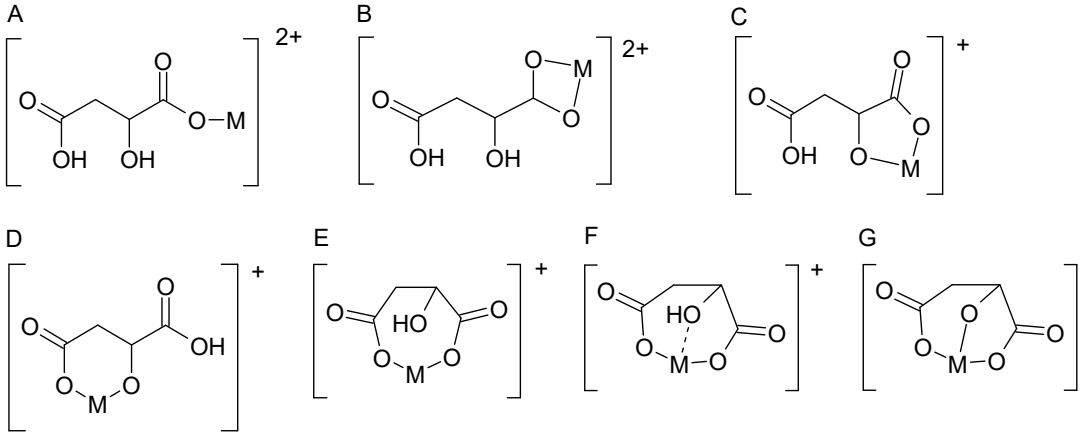

Figure 4.12: Possible configurations of Mal in complexes (M = Ln(III)/An(III)), only the 1:1 complex was considered. [25]

The spectra of the pure ligand and the Nd(III)-Mal complexes dissolved in background electrolyte solution were recorded in the pH_c 1-6. Since the absorption spectra of the Nd(III)-Mal solutions may still contain fractions of uncomplexed Mal, the difference spectra were calculated from the spectra of the solutions containing the Nd(III)-Mal complexes and the pure malate solutions at the respective pH_c according to the Lambert-Beer law. These spectra show positive and negative bands representing the vibrational modes of the complex and the uncomplexed Mal, respectively, and thus indicate spectral

differences of the Mal ligand due to the formation of the Nd(III)-Mal complexes (Figure 4.13). The assignments of the observed bands to the vibrational modes of Mal are summarized in Table 4.7.

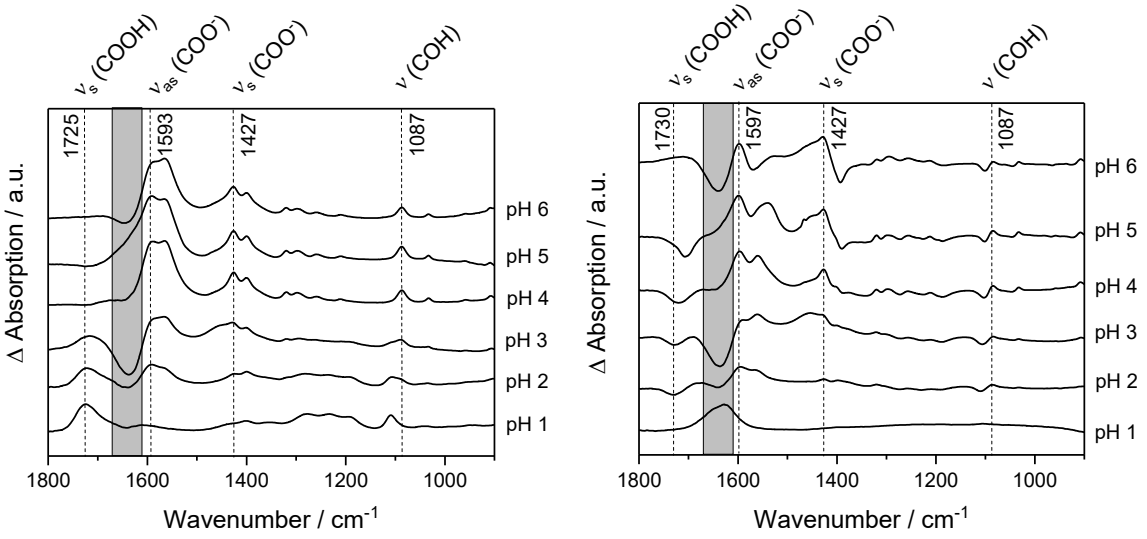

Figure 4.13: IR absorption (left) and difference spectra (right) of solutions with 10^{-2} m Nd(III) and 10^{-2} m Mal at $I_m = 0.5$ in the *pH* range of 1 – 6. The reference solution of the absorption spectra are the aqueous background electrolyte solutions. Difference spectra show only spectral changes due to Nd(III) complexation (for details see[186]). The spectral region in which solvent oscillations are expected is marked in grey.

Table 4.7: Observed frequencies of the band maxima and their assignment to the vibration modes of Mal. (+) indicate maxima of the bands of the difference spectra. Values are given in cm^{-1}.

Malic acid (H_2Mal)	**Malate, single protonated ($HMal^-$)**	**Malate diprotonated (Mal^{2-})**	**Nd(III)-Mal complex**	**Tentative assignment**
1727				$\nu(C_1OOH)$
	1718			$\nu(C_4OOH)$
	1580	1568	1593(+)	$\nu_{as}(C_1OO)$
		1568	1565(+)	$\nu_{as}(C_4OO)$
	1402	1395	1427(+)	$\nu_s(C_1OO)$
		1395		$\nu_s(C_4OO)$
	1104	1096	1087(+)	$\nu(C_2OH)$

A complexation of Mal with Nd(III) is shown in the vanishing of the ν(COOH) band at 1725 cm^{-1} at $pH_c > 3$. In the region of carboxylate vibrations, additional bands appear at 1593 and 1427 cm^{-1}, which can be clearly attributed to a coordination with Nd(III) due to their frequency shift compared to the pure Mal spectra. The observed spectral splitting of these $\nu(COO^-)$ bands of 195 cm^{-1} suggests a monodentate coordination of the carboxylate groups to Nd(III).[187,209,210,211] The participation of both carboxylate groups in the coordination of the Nd(III) ion can be derived from the difference spectrum at pH_c 5 (Figure 4.13, right). At this pH_c, which is close to the second pK_a of 4.5, the deprotonated Mal^{2-} is the dominant species (~ 80%) while the single protonated species $HMal^-$ plays a minor role, but it is still present. The negative band at 1707 cm^{-1} in the difference spectrum indicates clearly the deprotonation of the COOH group during the complexation with Nd(III). Thus, it can be assumed that both carboxyl groups are involved in the Nd(III)-Mal complex. A more detailed interpretation of the IR spectra of pure malate and the Nd(III)-complex as a function of pH_c and the derivation of the possible structural model is given in[186].

Finally, from the IR spectra it can be concluded that the Nd(III) cation is monodentately complexed via the carboxyl group(s) of the Mal ligands with contribution of the α–hydroxyl group. The hydroxyl group is protonated during complexation over the whole pH_c range. Furthermore, a complexation of Nd(III) in a chelate ring formed by the both carboxyl groups of Mal is very likely. Therefore, the structural model F in Figure 4.12 is assumed to be the most likely configuration of the Nd(III)-Mal complex.

4.2.4 EXAFS spectroscopy and quantenchemical AIMD calculations up to 6

The EXAFS spectra recorded in the pH_c range 1-6 and their Fourier transformations (FT) show only small spectral differences (Figure 4.14)[186]. Thus, only by using a comprehensive numerical analysis such as ITFA (*iterative transformation factor analysis*[212]) spectral information of the individual species can be obtained. ITFA allows a decomposition of a series of spectra into linear independent spectra and the determination of pure components (here referred to as species), even if these do not occur purely and/or the spectral changes are only small. The successful determination of the structure of aqueous Am(III) complexes using ITFA has already been demonstrated in lactate, acetate and formate systems.[119,213,214]

The EXFAS spectra are decomposed into their eigenvectors. Only the first two eigenvectors show spectral features, which means that two species are sufficient to reproduce the experimental spectra (Figure 4.15). The species can be assigned to coordinating water molecules and the Mal ligand. These two species change their coordination numbers (CN) depending on the pH_c value due to exchange reactions. The so-called VARIMAX factor loadings, which represent a kind of species distribution (resulting from the second step of the ITFA analysis), show that at pH_c 1 and 6 the water molecules and the Mal ligand have their maximum fraction, respectively. A mainly monodentate coordination of the carboxylate groups of Mal can be derived from a qualitative analysis of the eigenvectors.

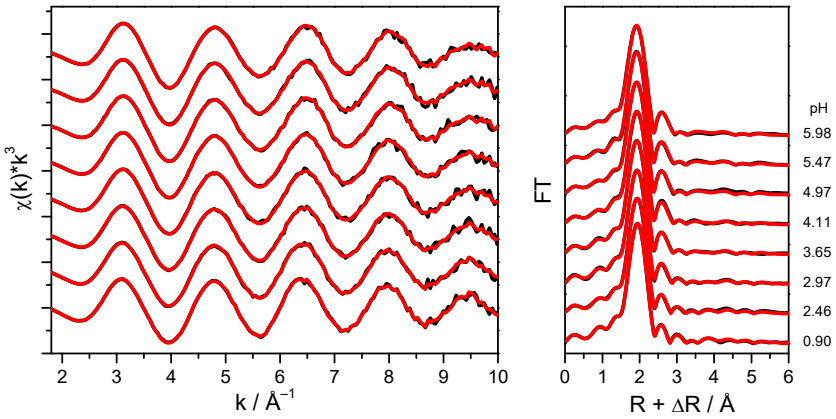

Figure 4.14: Experimental (black) Am L_{III}-edge EXAFS spectra (left) and spectra reproduced by ITFA (red) assuming two components. Corresponding Fourier Transformations (FT) (right).

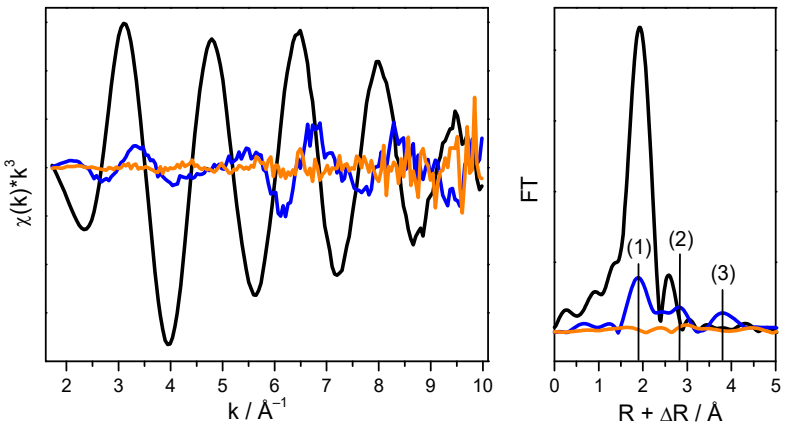

Figure 4.15: Am L_{III}-edge EXAFS- spectra (left) of the first three eigenvectors and the corresponding Fourier Transformations (right). Black - first eigenvector, blue - second eigenvector, orange - third eigenvector. The numbers in the FT show structural features. For a better representation, the amplitude of the first eigenvector has been reduced by a factor of 3.

A more precise analysis of the structure of both species can be obtained by fitting the EXAFS spectra (at pH_c 1 and 6) reproduced from the (shell fit). For the FEFF calculations, the averaged structure of the Am(III)-Mal$(H_2O)_6(H_2O)_n$-complex from the *ab-initio Molecular Dynamics* (AIMD) simulations was used (Table 7.8). The shell fits of the two reproduced spectra at pH_c 1 and 6 and the determined structural parameters are shown in Figure 4.16 and Table 4.8 respectively.

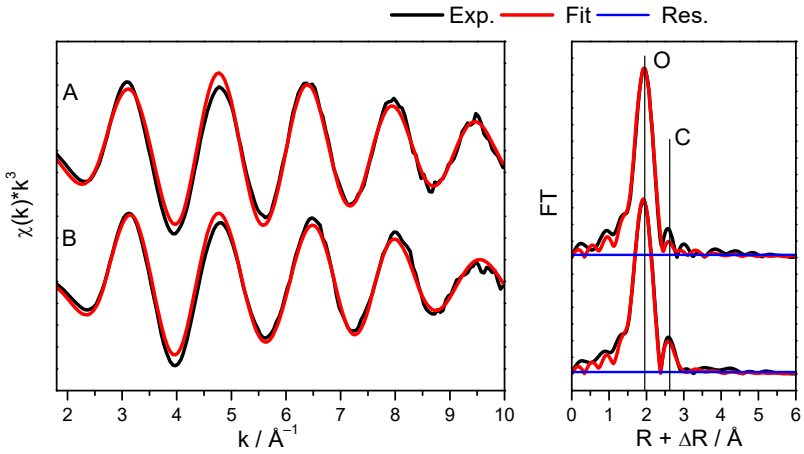

Figure 4.16: ITFA reproduced EXAFS spectra (left, black) of the samples at *pH* 1 (A) and *pH* 6 (B) and corresponding FT (right) with Shell Fit (red). The background noise level (blue) was estimated from the R-range between 15 Å – 25 Å

Table 4.8: Structural parameters of the reproduced EXAFS spectra of the Am(III)-aquo ion and the Am(III)-Mal species at pH_c 1 and 6, respectively, and the experimental spectral components 1 and 2 isolated from ITFA, assuming the tridentate AIMD structure.

Sample	**path**	**CN**	**R / Å**	**σ^2 / Å²**	**ΔE_0 / eV**
Am(III)-hydrate (pH_c = 1)	Am–O	8.5(2)	2.481(1)	0.0092(3)	11.68(6)
Am(III)-Mal (pH_c = 6)	Am–O	7.7(2)	2.461(2)	0.0096(4)	11.2(1)
	Am–C	4.1(7)	3.33(1)	0.012(3)	11.2[†]
species 1*	Am–O	1.1(2)	2.483(1)	0.0102(3)	11.70(6)
species 2[§]	Am–O	2.93(8)	2.453(2)	0.0098(4)	10.4(1)
	Am–C	2.0(3)	3.35(1)	0.013(3)	10.4[†]

* – a coordinated water molecule; [§] – a coordinated ligand; [†] – linked to the respective O-shell, CN – coordination number, *R* - interatomic distance, σ^2 – Debye-Waller factor, ΔE_0 – energy shift. The standard deviation of the fitted parameters is given in brackets. Amplitude reduction factor S_0^2 = 1.0.

The structural parameters of the reproduced spectrum at pH_c 1 are in very good accordance with those previously observed for the Am(III)aquo-ion.[119,213,214] At pH_c 6 a moderate decrease in the CN ((ΔCN_O = 0.8) and the averaged radial distance ((ΔR_O = 0.02 Å) of the Am(III)-O shell can be observed (Table 4.8) caused by the coordination of Mal. Similar Am-C distances were derived previously for the Am(III) formate and Am(III) lactate system where the carboxylate groups are monodentately coordinated. The results of the shell fit support the assumption that, here, the carboxyl group(s) of Mal also coordinate

monodentately to the metal ion. This allows model B, the bidentate binding model in Figure 4.12, to be excluded. Furthermore, model A is also excluded, since this configuration would result in a smaller CN_C than the determined CN_C of 4 under consideration of the highest complex stoichiometry of 1:2 (Am(III)/Mal) (results from ITC, TRLFS and UV-Vis measurements). The determined CN_C indicates the formation of a chelate ring in the complex (models C - G in Figure 4.12)

The investigation of a possible involvement of the OH group in the Am(III)-Mal coordination was achieved by a twin-tracked approach. On track is based on the shell fit of the ITFA isolated spectra. The other track is based on a direct comparison of the theoretically calculated EXAFS spectra from XRD structural data and from ab initio molecular dynamics simulation (AIMD). AIMD calculations were carried out for the Nd(III)-aquo ion, for the 1:1 and 1:2 Nd(III)-Mal complex both coordinated in a tridentate fashion (Table 7.8). For further analysis, Nd(III) was replaced by Am(III). Since AIMD calculated structures contain no or incorrect information on structural disorder (Debye Waller factor, amplitude function), which are required for the calculation of theoretical EXAFS spectra, the theoretical spectra cannot be compared directly with the experimental spectra. Therefore, a simple approximation was applied, in which the EXAFS amplitude function of the experimental spectra can be transferred to the theoretical spectra. A detailed description of these calculations and the procedure for obtaining theoretical EXAFS spectra from AIMD calculations is given in Taube et al.[186]

For the isolation of the species using ITFA, the number of coordinating water molecules (N_W) and Mal (N_{Mal}) must be specified in two spectra to ensure the uniqueness of the rotation for the iterative target test (ITT). For component 1 (pH_c 1) $N_W = 9$ and $N_{Mal} = 0$ was assumed while for component 2 (pH_c 6) two tridentate-bound Mal molecules ($N_{Mal} = 2$) replace six water molecules. During the complexation CN_O is decreased to 8 (Table 4.8), resulting in $N_W = 2$ at pH_c 6. The species extracted from ITFA also represent a bound water molecule (component 1) and a bound Mal ligand (component 2). The ITFA isolated spectra, the associated shell fits and the determined structural parameters of species 1 and 2 are shown in Figure 7.2 and Table 4.8 respectively. For species 1, all EXAFS structural parameters except CN_O are in agreement with those previously observed for the Am(III)-aquo ion. The determined CN_O of 1 supports the ITFA assumption that species 1 corresponds to one coordinated water molecule. For species 2, R_O is slightly shorter than in the Am(III)-aquo ion (pH_c 1) and in the Am(III)-Mal complex (pH_c 6), reflecting the exchange of water molecules by Mal ligands. The average $R_C = 3.39$ Å (average of C_1, C_2 und C_3 in Figure 4.17, right) of the nearest C-atoms from the AIMD structure is in good agreement with the measured R_C of 3.34(1) Å (Table 4.8). Thus, only a tridentate coordination mode (models F and G in Figure 4.12) is consistent with determined structural parameters.

Furthermore, there is also a good agreement between the theoretical EXAFS spectra, the corresponding FT (calculated using the AIMD structure) and the ITFA-isolated spectra in the fingerprint region from 3.24 to 4.48 Å (Figure 4.17). Small changes in the molecular structure would cause a different peak shape of the FT in this area. Considering the results from IR measurements[25], which show a protonation of the OH group up to a pH_c of 6, a tridentate coordination of malate involving the α-OH group is assumed to be the best possible coordination (model F in Figure 4.12 and Figure 4.17, right).

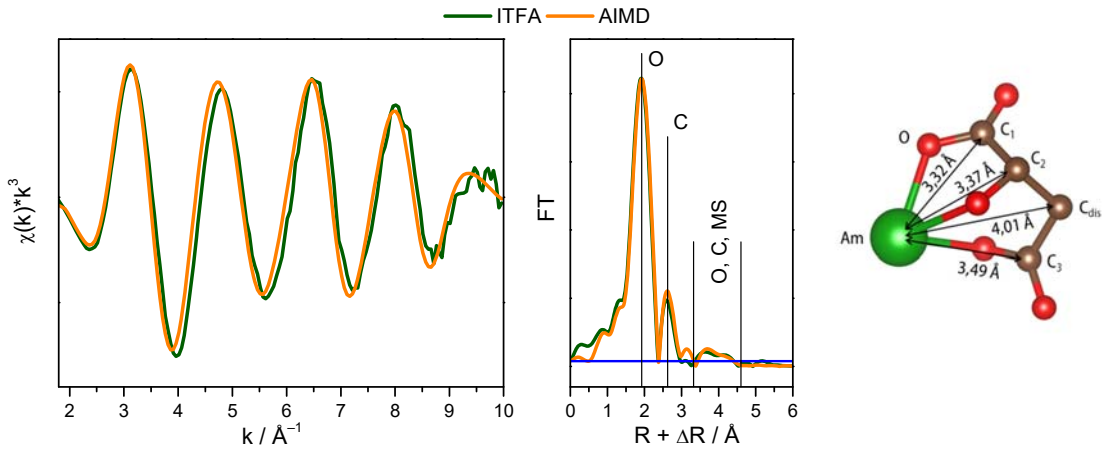

Figure 4.17: ITFA isolated EXAFS spectrum (left, green) of species 2 (a coordinated Mal ligand) assuming the AIMD structure of the tridentate Am(III)-Mal complex. Theoretical EXAFS spectrum calculated using the AIMD structure (left, orange), associated Fourier Transformations (FT) (center). The background noise (blue) was estimated from the R-range between 15 Å - 25 Å. AIMD structure of the 1:1 Am(III) Mal complex (right). The given values correspond to the Am(III) bond distances. Nd(III) was replaced by Am(III), H atoms were neglected.

Finally, the CN determined by ITC or UV-Vis measurements (complex stoichiometry) can be directly compared to CN of water molecules (CN_W) and Mal ligands (CN_{Mal}), because in addition to the spectra, the *pH*-dependent average CN of the individual species can also be obtained (Figure 4.18). For the calculation of the thermodynamically based CN_W and CN_{Ma} from ITC/UV-Vis measurements, it was assumed that each mal ligand replaces three water molecules (according to the AIMD structure in Figure 4.17) and that the overall coordination number decreases from 9 to 8 in the 1:1 and 1:2 complex. This results in CN_W: CN_{Mal} ratios of 9:0, 5:1 and 2:2 for the Am(III)-aquo ion, the 1:1 and the 1:2 Am(III)-Mal complexes, respectively. The CN_{Mal} based on the two approaches, namely the thermodynamic data and the EXAFS data, are in good agreement (Figure 4.18) and reflect the overall consistency between the two methods. At pH_c 2 - 3 larger deviations occur for CN_W, which can be caused by the assumption of the total number of coordinated water molecules for the 1:1 and 1:2 Am(III)-Mal complexes. The number of calculated water molecules from TRLFS measurements (lines in Figure 4.18) shows a deviation of ± ~ 1 for the 1:2 complex compared to the ITFA results. This deviation is in the error limit regarding the uncertainties of the respective calculations and the different methodical conditions. The CN_W ~ 3 observed in TRLFS measurements (in contrast to CN_W ~ 2 from ITFA) for the 1:2 complex can be explained by the replacement of two instead of three water molecules from the hydrate shell around the metal ion by the second Mal ligand (with total CN of 8). The lower entropy of the second Nd(III)-Mal complexation step (Table 4.3) supports this assumption, because it indicates a lower number of released water molecules compared to the first complexation step.

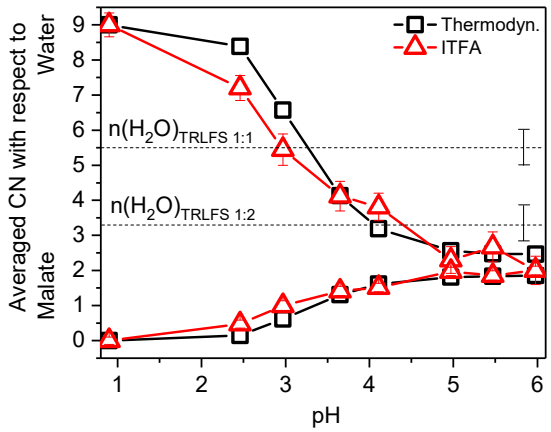

Figure 4.18: *pH*-dependent coordination number of water molecules (CN_W) and Mal ligands (CN_{MAL}) from thermodynamic calculations (ITC) and ITFA of EXAFS spectra, respectively. Error bars are the confidence intervals at 95 % estimated by using the error calculation with the methods described by Roscoe et.al.[215,216] . Dotted lines represent the number of water molecules for the 1:1 and the 1:2 Eu(III)-Mal complex from the TRLFS measurements.

4.2.5 Structural investigations at pH > 6

At *pH* values > 6 trivalent Ln(III)/An(III) show a strong tendency to hydrolysis. Usually, the positively charged hydrolysis species show strong sorption behavior on various solid phases (so also on vessels walls) and the uncharged ternary hydrolysis species possess a very low solubility. Therefore, conventional UV-Vis measurements are hardly feasible for the determination of thermodynamic data at high pH_c values due to the high required metal concentrations.[217,218] TRLFS measurements can be carried out at trace concentrations, but fluorescence quenching processes of the hydrolysis species can limiting the determination of thermodynamic data. Therefore, the focus in this chapter lies on the structural elucidation of possible mixed Am(III)-Mal-hydroxide complexes at higher pH_c values. For this purpose, a series of EXAFS spectra of the Am(III)-Mal system at pH_c values between 7 to 12 were recorded in addition to the EXAFS spectra in the acidic pH_c range (experimental details in chapter 3.4).

The VARIMAX factor loadings from the ITFA analysis of all EXAFS spectra at pH_c 1 - 12 show that at pH_c > 9 a third species becomes dominant (red line in Figure 4.19 left) in addition to the previously characterized Am(III)-aquo ion and the Am(III)-Mal complexes (chapter 4.2.4). The FTs of two samples at pH_c 11, one sample in the presence of Mal and the other in the absence of Mal are shown in Figure 4.19 (right). Both FTs show a high similarity: in addition to the O-peak at ~ 2 Å ($R + \Delta R$), a backscatter peak at ~ 4 Å ($R + \Delta R$) is visible, which is caused by the heavy backscatter Am(III). Therefore, it can be assumed that the third species is a polynuclear Am(III)-hydrolysis species and the complexation with Mal plays only a minor role under these conditions. The structural parameters of the Am(III) species at pH_c 11 (without Mal) determined by a shell fit are shown in Table 4.9

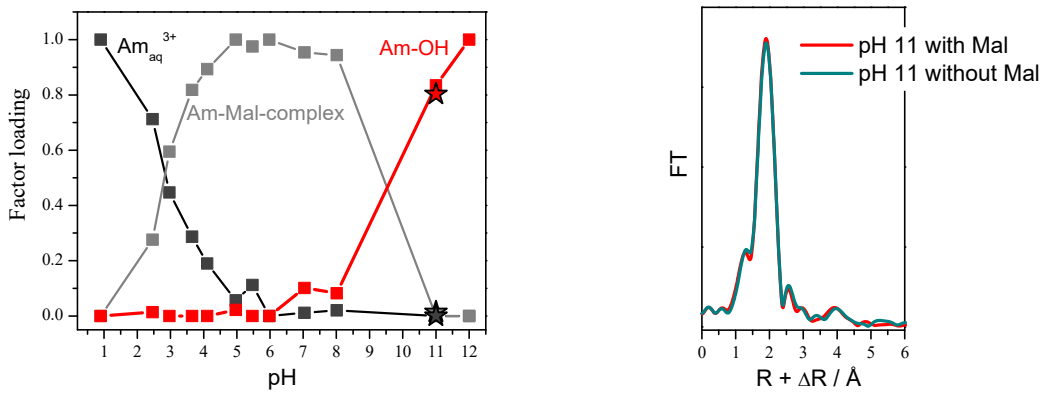

Figure 4.19: VARIMAX factor loadings of aqueous Am(III)-Mal solutions from *pH* 1 to 12 including three components (left). Fourier transformation (FT) of two samples at *pH* 11, [Am] = $1.1 \cdot 10^{-4}$ mol·L^{-1} (right).

The precipitate obtained from a Am(III)-Mal solution at pH_c = 10 was examined by using EXAFS. In contrast to the FT of the Am(III)-Mal complex at pH_c < 6, the FT of this solid shows a backscattering peak at 4 Å ($R + \Delta R$) (Figure 4.20 left, black line). This peak is attributed to the heavy backscatter Am(III), which points to a polynuclear species. The formation of polynuclear Ln(III)/U(VI)/Zn(II)-Mal species at high pH_c values is already described in the literature.[104,108,197,219,220,221] A shell fit of this spectrum was performed using the scattering paths generated from literature-known XRD structure of a mixed Nd(III)-Mal-Fumarate solid from Sushrutha et al.[108] shown in Figure 4.20 (right). The experimental spectrum was well fitted with one O, three C and one Am(III) shell(s) (Figure 4.20 left). The resulting distances and CN (Table 4.9) are in good consistency with the experimental data of the XRD structure. The mean Am(III)-C distance of 3.42 Å represents the average of the C_1, C_2 and C_3 distances according to the molecular structure in Figure 4.20 (right). Thus, a similar structure of the obtained solid in this work is assumed having a 2:4 stoichiometry, possibly $Na_2Am_2Mal_4$.

Table 4.9: Structural parameters of the aqueous Am(III) solution (without Mal) at *pH* 11 and the Am(III)-Mal solid at *pH* 10 obtained from the corresponding Shell Fits

sample/path	**CN**	***R* / Å**	**σ^2 / Å²**	**ΔE_0 / eV**
Am(III) solution, *pH* 11				
Am-O	6.3(2)	2.451(2)	0.0099(4)	10.51(7)
Am-Am	1*	3.98(1)	0.008*	10.51†
Am(III)-Mal-solid, *pH* 10				
Am-O	6.2(2)	2.437(3)	0.0108(6)	8.9(2)
Am-C	2*	2.960(9)	0.004*	8.9†
Am-C	6*	3.42(2)	0.018(2)	8.9†
Am-C_{dis}	2*	4.3(1)	0.02(4)	8.9†
Am-Am	1*	3.99(3)	0.011(3)	8.9†

CN – coordination number; *R* – interatomic distance; σ^2 – Debye-Waller factor; ΔE_0 – energy shift; † linked to the respective O-shell; * – Fixed parameter in the fit; C_{dis} – distances C-Atom. The standard deviation of the fitted parameters is given in brackets. Amplitude reduction factor $S_0^2 = 1.0$.

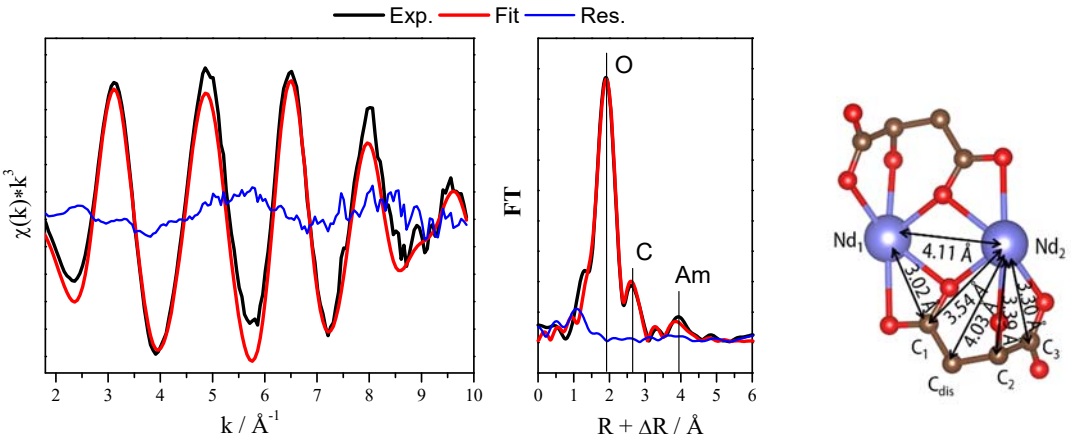

Figure 4.20: Experimental EXAFS spectrum of the Am(III)-Mal solid at *pH* 10 (left, black) with shell fit (red) and residuals (blue). Corresponding Fourier transformations (FT) (middle). Section of the XRD structure of the Nd(III)-Mal-Fumarate complex from Sushrutha et al. [108]. The values given correspond to the radial atomic spacings (right).

A comparison of the EXAFS spectra of the precipitates of Am(III)-Mal and Am(III)-Suc at high *pH* shows significant differences in the coordination of the metal ion. While Mal predominantly coordinates the Am(III) ion in a chelate structure (forming a 7-ring), the succinate Am(III) solid shows an open-chain structure.[25,182,222] The difference is mainly attributed to the stabilizing effect of the OH-group of Mal. These results show, that OH-groups have a considerable influence on the structure and stability of complexes, especially in the alkaline *pH* range. This is also reflected in the thermodynamic constants (see chapter 4.1.1).

5 Influence of Mal on Ln(III)/An(III) retention at CSH and CAH phases

5.1 Batch sorption experiments with Eu(III) and Mal at CSH phases

The sorption of tri-, tetra-, penta- and hexavalent radionuclides on CSH phases or hardened cement paste (HCP) by using batch experiments has already been widely described in the literature as a function of the solid/liquid ratio, the C/S ratio, the metal addition (direct/indirect) or concentration, the medium (water or ACW) and the reaction or contact time.[15,16,62]

The batch sorption experiments in this project were primarily aimed at quantifying the influence of the cement additives (using Mal as an example) on the Ln(III)/An(III) retention. These investigations are complementary to the structural investigations. The metal concentrations were chosen so that adequate results were obtained with respect to the structural sensitive method (Am(III) for EXAFS, Cm(III) for TRLFS, Eu(III) for TGA/NMR). The binary systems Eu(III)/CSH and Mal/CSH as well as the ternary system Eu(III)/Mal/CSH were studied in dependency on the C/S ratio and the used Mal and metal ion concentrations.

It is well known from the literature and from the work in this GRaZ joint project that the trivalent Ln/An show an almost quantitative sorption on the cement phases, which is reflected in log K_d values ~ 5 (5-6 in ACW, see Table 2.1). The determined log K_d values between ~ 4 and ~ 5 are independent of C/S ratio and the presence of Mal (Figure 5.1, Table 7.9). It should be highlighted that the sorption of Eu(III) is almost independent of the used Mal concentration (Figure 5.1, top right). In some references it is discussed that small organic molecules can increase the solubility of Ln/An by forming soluble ternary mixed complexes. [80,83,85,86] This results in an increase of the metal concentration in the supernatant solution and the log K_d value decreases. For the sorption of Eu(III) on CSH phases, however, an increase of the solubility caused by Mal was not observed. The complexation strength of Mal is not high enough to influence the Ln(III)/An(III)-sorption at CSH phases quantitatively.

The determined log K_d values, especially for Cm(III) (due to the low Cm(III) concentration) can be slightly underdetermined in comparison with the literature values. The reason for this is that possible colloidal particles of the metal-doped CSH phases were not completely removed in the supernatant solution, because the use of an ultracentrifugation was not possible for the phase separation.

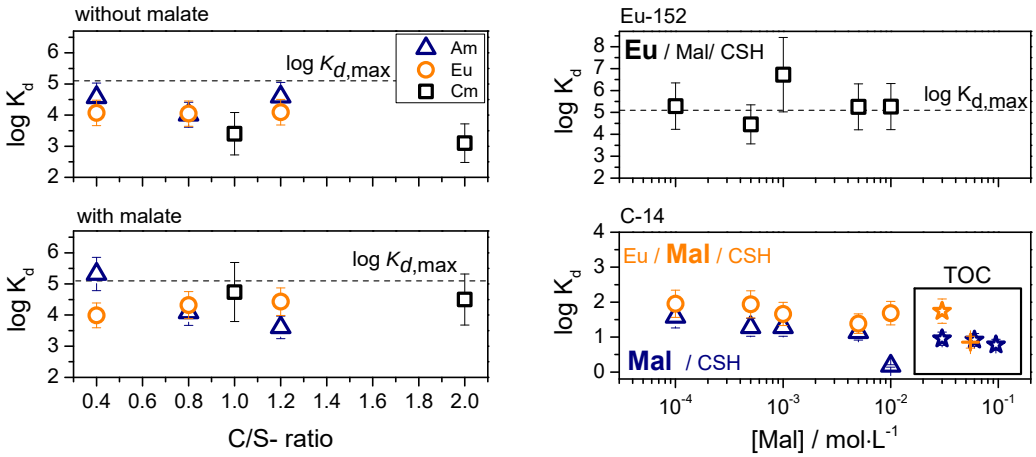

Figure 5.1: Log K_d-values as function of C/S ratio for [Cm] = 3·10^{-6} mol·L^{-1}; [Am] = 1·10^{-4} mol·L^{-1}; [Eu] = 2·10^{-4} mol·L^{-1} (top left). Log K_d-values as function of C/S ratio with Mal for [Cm] = 3·10^{-6} mol·L^{-1} and [Mal] = 1.5·10^{-2} mol·L^{-1}; [Am] = 1·10^{-4} mol·L^{-1} and [Mal] = 2·10^{-3} mol·L^{-1}; [Eu] = 2·10^{-4} mol·L^{-1} and [Mal] = 2·10^{-4} mol·L^{-1} (bottom left). Log K_d-values of ^{152}Eu (top right) or ^{14}C- labelled Mal (bottom right) as function of the Mal concentration at C/S 0.8 with [Eu] = 1·10^{-4} mol·L^{-1}. The used radioactive element/molecule is marked in bold. TOC (*Total Organic Carbon*): [Eu] = 2.7·10^{-2} mol·L^{-1} (star); [Eu] = 5·10^{-3} mol·L^{-1} (cross) (right).

Batch experiments with C-14 labeled Mal show that Mal, independent of its concentration, sorbs to a significantly lower extent at CSH phases than Eu(III) (Figure 5.1, bottom right, blue dots). The log K_d values are three orders of magnitude below those of Eu(III). A sorption to the silanol groups of the CSH phases occurs only to a limited extent, because Mal is negatively charged and structurally larger than Eu(III). The presence of Eu(III) has no or only a very small influence on the Mal sorption on the CSH phases (Figure 5.1, bottom right, orange dots). With increasing C/S ratio an increasing of the Mal sorption was observed (independently of the presence of Eu(III)). This indicates a Ca^{2+} mediated uptake of Mal in the CSH interlayer or on the CSH surface.

For the CAH phase katoite similar results were obtained: almost quantitative Eu(III) sorption, which is independent of the Mal concentration and a much weaker Mal sorption (see Table 7.10 and Figure 7.3 in the appendix). The katoite structure remained stable throughout the whole experiment (verified with PXRD measurements).

5.2 PXRD studies and thermal analysis

One focus of our work was to determine the An(III)/Ln(III) ligand speciation and its structural incorporation into the CSH/CAH phases. At present, there are only few substantiated studies on this field in the literature due to the amorphous character of the phases and the resulting difficulty in identifying An(III)/Ln(III) species in such phases. Therefore, one important step was the characterization of the synthesized cement phases by thermogravimetric analysis (TGA), differential scanning calorimetry (DSC) and powder X-ray diffraction (PXRD).

Due to the amorphous CSH structure, the PXRD diffraction patterns of the pure CSH phases show broad reflexes (peaks) with maxima at (7.8),16.4, 29.3, 32.1, 49.8 and 55.2 °2θ (Figure 5.2). The peak positions correspond very well with literature values of 14 Å-tobermorite (Plombierite PDF 00-029-0331). At high C/S ratios, the formation of portlandite ($Ca(OH)_2$, P in Figure 5.2) becomes more and more visible by the characteristic signals in the diffraction pattern. The PXRD diffraction patterns of the CSH phases doped with Eu(III)- or Eu(III)-Mal show hardly any changes compared to the pure CSH phase. The tobermorite structure remained unaffected at the used metal concentrations.

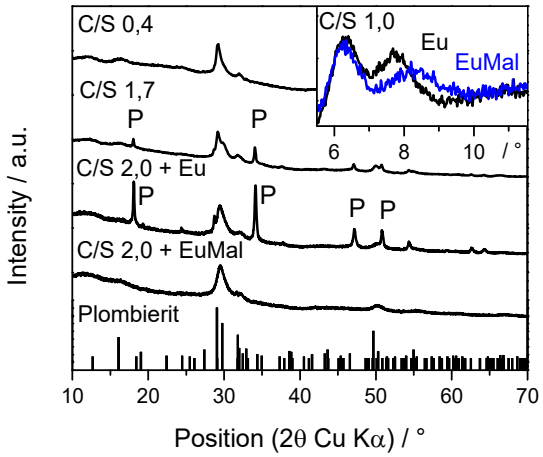

Figure 5.2: PXRD-diffraction pattern of the CSH phases with C/S 0.4 and 1.7 without additives, with C/S 1.0 (insert) and C/S 2.0 with [Eu] = $2 \cdot 10^{-4}$ mol·L^{-1} or [Eu] = $2 \cdot 10^{-4}$ mol·L^{-1} and [Mal] = $4 \cdot 10^{-3}$ mol·L^{-1}. Plombierite is shown as a reference. Peak in diffraction pattern at 6.3 °2θ (insert) is attributed to the sample holder.

The peak at ~ 8 °2θ represents the basal interspace of the CSH phases. This peak is shifted in the presence of Eu(III) and Mal by ~ 0.5 °2θ to higher angles compared to the CSH phase doped only with Eu(III) (see insertion in Figure 5.2). This shift can be caused by a reduction in the basal interspace distance and/or by a change in the crystallinity of the phases[161,162,223,224] At high C/S 2.0 the precipitation of portlandite is suppressed by Mal (Figure 5.2, C/S ratio 2.0) due to the complexation of Mal with Ca. This lowers the C/S ratio. [21,161,162]

Figure 5.3 shows the first derivations of the thermogravimetric signal (DTG) and the DSC curves of different CSH phases (with higher additive concentration than in PXRD measurements). It is known from the literature that CSH phases release water within a large temperature range (50 - 600 °C), which originates from the interlayer and from dehydroxylation processes (release of OH groups).[225] The release of water can be seen in the DTG curves and is connected with an endothermic heat effect (positive signal in the DSC curve). The exothermic peak at ~ 850 °C in the DSC signal can be attributed to the phase transformation from CSH to wollastonite (W, $CaSiO_3$).[226,227] Temperature of this phase transition depends on the C/S ratio. At high C/S ratios, a mass decrease due to the decomposition of portlandite (P) to water and CaO at ~ 440°C can also be seen in the DTG curve, which is simultaneously observed as an endothermic heat effect in the DSC curve (Figure 5.3 left).

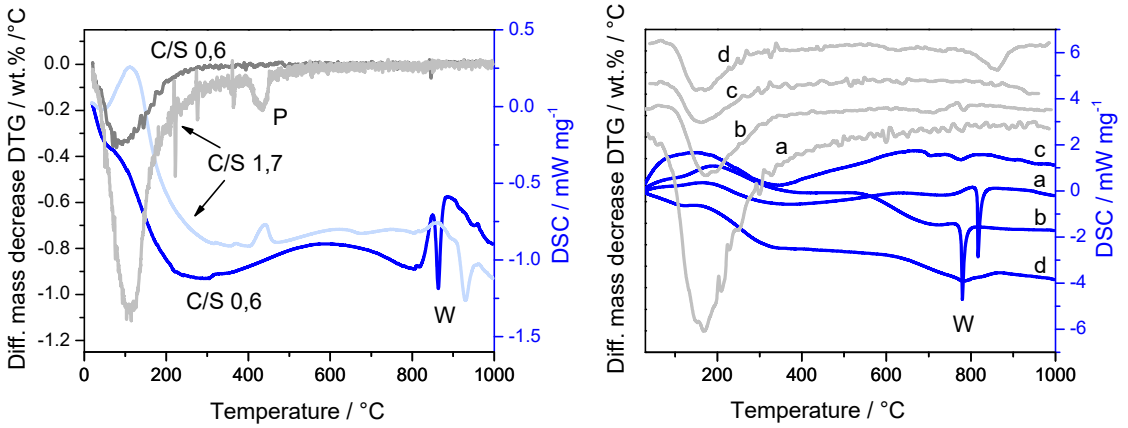

Figure 5.3: First derivation of the mass decrease (DTG) and DSC-signal of CSH-phases with C/S 0.6 und C/S 1.7 without additives (left) and of doped CSH phases at C/S 1.0. (a) – pure, (b) – with [Mal]= $6.0 \cdot 10^{-2}$ mol·L^{-1}, (c) - with [Eu] = $5.5 \cdot 10^{-2}$ mol·L^{-1}, (d) - with [Eu] = $2.7 \cdot 10^{-2}$ mol·L^{-1}and [Mal] = $3.0 \cdot 10^{-2}$ mol·L^{-1} (right).

The DTG signals of the doped CSH phases show a reduced mass loss (Figure 5.3 right). This is due to the hydration retarding effect of Mal and a possible cross-linking effect of Eu(III). The addition of Mal decreases the phase transition temperature from ~ 817 °C to ~ 780 °C compared to the pure CSH phase. The Eu(III) and Eu(III)-Mal-doped CSH phases (c and d in Figure 5.3 at [Eu] > $2.0 \cdot 10^{-2}$ mol·L^{-1}), however, do not show any phase transformations. The PXRD diffraction patterns of these two phases (Figure 5.2) show the typical reflexes of tobermorite. Thus, no secondary (mixed) phases are present. A possible carbonate contamination can be excluded: Carbonate decompose the CSH phases to silicic acid and amorphous $CaCO_3$ (calcite)[228,229] with a DTG signal at ~ 650 °C.[225] This indicates that the additives suppress the phase transformation. Small peaks in the DSC curves at 700 - 800 °C could indicate a low content of an amorphous phase such as $Eu(OH)_3$. Since even at a lower Eu(III) concentration (at [Eu(III)] < $2.0 \cdot 10^{-2}$ mol·L^{-1} and in the presence of Mal) a phase transformation peak is observed in the DSC signal (not shown here), the influence on the phase transformation is mainly due to the presence of Eu(III).

CAH phases

The formation of katoite could be clearly verified by the characteristic reflection patterns. No phase changes were observed when varying the S/L ratio or the crystal system of the precursor (Figure 7.4, left) Katoite degrades in two steps with increasing temperature as shown by TGA/DSC (Figure 7.4, right).The first step occurs at 300 °C and the second at 450 °C. In both cases a decrease in mass due to water loss after the following reactions can be observed.

$$7\ Ca_3Al_2(OH)_{12} \longrightarrow Ca_{12}Al_{14}O_{33} + 9\ Ca(OH)_2 + 33\ H_2O$$
$$2\ Al(OH)_3 \longrightarrow Al_2O_3 + 3\ H_2O \qquad 5.1$$

$$Ca(OH)_2 \longrightarrow CaO + H_2O \qquad 5.2$$

The addition of NaCl has a significant influence on the katoite structure. With increasing Cl concentration, a gradual transformation of the katoite into a LDH phase can be observed, whereby mainly the

$Ca_4Al_2(OH)_{12}Cl_2$-LDH is formed (confirmed also with IR spectroscopy, here not shown). Even at low Cl^- concentration new reflexes can be observed in the PXRD pattern at 10 to 25 °2θ and other reflexes vanish with increasing [Cl^-] (katoite marked with a star in Figure 5.4, left). The areas of 11 – 13 °2θ and 22 – 25 °2θ are very sensitive for the changes in the distance between layers of such LDHs (inserts in Figure 5.4). The observed shift to higher angles is caused by a decrease in the interlayer distance. Peak splitting occurs as well, which means that two different distances occur in the same structure. The C/A ratio changes from 1.5 (katoite) to 2 (LDH) (confirmed by ICP-MS measurements) when increasing Cl^- concentrations.

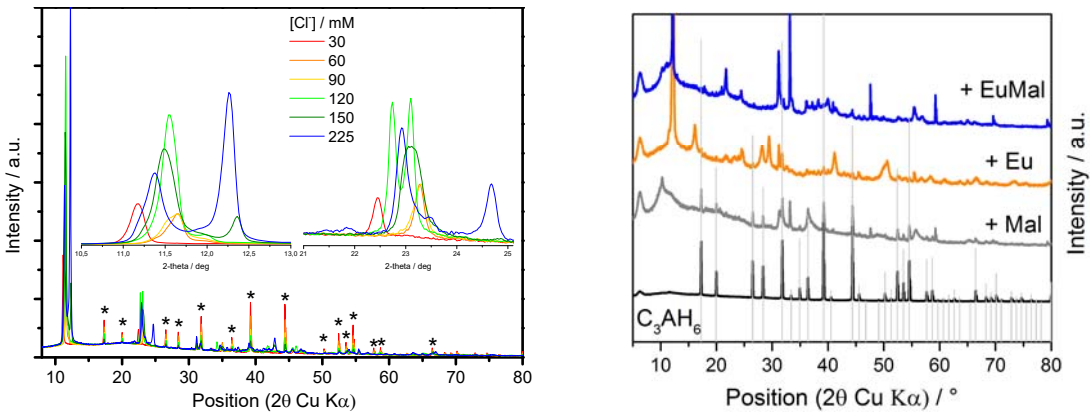

Figure 5.4: PXRD-diffraction pattern of the CAH phase katoite as function of [Cl^-], inserts zoomed part of the angle ranges 11 – 13 °2θ and 22 – 25 °2θ (left), PXRD-diffraction pattern of the CAH phase katoite in presence of [Eu^{3+}] = 50 mM and [Mal] = 50 mM (right)

The addition of Eu(III) and Mal inhibits the formation of the katoite, the new formed (LDH) phases are more amorphous. Changes in the PXRD diffraction patterns can be observed, namely peaks shifts and new peaks occur which could not be assigned to any known phase so far (Figure 5.4, right). Especially the strong changes in the regions of 11 – 13 °2θ and 22 – 25 °2θ in the Eu(III)-doped CAH phases are indications that Eu(III) (as $Eu(OH)_3$, $Eu(OH)_4^-$) could be bound in the intermediate layer of the formed LDH phases.

5.3 NMR spectroscopy

Examples of the ^{29}Si-NMR spectra of pure and doped CSH phases are shown in Figure 5.5. All chemical shifts and fractions obtained by spectral deconvolution are summarized in Table 5.1. ^{29}Si-NMR spectra generally show broad spectral signals due to second order quadrupole interactions or anisotropic interactions (even with Magic Angle Spinning NMR measurements). In the ^{29}Si-NMR spectra the silicate end group tetrahedra Q^1 and the bridging and paired tetrahedra Q^2 can be distinguished (see chapter 2.1.1 and Figure 2.2 for an explanation of the Q^n classification). The chemical shifts and relative fractions of Q^1 and Q^2 of the pure CSH phase correspond very well with literature values for a C/S ratio of one. [38,230,231,233]

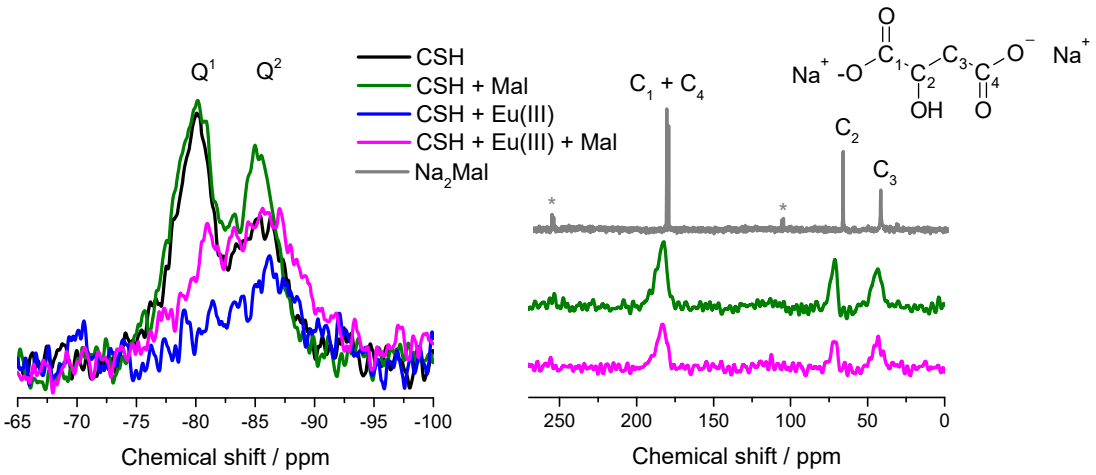

Figure 5.5: ^{29}Si (left) and ^{13}C NMR spectra (right) of the pure and doped CSH phases with C/S 1.0 and disodium malate. Concentrations see Table 5.1.

Mal has no influence on the ^{29}Si-NMR spectra, neither on Q^1 and Q^2 fractions nor on the chemical shifts, only the Q^2 signal is narrower compared to the pure CSH phase. In the range of -86 to -88 ppm, the signals of the Q^{2u} tetrahedra are found. These tetrahedra are linked by hydrogen bonds in the CSH interlayer.[161,162,224,232] A change in this signal could result from the binding of Mal within the CSH interlayers. It should be mentioned here that an outer sphere sorption of Mal not only on the CSH surface but also within the CSH interlayer is quite possible.

Table 5.1: Chemical shift and relative fractions (in %) of the Si-Q^1 and Si-Q^2 tetrahedra in the pure and doped CSH phases with C/S 1.0 determined in the ^{29}Si NMR spectra. I_M = 0.1 mol·L^{-1} NaOH.

Sample	**[additive] / mol·L^{-1}**	**Q^1**		**Q^2**		**MCL [&]**
		ppm[#]	**%[$]**	**ppm[#]**	**%[$]**	
Pure CSH phase	-	-79.9	64	-85.6	36	3
Pure CSH phase, C/S 1.2 [233]	-	-79.5	65	-85.3	35.1	3
CSH + Mal	6·10^{-2} (Mal)	-79.9	62	-85.4	38	3
CSH + Eu	6·10^{-2} (Eu(III))	-81.6	18	-86.5	82	11
CSH + EuMal	3·10^{-2} (Mal) and 3·10^{-2} (Eu(III))	-80.1	27	-85.3	73	7
CSH + EuMal* (not shown)	5.5·10^{-2} (Mal) and 5·10^{-3} (Eu(III))	-80.1	46	-85.4	54	4

[#] – Uncertainty of chemical shift ppm ± 0.5; [$] – Uncertainty of fractions ± 10 %; [&] – Uncertainty of MCl (main chain length) ± 2

Due the paramagnetic influence of Eu(III) the ^{29}Si signal is decreased strongly relative to the pure CSH phase in the ^{29}Si-NMR spectra of the Eu(III) and Eu(III)-Mal-doped CSH phases. The signal-to-noise ratio worsens significantly, which makes an accurate peak identification very difficult. The quenching through Eu(III) is more efficiently transferred to the Q^1 tetrahedra. It can be attributed to different effects, which cannot be resolved: a) the coordination of Eu(III) in the defect sites of the bridging Q^2 tetrahedra so that Eu(III) actually coordinates to Q^1 , b) the incorporation of Eu(III) in the CaO layer next to defect sites so that Eu(III) is closer to Q^1than to Q^2 or c) a higher water accessibility of Q^1 by which Eu(III) quenching can be transferred more efficiently via protons and therefore increasing relaxation. The increase of the main chain length (MCL, see Equation 3.18 in chapter 3.7.3) represents an apparent polymerization actually caused by the paramagnetic quenching (Table 5.1).

In case of the Eu(III) doped CAH phases (katoite) the ^{27}Al-NMR spectra show no significant changes compared to that of pure katoite, Al is 6-fold (octahedral) coordinated like in the pure katoite. If Mal is present a 4-fold (tetrahedral) Al-coordination in the range of 60-80 ppm can be observed next to the 6-fold (octahedral) Al-coordination in the range of 3-15 ppm of the chemical shift (Figure 7.5). Mal acts as a retarder and therefore probably unreacted precursor is still present in the samples. In the precursor Al is rather 4-fold coordinated.

^{13}C-NMR spectra were recorded to identify the binding mode of Mal in the CSH phases. The chemical shifts of ^{13}C in the Mal- and Eu(III)-Mal-doped CSH phases are both very similar to those of the disodium Mal reference sample (Figure 5.5). Only a signal broadening can be observed, which is indicating the presence of several Mal species with slightly different chemical environments in the amorphous CSH phases. The small low field shift of 2 ppm of the signal of the C_2 atom of Mal in the CSH samples is due the coordination of the OH by Ca^{2+} (instead of Na^+). The similarity of all measured ^{13}C-NMR spectra suggests that Mal is present in a similar binding mode in the CSH samples, namely as an outer sphere sorption complex mediated by Ca, even in the presence of Eu(III). An Eu(III) Mal complex is unlikely. Rather, the results indicate a separate binding of Eu(III) and Mal in the CSH phases, even if they were added simultaneously as a complex to the CSH suspension.

5.4 Time-resolved laser-induced fluorescence spectroscopy

Excitation, fluorescence emission spectra and fluorescence lifetimes were used to characterize possible sorption or complex species. Furthermore, for Eu(III) and Cm(III) the site-selective TRLFS was used to identify individual species.

The Am(III) coordination in the CSH phases is indicated by a clear redshift of 5 - 8 nm of the Am(III) emission of the Am(III)-doped CSH phases compared to the pure Am(III)-aquo ion (691 nm). In presence of Mal, a significant increase in fluorescence intensity is observed, no additional shifts or splitting of the Am(III) emission spectra appear (example in Figure 5.6). This indicates the formation of a new Am(III) species, associated with a decrease in quenching, as observed in other Am(III) ligand systems.[110,234,235] The Am(III) decay curves (Figure 5.6 insert) can be fitted mono-exponentially in all CSH samples with a fluorescence lifetime of ~ 200 ns independent of the C/S ratio (Table 7.11). Mal has no significant influence on the fluorescence lifetime, only at very low C/S ratios (C/S ~ 0.4) is it slightly increased. Here the simultaneous Ca-Mal complexation (decalcification by Mal) causes a

stronger change of the Am(III) surrounding CSH structure than at higher C/S ratios, which then results in a variation of the surrounding quenching water molecules.

The determined fluorescence lifetime is significantly prolonged compared to that of the Am(III) aquo ion with $\tau = 26 \pm 2$ ns, the Am(III)-Mal-(hydroxide) complex with $\tau = 58 \pm 5$ ns (at pH 7.8)[139] or other literature-known aqueous Am(III)-ligand complexes.[110,234,235] On the other hand, the lifetime is much shorter compared to solid solutions with Am(III) like the more highly ordered Am(III) calcite system (414 ± 16 ns and 1875 ± 45 ns at T = 18 K).[132] The results show that Am(III) is only weakly hydrated/hydroxylated within the CSH phases, indicating that Am(III) is either sorbed to or incorporated into the CSH structure. Different Am(III) species cannot be distinguished with these measurements, because in this system either the exchange reaction between the water molecules of the first coordination sphere and the ligand molecules is faster than the luminescence decay rate of the excited Am(III) species, so that in total only mono-exponential decay curves result, or the different very short fluorescence lifetimes cannot be resolved by the used laser system.

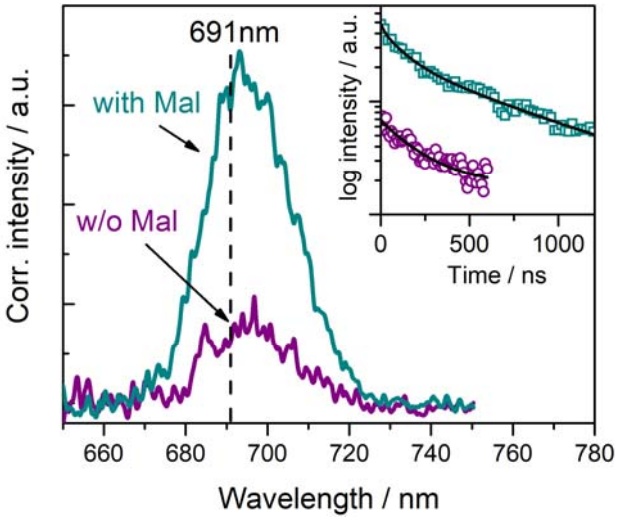

Figure 5.6: Emission spectra and monoexponentially fitted decay curve (inset) of Am(III)- and Am(III)-Mal-doped CSH phases (C/S 0.4) with λ_{exc} = 506 nm and [Am] = $1.1 \cdot 10^{-4}$ mol·L^{-1}.

A more detailed insight into the Ln(III)/An(III)-Mal species identification in the CSH phases is given by the site-selective TRLFS with Cm(III) and Eu(III).[25,139] Our investigations with Cm(III) are complementary to the studies from Wolter et. al [249].

Like the excitation spectra for the pure Cm(III) doped CHS phases in reference[249], the excitation spectra of the Cm(III)-Mal doped CSH phases also show very broad peaks at ~ 605 and ~620 nm (Figure 5.7). When exciting around 620 nm multiple narrow emission lines occur. This is typically denoted as the luminescence line-narrowing effect; it was previously observed in solid solutions and different minerals and is also expected for amorphous systems without long-range order. It can be attributed to the existence of several Cm(III) species showing slightly different chemical environments.[236,249] The band at ~ 605 nm can be assigned to a hot band corresponding to the transition from the A_2 sublevel of the $^6D_{7/2}$ transition to the $^8S_{7/2}$ ground state. The excitation in this hot band is apparently followed by an energy transfer between the several Cm(III) species, which results in only one broad emission peak.

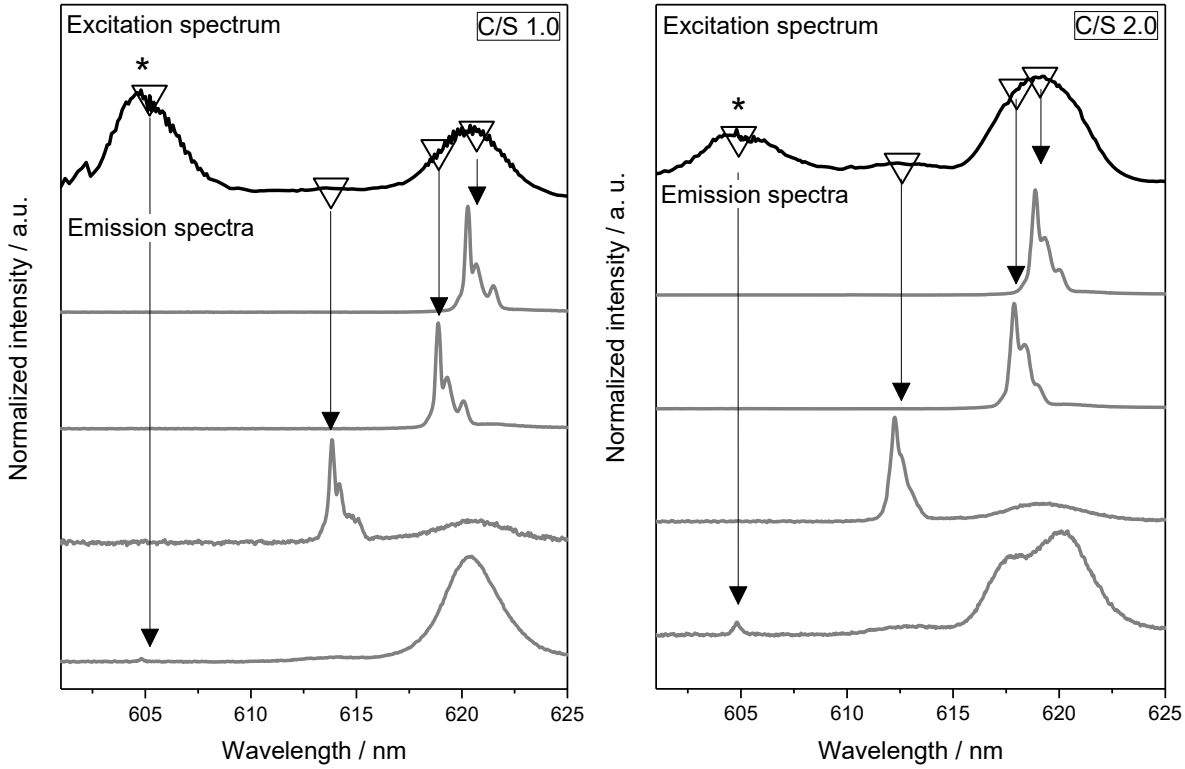

Figure 5.7: Excitation and emission spectra of Cm(III)-Mal-doped CSH phases at C/S 1.0 (left) and at C/S 2.0 (right). The hot band transition is marked with asterisks.

Time-resolved measurements of the Cm(III)-Mal-doped CSH samples yielded two main species like the analog pure Cm(III)-doped CSH samples from Wolter et. al. [249] The average lifetimes are summarized in Table 7.11. The first lifetime τ_1 corresponds well with literature values and represents a sorbed Cm(III) species with 2-3 H_2O/OH^- molecules. The second lifetime τ_2 is slightly shorter than the corresponding one in the system without Mal. This is rather caused by a symmetry change of the ligand field of the Cm(III) ion and/or a more efficient energy transfer from Cm(III) to the OH oscillations by shorter binding distances than by the unlikely presence of a ternary Cm(III)-OH-Mal complex in the CSH phase. When excited at ~ 620 nm, the emission spectra show a threefold splitting with a splitting of 29-31 cm^{-1} of the Cm(III) ground state which is typical for incorporated Cm(III) species. These highly resolved emission peaks indicate a high degree of order in the environment of Cm(III) in presence of Mal in contrast to the studies of the analogue samples[249] without Mal. Furthermore, another but unsymmetrical species (4-fold splitting) with an emission maxima ~ 613 nm is only observed in the presence of Mal and is probably absorbed in the interlayer of the CSH phases (see [25,139] for more detailed information).

Similar species groups as identified from the Cm(III)-TRLFS were also observed in TRLFS studies with Eu(III), although these TRLFS measurements were performed at significantly higher metal concentrations and in a different medium (for Eu(III) in water, for Cm(III) in ACW). The fluorescence emission spectra of Eu(III)-CSH solids show a complete splitting of all levels into (2J+1) lines, which correlates with a low symmetry of the ligand field of Eu(III), e.g. a C_S, C_1, C_{2h} or S_2-symmetry[237] (Figure 5.8 left). The observation of the $^5D_0$-$^7F_0$-transition is a further indication of a low symmetry of Eu(III) in the CSH phases compared to the Eu(III)-aquo ion (in Figure 5.8, left). The observed broad Eu(III)

emission and excitation peaks are typical for the presence of a broad distribution of species, all in a similarly disordered chemical environment (Figure 5.8, right). Since in the presence of Mal the splitting patterns in the Eu(III) emission spectra do not change, it can be concluded that the disordered chemical environment of Eu(III) is not affected. This is in obvious contrast to the conclusions of the Cm(III)-TRFLS studies, where a higher order of Cm species was found in the presence of Mal. One reason for this is (besides the much lower used Cm(III) concentration), that the Cm(III) fluorescence has a much higher sensitivity to changes in the chemical environment, which allows a more accurate structural interpretation of the species (especially when these are present in small fractions).

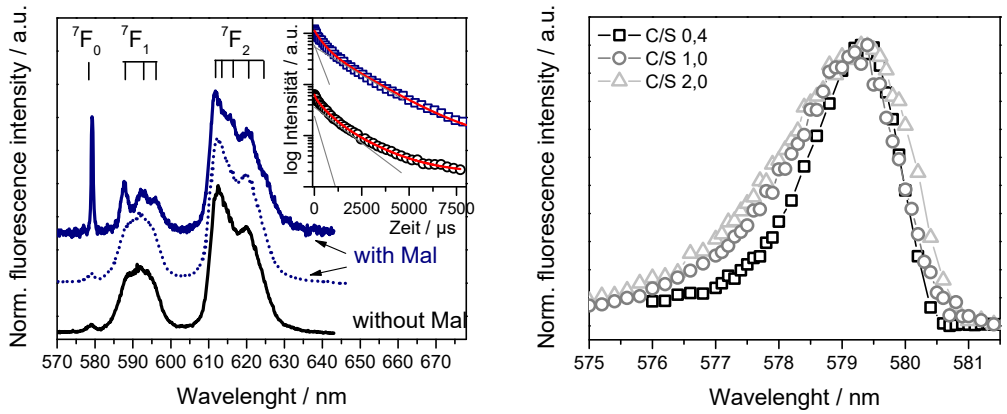

Figure 5.8: Fluorescence emission spectra and exponentially fitted decay curves (left) of Eu(III) (black) and Eu(III) Mal-doped CSH solid at RT (λ_{exc} = 394 nm, blue, dotted) and T < 20 K (λ_{exc} = 579.5 nm, blue, with laser peak) at C/S 0.4 (left). Excitation spectra ($^7F_2$ emission) of Eu(III)-doped CSH-solids at T < 20 K at different C/S ratios, [Eu] = $2 \cdot 10^{-4}$ mol·L^{-1} (right).

Mal has an influence on the fluorescence intensity (increases significantly) and the lifetimes (see Table 7.11 for the lifetimes of the species), which indicates a change in the chemical environment of Eu(III) in the CSH phases in the presence of Mal. At C/S 0.4 the fluorescence lifetime of Eu(III) increases slightly in the presence of Mal. However, this change has only a slight effect on the number of coordinating water/OH molecules surrounding Eu(III) (within the error range). An increase in fluorescence lifetimes could indicate the formation of a Ca-Eu(III)-Mal-hydroxide complex. Since fewer Ca ions are present in relation to higher C/S ratios, Mal may have a non-negligible influence on the species distribution of Eu(III) by the complex formation with Ca. At C/S 1.0, the Eu(III) fluorescence lifetimes of the two main species decrease substantially in the presence of Mal, indicating a change in the chemical environment of Eu(III) in the CSH phases. This lifetime decreasing is consistent with the Cm(III)-Mal-CSH system. At C/S 2.0, the Eu(III) fluorescence lifetimes increase significantly in the presence of Mal compared to the analogue CSH sample without Mal (see Table 7.11). This is because to the absence of portlandite in the malate-containing phases. (see PXRD measurements).
Preliminary site-selective TRLFS measurements of Eu(III) doped CAH phases (katoite-LDH phases) show (Figure 7.6, left) two broad excitation peaks, indicating at least 2 species groups. The excitation at different wavelengths in the $^7F_0$-transition results in emission spectra with a 2-to 3-fold splitting of the $^7F_1$-band and a 3-fold to 5-fold splitting in the $^7F_2$-band (Figure 7.6, right). This suggests that Eu(III) species with ligand fields of higher symmetry as well as very low symmetry[237] are present in the CAH phases. A fluorescence lifetime of ~ 200-250 µs was determined for all species suggesting sorbed Eu(III)

species. This lifetime is much smaller than in similar Eu(III)-solid/mineral systems. Probably quenching processes (e.g. due to OH^-) play an important role in the Eu(III)-CAH system. Thus, no classification of the different species into sorbed, incorporated or polynuclear species can be derived. Presently, further TRLFS investigation in the Eu(III)-CAH system are in progress.

5.5 EXAFS spectroscopy

The EXAFS spectroscopy in combination with the iterative transform factor analysis (ITFA[212]) is an important tool to characterize structures of species in solids or complexes, even if the individual species are only present in spectral mixtures.[186,213]

Using ITFA three components, in the following referred to as species, could be determined from the EXAFS spectra. All experimental EXAFS spectra can be reproduced well with the extracted three species. The fractions (normalized varimax factor loadings) are shown in Figure 5.9. Species 1 is only present in the samples with a C/S ratio of 0.4 independent of the presence of Mal, while species 2 becomes dominant in the samples with a C/S ratio ≥ 0.8 if no Mal is present. In presence of Mal in the samples at higher C/S ratios two species, species 2 and further species 3 are present, species 3 becomes dominant at high C/S ratios and high Mal concentrations.

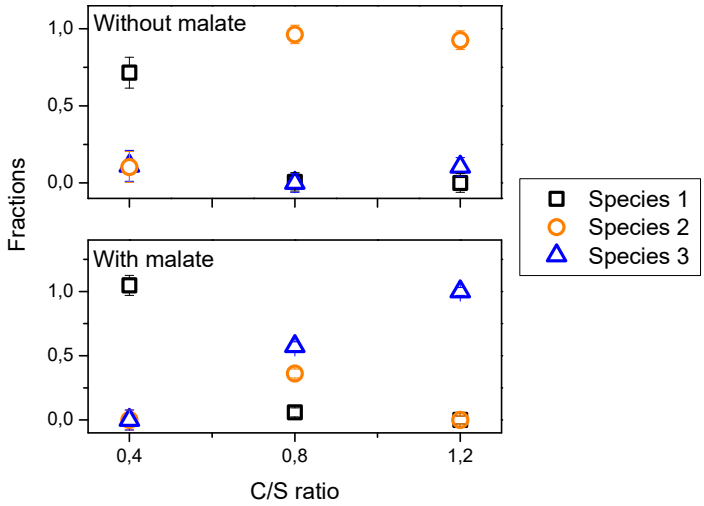

Figure 5.9: Fractions of the three species of Am(III)-C-S-H (above, samples 1-3 in Table 3.2) and of Am(III)-Mal-C-S-H (below, samples 4-6 in in Table 3.2) EXAFS spectra in dependence of C/S ratio determined by ITFA.

The concentrations or percentages of the species are not known, so that no single component spectra can be extracted. Thus, only those EXAFS spectra will be considered for the in the following shell fit where the respective species has its maximum fraction. These shell fits were performed with a FEFF file generated with the model structure of tobermorite[238] (and britholite). The experimental EXAFS spectra, their Fourier Transformations (FT), the corresponding shell fits and the resulting structural parameters of the three species are shown in Figure 5.10 and listed in Table 5.2, respectively.

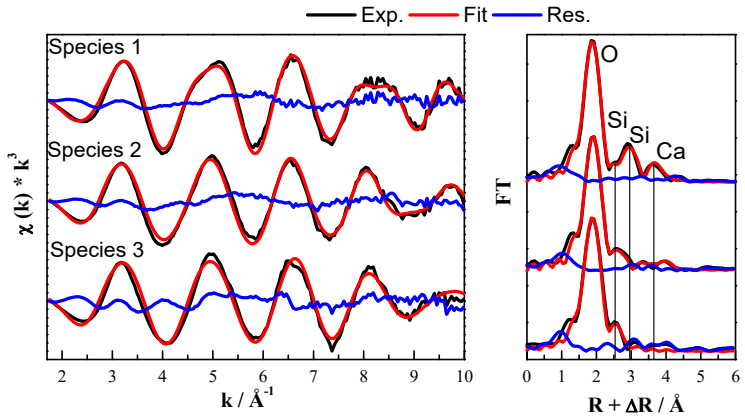

Figure 5.10: EXAFS spectra (black) of each species and respective FT (right) with shell fit (red) and residual (blue).

Species 1 and 2 both can be well described by one O shell, two Si shells and one Ca shell. The number of shells was used according to the literature[70,71], whereby a smaller number of shells significantly worsened the fit. The Am(III)-O distances R_{Am-O} of both species with 2.41 - 2.44 Å correspond well with the distances in the Eu(III)-CSH and the Nd(III)-CSH systems[70,71]. The determined coordination number (CN) for oxygen of 6 - 7 is equal to the CN_O of Ca in the CaO sheets of non-doped CSH phase with similar C/S ratio. This indicates that Am(III) is incorporated in the CaO framework of the CSH phases by substitution of Ca. Furthermore, one Si atom is located in the nearer surroundings of Am(III) at a distance of 3.16 Å and 1 - 3 Si atoms have at a distance of 3.66 - 3.87 Å. However, these two Si shells seem to be very variable with respect to their CN and therefore usually show large errors.

Higher CN_{Si} at low C/S correspond to the presence of bridging Si tetrahedra in the CSH phases which are eliminated at C/S > 0.7. The sorption of the metal on amorphous SiO_2 at C/S 0.4 can be excluded, as this would result in longer metal-Si distances (R_{Nd-Si} = 3.85(6)[71]. Additionally, 1 - 2 Ca atoms can be observed at 4.2 - 4.5 Å for species 1 and 2. The CN_{Ca} determined here points towards the presence of on the CSH surface adsorbed Am(III) rather than incorporated Am(III) which would results in CN_{Ca} of 4-5[238,239]. The Am(III)-Ca distances determined here are significantly longer than R(Eu/Nd-Ca) distances in the literature[70,71]. Longer metal-Ca bond distances may be due to a higher degree of disorder of the CSH phase which can be caused by the increasing incorporation of Am(III) into the CSH phases. The degree of disorder therefore depends on the used preparation method, the metal concentration and the metal/CSH contact or reaction time.

The backscattering peak at ~ 4 Å (R + ΔR) could also be attributed to a possible precipitation of Am(III) in the CSH phases. The back transformation of the EXAFS signal (at C/S ≥ 0.8) confirms the existence of the heavy backscatterer Am(III) at this distance. But significant amounts of polynuclear Am(III)-hydroxide species or of an Am(III)-Mal solid can be excluded in the CSH samples (for more details see[25,139]). Nevertheless, Am(III) could be co-precipitating with Mal and/or Ca within the CSH phases, which could result in different structural parameters of the precipitate. A co-precipitation of Ca in a possible Am(III) precipitate would explain the small CN_{Ca} and the slight decrease of CN_{Ca} at higher C/S ratios. Since the peaks around ~ 4 Å (R + ΔR) in the CSH samples have a very small amplitude (although Am(III) is a heavy backscatterer), only a small fraction of a polynuclear Am(III) precipitate is formed. Furthermore, the CN_O would be much higher for such a precipitate, between 6.8 and 9.6, which was determined e. g. for Eu(III) precipitate in CSH phases.[70]

The EXAFS spectrum and the FT of species 2 differ significantly from these of species 1. While the backscattering peaks in the FT of species 1 are clearly pronounced, all backscattering peaks of species 2 (except the O shell) show a significantly smaller amplitude. Therefore, it is assumed that an Am(III) inner-sphere sorbed surface complex (in the CSH intermediate layer) is mainly characterized by species 2 in contrast to an incorporated Am(III) species, which is mainly reflected by species 1.

As well as species 2, species 3 also shows very small backscattering contributions (exception O atom) compared to species 1. The spectrum of species 3 (C/S 0.8 and 1.2) could not be satisfactorily fitted with four shells. Only the structural parameters of one O and one Si shell could be extracted. The Am(III)-O- and the Am(III)-Si distance in species 3 are significantly shortened compared to the respective binding distances in the samples without Mal. A back transformation in the range between 2.9 - 4.5 Å (R + ΔR) indicates the presence of light backscattering atoms. Due to the similarity of the FTs of species 2 and 3, the dominant existence of a sorbed species can be concluded. However, the Am(III) surrounding structure in the Mal-doped CSH phases seems to have changed significantly from species 2 to species 3.

As already mentioned hydroxycarboxylates like Mal are known to cause a decalcification within CSH phases by forming outer-sphere sorption complexes with Ca. This structural change in presence of Mal especially influences the Am(III)-Ca bond distances so that tobermorite/britholite does not provide a sufficiently good structural fitting model for the EXAFS data anymore. Therefore, to identify the pure component EXAFS spectra for Am(III) in (Mal-doped) CSH phases from the experimental spectral mixture, a combination of quantum mechanical calculations and various numerical approaches is useful, for more information see[139].

Table 5.2: Structural parameters from the Shell Fit of the EXAFS spectra in which the respective species have their maximum fractions compared to literature values.

sample	Path	CN	R / Å	σ^2 / Å^2	ΔE_0 / eV
Species 1: C/S 0.4 with Mal	Am-O	6.3(2)	2.412(2)	0.0085(3)	4.1(2)
	Am-Si_1	1.1(1)	3.161(8)	0.008*	4.1†
	Am-Si_2	2.5(2)	3.655(6)	0.008*	4.1†
	Am-Ca	2.1(2)	4.187(7)	0.008*	4.1†
Species 2: C/S 0.8 without Mal	Am-O	6.3(2)	2.437(2)	0.0090(3)	5.3(2)
	Am-Si_1	1.3(1)	3.162(6)	0.008*	5.3†
	Am-Si_2	0.9(2)	3.87(2)	0.008*	5.3†
	Am-Ca	0.9(2)	4.48(2)	0.008*	5.3†
Species 3: C/S 1.2 with Mal	Am-O	6.7(2)	2.424(2)	0.0098(4)	5.2(2)
	Am-Si	1.5(1)	3.119(7)	0.008*	5.2†
Eu(III)-tobermorite from Mandaliev *et al.* 2011 (C/S ~ 0.7). 28 d	Am-O	7.0(3)	2.41(0.8)	0.011(1)	6.9(8)
	Am-Si_1	0.6(2)	3.17(3)	0.004*	
	Am-Si_2	3.1(12)	3.70(6)	0.004*	
	Am-Ca	1.9(9)	3.75(6)	0.004*	

CN – Coordination number, *R* – interatomic distance, σ^2 - Debye-Waller factor, ΔE_0 – energy shift. Amplitude reduction factor $S_0^2 = 1.0$; † – linked to the respective O-shell, * - fixed parameter. The standard deviation of the fitted parameters is given in brackets.

5.6 Infrared spectroscopy

IR investigations were used for further structural characterization of the doped CSH phases (C/S 0.4, 1.0 and 2.0). The pure CSH phases (Figure 5.11) show IR spectra which are very similar to those of tobermorite.[240] All IR bands and their corresponding assignments are listed in Table 5.3.

The IR spectra show a complex structure of the bands between 800-1200 cm^{-1}, which represent the stretching vibrations of Si-O bonds. These can be classified into oscillations of the Q^1- and Q^2 tetrahedra of the silicate layers (see chapter 2.1.1 for Q^n classification).[240,241] The bands at ~ 970 cm^{-1}correspond to the Q^2 vibration and the bands at ~ 820 cm^{-1} to the Q^1 vibration.

At C/S ratio of 1.0 and 2.0, the Q^1 bands occur at 824 cm^{-1} and 818 cm^{-1} respectively (Figure 5.11), since at higher C/S ratios the fraction of Q^1 tetrahedra increases due to the reduction of bridging Q^2 tetrahedra. At C/S ratio of 0.4, however, only a small shoulder is visible. The Si-O-Si bending vibration is represented by a band at ~ 665 cm^{-1} and the deformation vibration of the Si tetrahedra is represented at ~ 455 cm^{-1}. The band at 1630 to 1640 cm^{-1} is due to water contained in the pellets and will not be considered further.

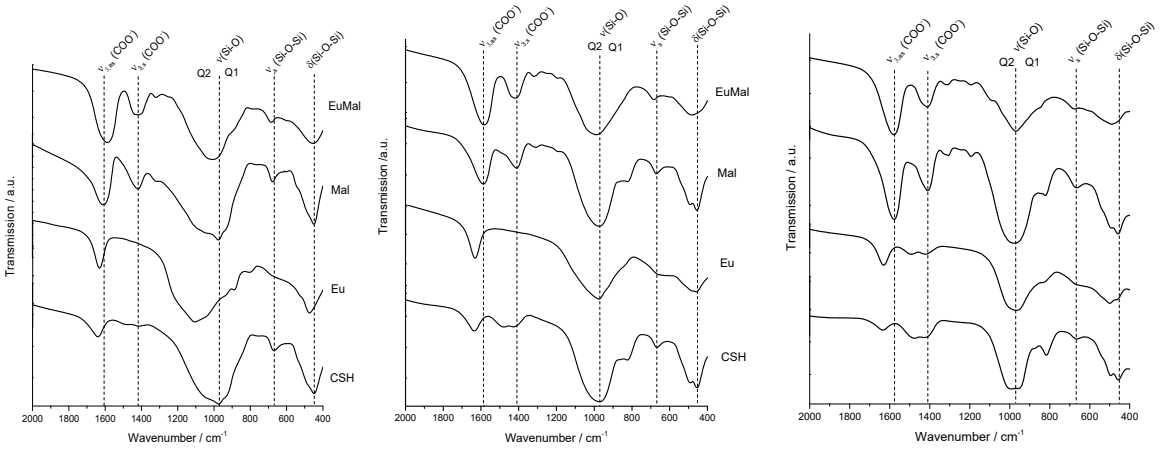

Figure 5.11: IR transmission spectra of doped C-S-H phases as KBr pellets for C/S ratio 0.4 (left), 1.0 (middle) and 2.0 (right) with 0.1 mol·L^{-1} Eu(III), 0.1 mol·L^{-1} Mal or 0.1 mol·L^{-1} Mal and 0.1 mol·L^{-1} Eu(III).

The samples with C/S ratio ~ 0.4 consist of CSH phase and SiO2 gel. The (Si-O) band is significantly broader, especially in the higher frequency range, than the same band at higher C/S ratios. This difference is due to the increased degree of polymerization of the SiO_2 gel by the presence of Q^3- and Q^4 tetrahedra.[242,243]

When Eu(III) is added, the stretching oscillation (Si-O) shifts from 974 cm^{-1} to the higher frequency range to 1105 cm^{-1}, indicating that the content of Q^2- tetrahedra in the CSH phases is decreased by Eu(III) or the silicate chains are converted to SiO_2 gel. In addition, oscillations at 889 cm^{-1} and 804 cm^{-1} become visible.

In the presence of Mal, the symmetrical and antisymmetrical stretching oscillations of the carboxylate groups are observed in the IR spectrum; the stretching and bending oscillations of the Si-O-Si bond do not change compared to the pure CSH phase. This confirms the assumption that Mal binds to the CSH phases as an outer-sphere complex and is not incorporated.

With simultaneous addition of Eu(III) and Mal, the $\nu_{3,as}(COO^-)$-oscillation shifts by 23 cm^{-1} and the $\nu_{3,s}(COO^-)$- oscillation becomes broader. This can indicate a possible Eu(III)-Mal complex, which is favored by the degradation of the CSH structure by Eu(III). The spectral splitting of the two $\nu_3(COO^-)$ bands in the CSH solids indicates a preferred monodentate coordination of the ligand in the investigated samples (see chapter 4.2.4 and [25]).

Table 5.3: Frequencies of the band maxima of the doped CSH solids and their assignment to the vibration modes. Frequencies in cm^{-1}.

CSH	CSH + Eu	CSH + Mal	CSH + EuMal	assignment
C/S 0.4				
449	474	447	453	δ(Si-O-Si)
669		677	685	ν(Si-O-Si)
974 sh	1105	977 sh	1007	ν(Si-O)
		1418	1416 br	$\nu_{3,s}(COO^-)$
		1610	1587	$\nu_{3,as}(COO^-)$
C/S 1.0				
455*/492	459	455*/492	482	δ(Si-O-Si)
667		671	683	ν(Si-O-Si)
972	976	972	989	ν(Si-O)
		1412	1416	$\nu_{3,s}(COO^-)$
		1587	1583	$\nu_{3,as}(COO^-)$
C/S 2.0				
457*/496	467/500*	457*/492	490	δ(Si-O-Si)
665	sh	669	677	ν(Si-O-Si)
974 br	966 br	977 br	968	ν(Si-O)
		1410	1412	$\nu_{3,s}(COO^-)$
		1578	1580	$\nu_{3,as}(COO^-)$

* – band with higher intensity, br – broad, sh – shoulder

Furthermore, carbonate bands at ~ 1400 cm^{-1} can be observed in the pure CSH phases (especially at the higher C/S ratio of 1.0 and 2.0). Since these bands have a very low relative intensity, a carbonate content only in the lower percentage range can be assumed.

At C/S ratio of 1.0, these bands are no longer observed if Eu(III) is present, which suggests, that the carbonate is displaced by Eu(III) from the interlayer. It is interesting to point out that at a C/S ratio of 2.0, this displacement does not occur or occurs only to a small extent. This is due to the presence of portlandite, to which Eu(III) shows a high affinity (see also chapter 4.2.2). Whether Mal, like Eu(III), displaces the carbonate from the interlayers cannot be deduced due to the strong interfering $\nu_{3,as}(COO^-)$- and $\nu_{3,s}(COO^-)$ modes. Similar to the C/S ratio of 0.4, the ν(Si–O) band becomes broader in the higher frequency range and the Q^1 band at 820 cm^{-1} disappears in the presence of Eu(III) (more pronounced at the C/S ratio of 1.0). The additional decrease of the (Si-O-Si) band intensity at 670 cm^{-1} or its broadening is explained by a low order of the samples. The internal deformation of the SiO_4 tetrahedra is visible by a strong change of the δ(Si–O–Si)-band.

Mal has no influence on the degree of polymerization of the CSH phases, even at high C/S ratios. Since the $\nu_3(COO^-)$ bands shift by a maximum of 4 cm^{-1} when Mal and Eu(III) are added, it can be assumed that Eu does not dominantly complex with Mal within the phases (for C/S ≥ 1.0). Ternary Eu(III)-Mal-CSH complexes are therefore very unlikely. Furthermore, in the range of Si-O(-Si) oscillations the IR spectra of the Eu(III)-Mal-doped CSH phases are a mixture and/or overlap of the individual IR spectra of the Mal-doped and the Eu(III) doped CSH phases (at all C/S ratios). This supports the assumption that Eu(III) and Mal will sorb/incorporate independently of each other on/in the CSH phases.

At C/S 2.0, the OH-vibration of the portlandite can be also observed at ~ 3640 cm^{-1}. However, this only occurs in the pure CSH phase or at low Eu(III) and Mal concentrations. At higher concentrations of Eu(III), the binding of Eu(III) to portlandite seems to suppress/shift this oscillation. But it should be noted, that at high metal concentrations (high metal to CSH ratio) probably no CSH phases are present.

6 Summary and conclusion

The present report deals with structural and thermodynamic investigations on the retention of trivalent actinides (An) and lanthanides (Ln) at calcium silicate hydrates (CSH) phases (and calcium aluminate hydrate phases, CAH) in the presence of (α-hydroxy)carboxylates.

Hydroxycarboxylates like malate, tartrate, gluconate and citrate and are constituents of cement additives and serve as retarders. Malate (Mal, hydroxysuccinic acid) was used as model ligand for α-hydroxycarboxylate based cement additives. For comparison, the natural occurring ligands lactate (Lac) and oxalate (Oxa) were also considered. Furthermore, because polycarboxylate-ethers (PCE) are today the most widely used superplasticizers in the cement industry, thermodynamic investigations on the interaction of PCE with trivalent Ln were also performed.

CSH phases are the main phases in concrete and they are considered as the actinide uptake controlling phases. However, in cement/concrete mixed calcium silicate/aluminate hydrate phases (CA(S)H) are also present in significant quantities, which is why additional investigations were performed with pure calcium aluminate hydrate (CAH) phases.

Using a multi-method approach - a combination of spectroscopic, theoretical and thermodynamic investigations - the binary systems Ln(III)/An(III)-ligand, Ln(III)/An(III)-CSH and ligand-CSH phase as well as the ternary system Ln(III)/An(III)-ligand- CSH phase were characterized.

The complex formation reactions of the here investigated Ln(III)/An(III)-ligand systems are predominantly endothermic and entropy-driven. The interaction of Eu(III) with PCE is strongly endothermic. Therefore, higher temperatures, as expected in the near field of a nuclear repository, favor the complexation of Ln(III)/An(III) with these organic ligands.

Higher ionic strengths should also be considered when water ingresses into potential host rocks, such as clay formations or salt domes, of a nuclear repository. With increasing ionic strength, the enthalpy of the studied complexation reactions decrease. Thus, in solutions of higher ionic strengths such complexation reactions are not necessarily favored at higher temperatures. This underlines that the ionic strength is an important parameter and must be considered in modelling.

The An(III)/Ln(III)-ligand systems are mainly characterized by a moderate complexation strength (for instance for PCEs with $\log K_1 \sim 4.5$ to 5.5 at I = 0.1 m, for Am(III)-Mal with $\log \beta_1 = 6.1 \pm 0.3$ at I = 0 m). The complexation constants decrease with increasing ionic strength.

For the estimation and interpretation of thermodynamic data, fundamental structural investigations of the considered An/Ln-ligand systems are necessary, as shown exemplarily for the An(III)/Ln-Mal system. The studies confirmed two complexes with a 1:1 and 1:2 stoichiometry, respectively. Up to pH 6 no further complexes, such as a 1:3 or protonated species were found. Above pH 6, next to polynuclear An(III)/Ln(III)-hydrolysis species, a polynuclear An(III)/Ln(III)-Mal complex is precipitating. It was not possible to observe further complexes in the alkaline pH range (like ternary complexes

An(III)/Ln(III)-OH-Mal or quaternary Ca- An(III)/Ln(III)-OH-ligand complexes). The exact speciation of Ln(III)/An(III) in the alkaline pH range in the presence of medium to strong complexing organic ligands is still an open question.

Mal chelates the cations of the 4f and 5f elements in a tridentate ring structure in which the α-hydroxyl group and both carboxylate groups are involved (structural model in Figure 6.1 above). By comparing the An(III)/Ln(III)-succinate (no OH group) and An(III)/Ln(III)-malate complexes, the contribution of an α-OH group to the increase of the stability constant can be estimated to be of one order of magnitude. The α-hydroxyl group also has a major influence on the structure of the precipitated An(III)-ligand complexes in the alkaline *pH*. In the investigated Am(III)-Mal solid Mal remains in the tridentate structure. In contrast, in the precipitated Am(III)-Suc complex there is a change in the coordination, which results in an open-chain structure.

The batch sorption studies of An(III)/Ln(III) on the CSH/CAH cement phases reveal a strong sorption behavior of An(III)/Ln(III) both in the binary system without Mal as well as in the ternary system with Mal, thus leading to high K_d-values ($K_d > 10^4$ L·kg^{-1}) independently of the used C/S or S/L ratio. The almost quantitative An(III)/Ln(III) sorption on the CSH phases is not influenced by Mal, and likewise, the uptake of Mal is only minimally influenced by the presence of the metal ions. Malate shows only weak sorption with $K_d \sim 10^1$ to 10^2 L·kg^{-1} to the cement phases, which increases slightly with increasing C/S ratio due to an enhanced Ca ion mediated *outer sphere* sorption on the CSH surface and in the CSH interlayer (Figure 6.1 bottom, middle). The Ln(III)/An(III) ions and the ligand molecules show independent (ab-)sorption mechanisms.

The spectroscopic investigations indicate a homogeneous distribution of two An(III)/Ln(III) species in the CSH phases: an incorporated species, which is completely dehydrated within the CaO layer and an inner sphere sorbed species with 1 - 3 remaining water molecules in the CSH intermediate layer or on the CSH surface (Figure 6.1 bottom left). At high C/S ratios > 2 a further An(III)/Ln(III) species appears. As portlandite is only formed at these high C/S ratios, it is assumed that this third species mainly associated with portlandite.

In the ternary Ln(III)/An(III)-Mal-CSH system, at low C/S ratio << 1 both species are present in a slightly stronger ligand field in the presence of Mal than at higher C/S ratio. At the pH ~ 10, which is prevailing in these CSH phases, the An(III)/Ln(III)-Mal complexation is no longer dominant but still possible. The uptake of this complex or of a An(III)/Ln(III)-OH-Mal complex in the CSH phases could be a possible reason of the spectroscopic changes. But so far, there is no clear evidence of a sorbed or incorporated An(III)/Eu(III)-Mal complex in the CSH phases. At C/S ratio ≥ 1 the species show an increased crystallinity respectively an increased degree of order and increased symmetry in contrast to the samples without Mal. These structural changes of the CSH phases are probably favored by the hydration retarding effect of the α-hydroxycarboxylate and by a strong Ca-ligand complexation (Figure 6.1 bottom right). Due to the complexation of Mal with Ca the formation of portlandite at high C/S ratios is inhibited and/or retarded and thus, the An(III)/Ln(III)-portlandite species is also influenced by Mal.

In the present work the process understanding of the influence of organic ligands on the An(III)/Ln(III) retention in CSH phases has been significantly extended and improved. Summarizing, it can be concluded that the presence of Mal results in highly symmetrical An(III)/Ln(III) species in a more ordered

(crystalline) CSH structures. This species has probably only a small number of available sorption sites and can therefore only be detected at low metal concentrations. The retention of An(III)/Ln(III) by the CSH phases is not influenced. The organic ligands themselves are weakly sorbed on the CSH phases as outer sphere complexes. For moderate complexing ligands, like Mal, there is no desorption of the trivalent actinides/lanthanides by formation of soluble An(III)/Ln(III)-ligand complexes. This is an important aspect for the permanent retention of trivalent actinides in a nuclear repository. Figure 6.1 illustrates the results of this work in a schematic summary.

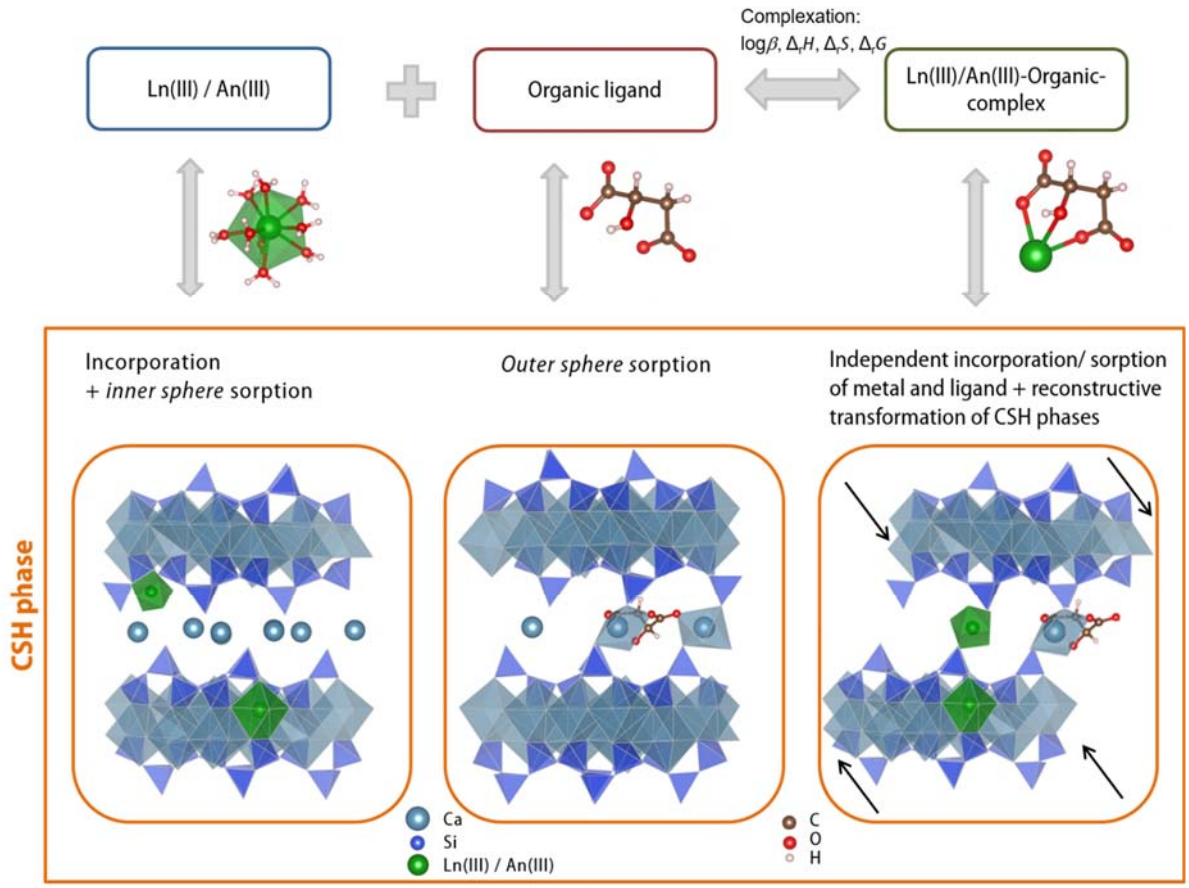

Figure 6.1: Schematic illustration of the results of this project. A tridentate coordination of Ln(III)/An(III) with Mal and corresponding thermodynamic data were determined (chapter 4). The Ln(III)/An(III)-Mal-CSH system was analyzed and a possible transformation processes of the CSH phases by influence of Mal was identified (bottom, chapter 5). H and O atoms within the CSH structure were neglected for simplification. With permission and adapted from[25].

7 Appendix

Table 7.1: Used Chemicals

Substance	Company		Purity
Neodymium(III) chloride hexahydrate	Alfa Aesar	Massachusetts, USA	≥ 99 %
Europium(III) chloride hexahydrate	Sigma-Aldrich	Missouri, USA	99,99 %
L-(−)-malic acid	Sigma-Aldrich	Missouri, USA	≥ 99 %
L-(−)-malic acid disodium salt	Goldbiotechnologie	Missouri, USA	99 %
L- lactic acid 90 %	PanReac Applichem	Germany / Spain	
sodium L-lactate	Sigma-Aldrich	Missouri, USA	99,99 %
oxalic acid	Sigma-Aldrich	Missouri, USA	≥ 99 %
sodium oxalate	Sigma-Aldrich	Missouri, USA	≥ 99,5 %
Commercial PCE: Glenium®51 [124]	BASF Construction Solution GmbH	Germany	
Synthetic PCE: 52IPEG4.5 [125], 45PC6	J. Plank, TU München, Lehrstuhl für Bauchemie	Germany	
Sodium polyacrylate PA5100 M_w = 5100 g/mol	Sigma-Aldrich	Missouri, USA	
Sodium chloride NaCl	VWR Chemicals	Leuven, Belgium	≥ 99,5 %
NaOH pellets	VWR Chemicals	Leuven, Belgium	≥ 99,5 %
Calciumaluminate C_3A precursor	Mineral Research Processing,	France	

Table 7.2: Conditional stability constants for complexation reactions of Mal with various trivalent metal ions from the literature at $T = 25$ °C.

Ln(III)	ionic strength / medium	n	log β_n	reference / method
Nd	0.1 M KNO_3	1	4.65 ± 0.17	[106], spec
		2	7.17 ± 0.15	
Nd	0.1 M $NaClO_4$	1	4.77 ± 0.01	[244], pot
		2	7.94 ± 0.02	
Nd	0.2 M $NaClO_4$	1	4.45 ± 0.01	[245], pot
Nd	0.1 M KCl	1	4.60 ± 0.02	[197], pot
		2	9.16 ± 0.03	
Nd	0.1 M KCl	1	5.12 ± 0.02	[107], pot †
		2	8.76 ± 0.05	
		3	11.68 ± 0.11	
Gd	0.1 M $NaClO_4$	1	4.74 ± 0.03	[246], pot
		2	7.68 ± 0.08	
Eu	0.1 M $NaClO_4$	1	4.85 ± 0.03	[244], pot
		2	8.11 ± 0.09	
Eu	0.1 M $NaClO_4$ (0,004 M NaAc)	1	3.65	[247], ex
		2	6.15	
Eu	1.0 M $NaClO_4$	1	4.33 ± 0.01	[199], spec
		2	7.37 ± 0.01	
		3	9.24 ± 0.02	
Sm	0.1 M $NaClO_4$	1	4.89 ± 0.03	[244], pot
		2	8.16 ± 0.07	
Sm	2.0 M $NaClO_4$	1	3.9	[339], qh
		2	6.48	

qh – quinhydron-electrode; pot – potentiometry (H^+- Glass electrode); spec – spectroscopy; ex – Liquid-liquid extraction; † – T = 30 °C

Table 7.3: Experimental stability constants, enthalpies and entropies of Ln(III)/An(III)-Mal complexes compared to literature values of similar ligand systems at I_m = 0 (NaCl)

system / method / Ref.	$\log \beta^0_1$	$\log \beta^0_2$	$\Delta_r H^0_{m,1}$ / kJ·mol^{-1}	$\Delta_r H^0_{m,2}$ / kJ·mol^{-1}	$\Delta_r S^0_{m,1}$ / J·mol^{-1}K^{-1}	$\Delta_r S^0_{m,2}$ / J·mol^{-1}K^{-1}
Nd(III)-Mal / ITC / d. A.	6.0 ± 0.4	9.1 ± 0.7	6.4 ± 0.1	4.4 ± 0.9	137 ± 7	188 ± 13
Nd(III)-Mal / UV-Vis / d. A.*	5.7 ± 0.5	8.2 ± 0.8				
Eu(III)-Mal / TRLFS / d. A.*	5.8 ± 0.5	8 ± 1				
Am(III)-Mal / ITC / d. A.*	6.1 ± 0.3	9.4 ± 0.5	5.8 ± 0.5	3 ± 1	136 ± 6	190 ± 20
Eu(III)-Lac / Pot, ITC / [185]	3.48 ± 0.15	6.16 ± 0.18	1.65 ± 0.90	−1.51 ± 1.10	71.2 ± 6.38	112.9 ± 7.05
Cm(III)-Prop / TRLFS / [188]	3.12 ± 0.09	4.51 ± 0.51	5.7 ± 1.8	49.9 ± 4.0	83.6 ± 5.2	256.7 ± 12.2
Cm(III)-Suc / TRLFS /[182] #	5.15 ± 0.13	7.63 ± 0.14	2.2 ± 6.7	35.9 ± 7.5	105.5 ± 21.6	265.4 ± 24.0
Cm(III)-Malo / TRLFS / [248] #	5.28 ± 0.19	8.49 ± 0.23	8.69 ± 1.62	18.51 ± 3.16	129.05 ± 4.74	223.33 ± 9.79
Cm(III)-Oxa / TRLFS /[123] #	6.86 ± 0.06	11.57 ± 0.10	−2.7 ± 0.8	8.1 ± 2.0	121.8 ± 2.9	247.8 ± 4.3
Nd(III)-Oxa / ITC / d. A.	6.2 ± 0.6		−6.0 ± 1.8		99 ± 23	
Am(III)-Oxa [102]	6.51 ± 0.15	10.71 ± 0.20				
Cm(III)-Cit / TRLFS / [187]	9.3 ± 0.2	13.2 ± 0.7				
Am(III)-Cit [102]	8.55 ± 0.20	13.9 ± 1.0				
Am(III)-HCit [102]	6.5 ± 1.0	10.8 ± 1.0				

d. A. – this work; * – extrapolated using the SIT parameters of Nd(III)-Mal-system from ITC-measurements; # – at T = 30 °C; Pot – Potentiometry, Suc – succinate; Oxa – oxalate; Prop – propionate; Malo – malonate; Cit – citrate; All uncertainties have been calculated according to OECD NEA-TDB[102] recommendations and are displayed in 2σ -values.

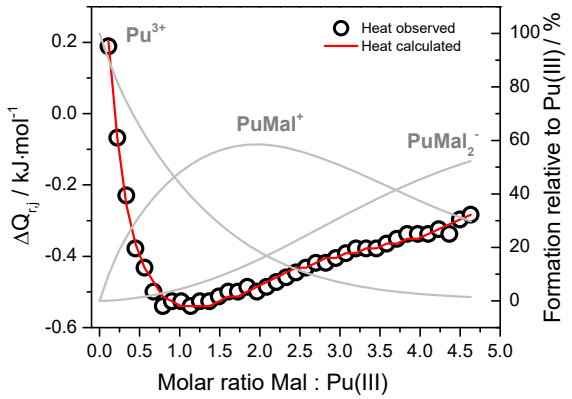

Figure 7.1: Calorimetric heat curves of Pu(III)-Mal titration [Pu] = $3.2 \cdot 10^{-3}$ mol·L^{-1} and [Mal] = $7.16 \cdot 10^{-2}$ mol·L^{-1}; pH_C = 3.95; I_M = 0.61 NaCl. $\Delta Q_{r,j}$ – integrated stepwise heat for each titration step *j*, log β_1 = 4.8 ± 1

Table 7.4 Conditional stability constants and enthalpy values of the complexation of Eu(III) with 45PC6 as function of ionic strength of NaCl and $CaCl_2$ at T = 25 °C

I_m / mol·kg^{-1}	pH_{exp} ± 0.05	log K_{11} ± 2σ	$\Delta_r H_{11}$ ± 2σ / kJ·mol^{-1}	pH_{exp} ± 0.05	log K_{11} ± 2σ	$\Delta_r H_{11}$ ± 2σ / kJ·mol^{-1}
	NaCl, pH_c = 6.20 ± 0.05			$CaCl_2$, pH_c = 6.30 ± 0.05		
0.1	6.00	4.9 ± 0.1	61 ± 2	6.25	4.9 ± 0.1	44 ± 3
0.3	5.76	5.0 ± 0.3	59 ± 2	6.02	4.7 ± 0.1	47 ± 5
0.5	5.64	4.7 ± 0.2	64 ± 3	5.94	4.5 ± 0.2	47 ± 2
0.7	5.53	4.6 ± 0.2	66 ± 3	5.98	4.3 ± 0.2	46 ± 3
1.0	5.43	4.4 ± 0.2	65 ± 5	5.80	4.2 ± 0.3	42 ± 2
1.5	5.31	4.0 ± 0.3	55 ± 6	5.67	4.1 ± 0.3	33 ± 4
2.0	5.28	3.8 ± 0.3	61 ± 3	5.62	4.0 ± 0.4	27 ± 4
0.1[125 a)]	$[H+]_{total}$ = 10^{-4} mol·kg^{-1}	6.54 ± 0.28	-17.6 ± 4.9			

[a)] 52IPEG4.5, T = 20 °C, TRLFS, data analyzed with charge neutralization model by Kim and Czerwinski

Table 7.5: Conditional stability constants and enthalpy values of the complexation of Eu(III) with PA5100 as function of ionic strength of NaCl and $CaCl_2$ at $T = 25$ °C

I_m / mol·kg^{-1}	pH_{exp} ± 0.05	log K_{11} ± 2σ	$\Delta_r H_{11}$ ± 2σ / kJ·mol^{-1}	pH_{exp} ± 0.05	log K_{11} ± 2σ	$\Delta_r H_{11}$ ± 2σ / kJ·mol^{-1}
	NaCl, $pH_c = 6.50 \pm 0.05$			$CaCl_2$, $pH_c = 5.35 \pm 0.05$		
0.1	6.36	5.6 ± 0.2	48 ± 2	5.20	4.8 ± 0.1	22 ± 3
0.3	6.00	5.4 ± 0.2	49 ± 2	4.90	4.5 ± 0.2	22 ± 3
0.5	5.79	5. 4 ± 0.2	48 ± 3	4.83	4.4 ± 0.2	23 ± 4
0.7	5.73	5.4 ± 0.2	48 ± 2	4.71	4.3 ± 0.2	23 ± 3
1.0	5.52	5.3 ± 0.2	48 ± 2	4.58	4.2 ± 0.2	24 ± 2
1.5	5.37	5.4 ± 0.2	49 ± 3	4.50	4.0 ± 0.3	25 ± 2
2.0	5.24	5.4 ± 0.2	48 ± 3	4.43	3.9 ± 0.3	27 ± 4
0.1 [126 a)]	$[H^+]_{total} = 10^{-4}$ mol·kg^{-1}	5.87 ± 0.28				
not given [191 b)]	3.0-5.5	3.7 ± 0.3				

[a)] PA with molar weights ~ 2100 g/mol, T = 20 °C, TRLFS, data analyzed with charge neutralization model by Kim and Czerwinski, [b)] PA with molar weights ~ 2000 and ~ 5000 g/mol, T = 20 °C, TRLFS

Table 7.6: Conditional stability constants and enthalpy values of the complexation of Eu(III) with Glenium®51 as function of pH_c in 0.1 m NaCl at $T = 25$ °C, [Eu^{3+}] (2 - 6)·10^{-3} mol/kg

$pH_c \pm 0.05$	*[Glenium®51] / mg/g*	$\log K_{11} \pm 2\sigma$	$\Delta_r H_{11} \pm 2\sigma$ / kJ·mol^{-1}
5.90	3	5.0 ± 0.1	66 ± 3
5.80	3	4.9 ± 0.2	58 ± 4
5.25	2.2	4.8 ± 0.3	55 ± 5
5.03	12 [a)]	4.2 ± 0.2	51 ± 3
4.51	25 [a)]	3.6 ± 0.2	56 ± 6
4.45	20 [a)]	3.6 ± 0.2	57 ± 7
4.21	100 [a)]	3.1 ± 0.3	52 ± 10

[a)] At pH values below 5 only a very small fraction of the carboxylic groups of the PCEs are deprotonated. Therefore, a relatively high concentration of the PCE-ligand is necessary to obtain an analyzable heat curve.

Table 7.7: Entropy values of the complexation of Eu(III) with Glenium®51 , PCE 45PC6 and PA5100 as function of ionic strength of NaCl and $CaCl_2$ at $T = 25$ °C. Values were calculated according to equation 3.28 with the conditional stability constants and enthalpy values for Glenium®51, 45PC6 and PA5100 taken from Table 4.4,

Table 7.4 and Table 7.5, respectively

	$\Delta_r S_{11} \pm 2\sigma$ / kJ·Kmol^{-1}·K^{-1}					
I_m / mol·kg^{-1}	*Glenium®51*	45PC6	PA5100	*Glenium®51*	45PC6	PA5100
	NaCl			CaCl		
0.1	305 ± 9	298 ± 9	268 ± 11	248 ± 9	241 ± 12	166 ± 12
0.3	298 ± 11	294 ± 12	268 ± 11	247 ± 14	248 ± 19	160 ± 14
0.5	389 ± 11	305 ± 14	264 ± 14	226 ± 14	244 ± 11	161 ± 17
0.7	302 ± 11	309 ± 14	264 ± 11	205 ± 21	237 ± 14	159 ± 14
1.0	283 ± 11	302 ± 21	264 ± 11	178 ±19	221 ± 12	161 ± 11
1.5	298 ± 19	261 ± 26	268 ± 14	148 ± 23	189 ± 19	160 ± 12
2.0	303 ± 19	277 ± 16	268 ± 14	121 ±23	167 ± 21	165 ± 19
0.1	152 ± 42[124]	63.9 ± 15.7[125]				

error calculation of $\Delta_r S_{11}$: $2\sigma_{\Delta S} = \frac{1000 \cdot 2\sigma_{\Delta H}}{T} + 2.303 \cdot R \cdot 2\sigma_{logK}$

Table 7.8: Momentum analysis of the radial particle distribution function (RPDF) of AIMD simulated structures for selected R ranges. AIMD calculated average structures of the Nd(III)-aquo ion and the tridentate 1:1 Nd(III)-Mal complex with and without water molecules (below). Nd(III) was replaced by Am(III).

	***R*-range/ Å**	**CN**	***R* / Å**	**σ^2 / Å²**
Am-$(H_2O)_9$·$(H_2O)_n$	2.00–3.00 (O)	9.0	2.55	0.0091
Am-Mal$(H_2O)_6$·$(H_2O)_n$	2.00-3.40 (O)	8.8	2.55	0.0269
	3.00-3.75 (C)	3.0	3.40	0.0116
	3.75-4.30 (C)	1.0	4.01	0.0097
Am-Mal	2.00-3.00 (O)	3.0	2.53	0.0100
	4.00-5.00 (O)	2.0	4.52	0.0137
	3.00-3.75 (C)	3.0	3.40	0.0116
	3.75-4.30 (C)	1.0	4.01	0.0097

CN – coordination number, R – Binding distance, σ^2 – Debye-Waller factor.

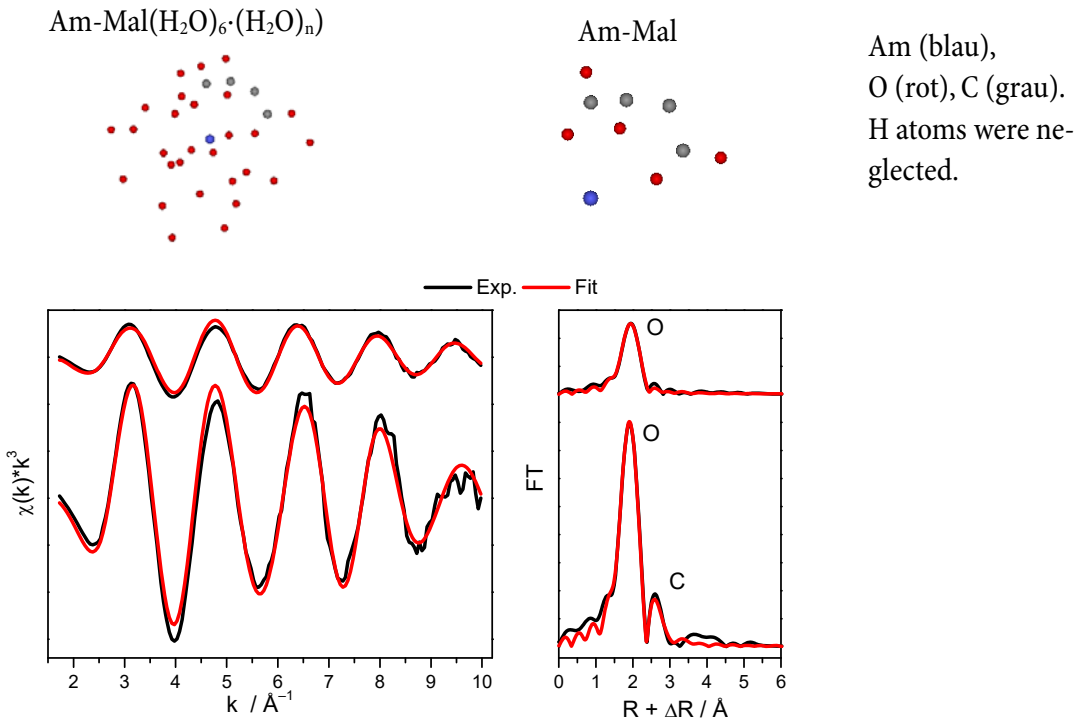

Figure 7.2: Shell fit (red) of ITFA-isolated EXAFS spectra (left, black) of component 1 (a coordinated water molecule, top) and of component 2 (a coordinating Mal ligand, bottom) assuming the AIMD structure of the tridentate Am(III)-Mal complex. Corresponding Fourier transformations (FT) (right).

Table 7.9: Distribution coefficients of trivalent Ln/An and Mal on CSH phases determined in this work

sorptive	concentration of sorptive mol·L^{-1}	[Mal] mol·L^{-1}	C/S ratio	*pH*, medium	S/L kg·L^{-1}	log K_d
Eu(III)	$2{\cdot}10^{-4}$	-	0.4 – 2	H_2O	$2.0{\cdot}10^{-4}$	4.07 ± 0.02
	$2{\cdot}10^{-4}$	$2{\cdot}10^{-4}$	0.4 – 2	H_2O	$2.0{\cdot}10^{-4}$	4.25 ± 0.23
	$2{\cdot}10^{-4}$	$1{\cdot}10^{-4}$ - $1{\cdot}10^{-2}$	0.8	H_2O	$1{\cdot}10^{-2}$	5.18 ± 0.91
Cm(III)	$3{\cdot}10^{-6}$	$2{\cdot}10^{-2}$	1.0	0.3 M NaOH	$2.4{\cdot}10^{-2}$	4.74 ± 0.95
	$3{\cdot}10^{-6}$	$2{\cdot}10^{-2}$	2.0	0.3 M NaOH	$2.4{\cdot}10^{-2}$	4.50 ± 0.82
Am(III)	$1{\cdot}10^{-4}$	-	0.4 – 1.2	H_2O	$2{\cdot}10^{-3}$	4.39 ± 0.33
	$1{\cdot}10^{-4}$	$2{\cdot}10^{-3}$	0.4 – 1.2	H_2O	$2{\cdot}10^{-3}$	4.33 ± 0.89
Mal		$1{\cdot}10^{-4}$	0.4	H_2O	$1{\cdot}10^{-2}$	0.63 ± 0.11
		$1{\cdot}10^{-4}$ - $1{\cdot}10^{-2}$	0.8	H_2O	$1{\cdot}10^{-2}$	1.32 ± 0.18
		$1{\cdot}10^{-4}$	2.2	H_2O	$1{\cdot}10^{-2}$	2.52 ± 0.21
		$1{\cdot}10^{-4}$ - $1{\cdot}10^{-2}$	0.8	ACW	$1{\cdot}10^{-2}$	1.52 ± 0.19
	[Eu] = $2{\cdot}10^{-4}$	$1{\cdot}10^{-4}$ - $1{\cdot}10^{-2}$	0.8	H_2O	$1{\cdot}10^{-2}$	1.73 ± 0.23
	[Eu] = $2{\cdot}10^{-4}$	$1{\cdot}10^{-4}$ - $1{\cdot}10^{-2}$	0.8	ACW	$1{\cdot}10^{-2}$	1.82 ± 0.40

Table 7.10: Distribution coefficients of Eu(III) and Mal on CAH phase katoite determined in this work

sorptive	concentration of sorptive mol·L^{-1}	[Mal] mol·L^{-1}	C/A ratio	*pH*, medium	S/L kg·L^{-1}	log K_d
Eu(III)	$1 \cdot 10^{-4}$	-	Katoite (1.5)	0.1 M NaOH	$(7 \pm 4) \cdot 10^{-3}$	4.75 ± 0.12
	$1 \cdot 10^{-4}$	$1 \cdot 10^{-4}$ - $1 \cdot 10^{-2}$	Katoite (1.5)	0.1 M NaOH	$(7 \pm 4) \cdot 10^{-3}$	4.38 ± 1.20
Mal		$1 \cdot 10^{-4}$ - $1 \cdot 10^{-2}$	Katoite (1.5)	0.1 M NaOH	$(7 \pm 4) \cdot 10^{-3}$	1.94 ± 0.94
	[Eu] = $1 \cdot 10^{-4}$	$1 \cdot 10^{-4}$ - $1 \cdot 10^{-2}$	Katoite (1.5)	0.1 M NaOH	$(7 \pm 4) \cdot 10^{-3}$	2.22 ± 0.28

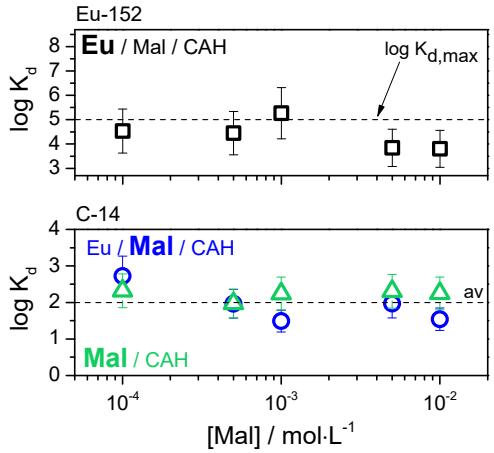

Figure 7.3: Log K_d-values of ^{152}Eu (top) or ^{14}C- labelled Mal (bottom) as function of the Mal concentration at katoite with [Eu] = $1 \cdot 10^{-4}$ mol·L^{-1}. The used radioactive element/molecule is marked in bold.

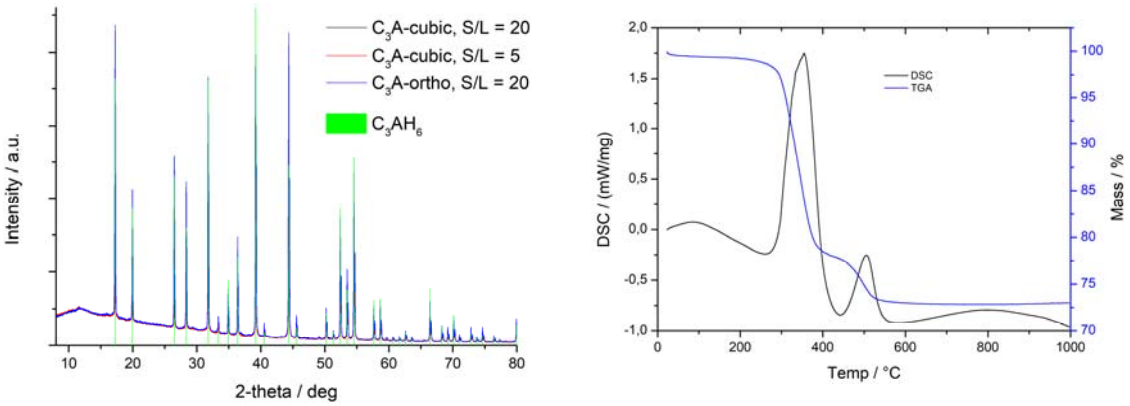

Figure 7.4: p XRD-diffraction pattern of the formation CAH phase katoite as function of solid/liquid ratio and the crystal structure of the used precursor (left) and typical thermogravimetric analysis (TGA) and DSC-signal of katoite (right)

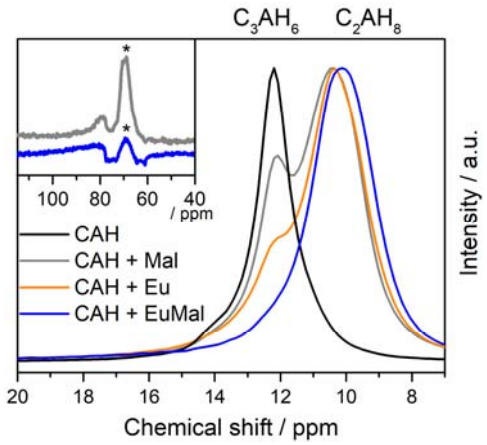

Figure 7.5: ^{27}Al NMR spectra the pure and with Eu(III) and Mal doped CAH phase (katoite). [Eu] = $5{\cdot}10^{-3}$ mol·L^{-1}/ [Mal] = $5{\cdot}10^{-3}$ mol·L^{-1}

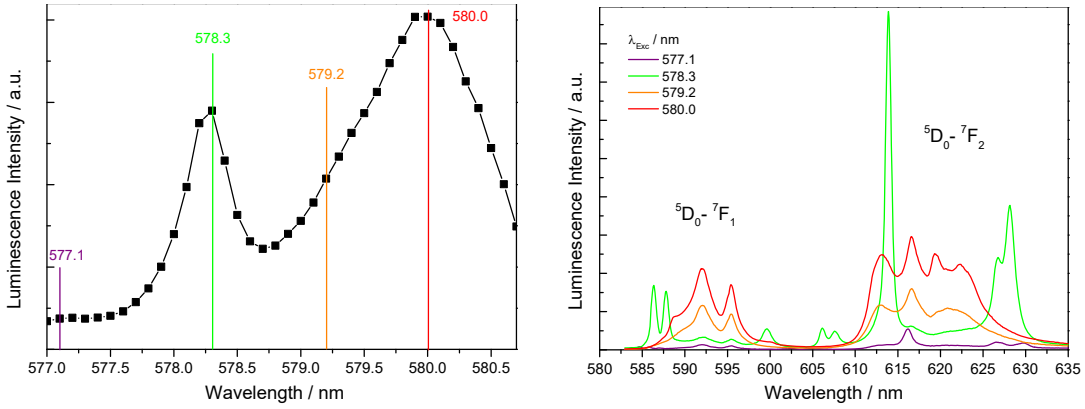

Figure 7.6: Excitation spectra of Eu(III)-doped CAH-solids RT (left), Fluorescence emission spectra of Eu(III)-doped CAH solid at excitation in the $^5D_0$-$^7F_0$ transition with different excitation wavelength (right), [Eu] = $2{\cdot}10^{-2}$ mol·L^{-1}, T = 20 K

Table 7.11: Lifetimes of Am(III)/Cm(III)/Eu(III)- and Am(III)/Cm(III)/Eu(III)-Mal-doped C-S-H phases at room temperature (RT) in H_2O or low temperature (TT) < 20 K

Sample	**C/S**	**An(III)-CSH**		**An(III)-Mal-CSH**	
		τ / µs	n (H_2O / OH)*	τ / µs	n (H_2O / OH)*
Am(III) RT	0.4	$(172 \pm 25)\cdot10^{-3}$		$(272 \pm 14)\cdot10^{-3}$	
Am(III) RT	0.8	$(228 \pm 19)\cdot10^{-3}$		$(202 \pm 23)\cdot10^{-3}$	
Am(III) RT	1.2	$(194 \pm 12)\cdot10^{-3}$		$(189 \pm 7)\cdot10^{-3}$	
Cm(III) cryo [§]	1.0	163 ± 111 [249]	3.1 [249]	205 ± 66	2.3
		977 ± 51 [249]	0 [249]	703 ± 16	0
Cm(III) cryo [§]	2.0	214 ± 28 [249]	2.2 [249]	153 ± 16	3.4
		928 ± 109 [249]	0 [249]	674 ± 16	0.1
Cm(III) [77]	1.0	289 ± 11	1.4		
		1482 ± 200	0		
Eu(III) RT	0.4	56 ± 30[#]	-	55 ± 24[#]	-
λ_{exc} = 394 nm		538 ± 106/ 689 ± 112 [#]	1.4/ 0.9	474 ± 21 / 667 ± 42#	1.6/ 1.0
		1962 ± 300/ 1941 ± 336[#]	0/ 0	1999 ± 65/ 2240 ± 71#	0/ 0
Eu(III) TT	0.4	618 ± 95	1.1	755 ± 95	0.8
λ_{exc} = 579.5 nm		2385 ± 176	0	3348 ± 553	0
Eu(III) TT	1.0	774 ± 84	0.8	400 ± 167	2.1
λ_{exc} = 579 nm		2834 ± 294	0	1820 ± 121	0
Eu(III) TT	2.0	537 ± 58	1.4	845 ± 60	0.6
λ_{exc} = 579 nm		1797 ± 142	0	2733 ± 234	0
Eu(III) [76]	0.83	570	1.3		
		980	0.5		

RT – room temperature; TT – low temperature; [#] – tri-exponential fit; [§] – in ACW; * –uncertainty ± 0.5 according to Kimura et al. [205] and Horrocks et. al.[143] All other uncertainties are shown in 1σ values.

8 References

[1] Gesetz zur Suche und Auswahl eines Standortes für ein Endlager für Wärme entwickelnde radioaktive Abfälle (Standortauswahlgesetz – StandAG); Bundesgesetzblatt Jahrgang 2013 Teil I Nr. 41, 2013

[2] I. Bredberg, J. Hutter, A. Koch, K. Kühn, K. Niedzwiedz, F. Philippczyk and R. Wähning, Statusbericht zur Kernenergienutzung in der Bundesrepublik Deutschland 2017, Abteilung Kerntechnische Sicherheit und atomrechtliche Aufsicht in der Entsorgung, Salzgitter, 2018.

[3] A. Schwenk-Ferrero, German Spent Nuclear Fuel Legacy: Characteristics and High-Level Waste Management Issues, Sci. Technol. Nucl. Install., 2013, 1–11.

[4] A. Lommerzheim, M. Jobmann (2014): Endlagerkonzept sowie Verfüll- und Verschlusskonzept für das Standortmodell NORD, Technischer Bericht, DBE-TECHNOLOGY GmbH, Stand 9.10.2014

[5] H. F. W. Taylor, Cement Chemistry, Academic Press, London, 1990.

[6] I. G. Richardson, The calcium silicate hydrates, Cem. Concr. Res., 2008, 38, 137–158.

[7] I. G. Richardson, The nature of CSH in hardened cements, Cem. Concr. Res., 1999, 29, 1131–1147.

[8] J. D. Bernal, J. W. Jeffery and H. F. W. Taylor, Crystallographic Reasearch on the Hydration of Portland Cement. A first Report on investigations in Progress., Magn Concr Res, 1952, 4, 49–54

[9] E.W. Locher: Zement-Grundlagen der Herstellung und Verwendung, Verlag Bau und Technik, Düsseldorf, 2000

[10] P. Zhang, G. Qian, H. Shi, X. Ruan, J. Yang, R. L. Frost, Mechanism of interaction of hydrocalumites (Ca/Al-LDH) with methyl orange and acidic scarlet GR. Journal of Colloid and Interface Science 2012, 365, 110–16.

[11] G. Renaudin, M. Francois, O. Evrard, Order and disorder in the lamellar hydrated tetracalcium monocarboaluminate compound, Cement and Concrete Research, 1999, 29, 63-69

[12] J. Qu, L. Sha, C. Wu and Q. Zhang, Applications of Mechanochemically Prepared Layered Double Hydroxides as Adsorbents and Catalysts: A Mini-Review, Nanomaterials, 2019, 9, 80

[13] M. Atkins and F. P. Glasser, Application of Portland Cement-based materials to radioactive waste immobilization, Waste Manag., 1992, 12, 105–131.

[14] F. Bart, C. Cau-dit-Coumes, F. Frizon and S. Lorente, Cement-Based Materials for Nuclear Waste Storage, New York, Springer Science+Business Media., 2013

[15] M. Ochs, D. Mallants and L. Wang, Radionuclide and Metal Soprtion on Cement and Concrete, Springer International Publishing, Switzerland, 2016, vol. 29.

[16] J. Tits and E. Wieland, Actinide Sorption by Cementitious Materials, Paul Scherrer Institut PSI Bericht Nr. 18-02, Switzerland, 2018

[17] A. Manceau, M. A. Marcus and N. Tamura, Quantitative Speciation of Heavy Metals in Soils and Sediments by Synchrotron X-ray Techniques, Rev. Mineral. Geochem., 2002, 49, 341–428.

[18] M. Hakanen and H. Ervanne, The influence of organic cement additives on radionuclide mobility, Posiva Working Report 2006-06, Finland

[19] V. S. Ramachandran, Concrete admixtures Handbook- Properties, Science, and Technology, Noyes Publications, National Research Council, Ottawa, Ontario, Canada, 1995

[20] E. Wieland, B. Lothenbach, M. A. Glaus, T. Thoenen and B. Schwyn, Influence of superplasticizers on the long-term properties of cement pastes and possible impact on radionuclide uptake in a cement-based repository for radioactive waste, Appl. Geochem., 2014, 49, 126–142.

[21] M. A. Glaus and L. R. Van Loon, A generic procedure for the assessment of the effect of concrete admixtures on the retention behaviour of cement for radionuclides: Concept and case studies, Paul Scherrer Institut, Switzerland, 2004.

[22] I. Androniuk, PhD Thesis, Ecole nationale supérieure Mines-Télécom Atlantique Bretagne Pays de la Loire, 2017

[23] R. D. Shannon, Revised effective ionic radii and systematic studies of interatomic distances in halides and chalcogenides, Acta Crystallogr. A, 1976, 32, 751–767.

[24] M. J. Keith-Roach, The speciation, stability, solubility and biodegradation of organic co-contaminant radionuclide complexes: A review, Sci. Total Environ., 2008, 396, 1–11.

[25] F. Taube, Struktur und Thermodynamik von Komplexen dreiwertiger Lanthanide/Actinide mit Mlat und deren Rückhaltung an Calciumsilikathydrat-Phasen, PhD Thesis, TU Dresden, 2019

[26] B. Lothenbach and A. Nonat, Calcium silicate hydrates: Solid and liquid phase composition, Cem. Concr. Res., 2015, 78, 57–70.

[27] U. R. Berner, Evolution of pore water chemistry during degradation of chemistry in a radioactive waste repository environment, Waste Manag., 1992, 12, 201–219.

[28] U. Berner, A Thermodynamic Description of the Evolution of Pore Water Chemistry and Uranium Speciation during the Degradation of Cement, Paul Scherrer Institut PSI Bericht Nr. 62, Würenlingen und Villigen, 1990

[29] D. Jacques and D. Mallants, Evolution of concrete pore water and solid phase composition during leaching with different types of water, NIROND-TR 2008-24 E V2, Brussels, 2011.

[30] D. Jacques, J. Perko, S. C. Seetharam and D. Mallants, A cement degradation model for evaluating the evolution of retardation factors in radionuclide leaching models, Appl. Geochem., 2014, 49, 143–158

[31] Geological Disposal. Near-field evolution status report., NDA Report no. NDA/RWMD/033, UK, 2010.

[32] D. Jacques, L. Wang and D. Mallants, Modelling chemical degradation of conccrete during leaching with rain and soil water types, Cem. Concr. Res., 2010, 40, 1306–1313.

[33] A. Atkinson, N. M. Everitt and R. Guppy, Evolution of pH in a Radwaste Repository: Experimental Simulation of Cement Leaching: Part 1, DOE/RW/89/025, UK, 1989.

[34] F. Brunet, P. Bertani, T. Charpentier, A. Nonat and J. Virlet, Application of 29-Si Homonuclear and 1-H– 29- Si Heteronuclear NMR Correlation to Structural Studies of Calcium Silicate Hydrates, J. Phys. Chem. B, 2004, 108, 15494–15502.

[35] S. Grangeon, A. Fernandez-Martinez, A. Baronnet, N. Marty, A. Poulain, E. Elkaïm, C. Roosz, S. Gaboreau, P. Henocq and F. Claret, Quantitative X-ray pair distribution function analysis of nanocrystalline calcium silicate hydrates: a contribution to the understanding of cement chemistry, J. Appl. Crystallogr., 2017, 50, 14–21.

[36] J. Rottstegge, M. Wilhelm and H. W. Spiess, Solid state NMR investigations on the role of organic admixtures on the hydration of cement pastes, Cem. Concr. Compos., 2006, 28, 417–426.

[37] A. J. Allen, J. J. Thomas and H. M. Jennings, Composition and density of nanoscale calcium–silicate–hydrate in cement, Nat. Mater., 2007, 6, 311–316.

[38] X. Cong and R. J. Kirkpatrick, 29Si and 17O NMR investigation of the structure of some crystalline calcium silicate hydrates, Adv. Cem. Based Mater., 1996, 3, 133–143.

[39] N. Lequeux, A. Morau, S. Philippot and P. Boch, Extended X-ray Absorption Fine Structure Investigation of Calcium Silicate Hydrates, J. Am. Ceram. Soc., 1999, 82, 1299–1306.

[40] I. G. Richardson, J. Skibsted, L. Black and R. J. Kirkpatrick, Characterisation of cement hydrate phases by TEM, NMR and Raman spectroscopy, Adv. Cem. Res., 2010, 22, 233–248.

[41] H. D. Megaw and C. H. Kelsey, Crystal Structure of Tobermorite, Nature, 1956, 177, 390–391.

[42] E. Bonaccorsi, S. Merlino and A. R. Kampf, The Crystal Structure of Tobermorite 14 A (Plombierite), a C-S-H Phase, J. Am. Ceram. Soc., 2005, 88, 505–512.

[43] K. Garbev, G. Beuchle, M. Bornefeld, L. Black and P. Stemmermann, Cell Dimensions and Composition of Nanocrystalline Calcium Silicate Hydrate Solid Solutions. Part 1: Synchrotron-Based X-Ray Diffraction, J. Am. Ceram. Soc., 2008, 91, 3005–3014.

[44] K. Garbev, M. Bornefeld, G. Beuchle and P. Stemmermann, Cell Dimensions and Composition of Nanocrystalline Calcium Silicate Hydrate Solid Solutions. Part 2: X-Ray and Thermogravimetry Study, J. Am. Ceram. Soc., 2008, 91, 3015–3023.

[45] R. J. Myers, S. A. Bernal, R. San Nicolas and J. L. Provis, Generalized Structural Description of Calcium–Sodium Aluminosilicate Hydrate Gels: The Cross-Linked Substituted Tobermorite Model, Langmuir, 2013, 29, 5294–5306.

[46] A. Nonat, The structure and stoichiometry of C-S-H, Cem. Concr. Res., 2004, 34, 1521–1528.

[47] H. Matsuyama and J. F. Young, in Advances in Cement Research, ICE Publishing, UK, 2000, vol. 12 (1), pp. 29–33.

[48] J. Qu, L. Zhong, Z. Li, M. Chena, Q. Zhanga, X. Liub, Effect of anion addition on the syntheses of Ca–Al layered double hydroxide via a two-step mechanochemical process, Applied Clay Science, 2016 124–125, 267–270.

[49] J. Qu, L. Sha, C. Wu and Q. Zhang, Applications of Mechanochemically Prepared Layered Double Hydroxides as Adsorbents and Catalysts: A Mini-Review, Nanomaterials, 2019, 9, 80

[50] V. Dodson, Concrete Admixtures, Springer Science+Buisiness Media, LLC, New York, 1990

[51] C. Giraudeau, J.-B. d' Espinose de Lacaillerie, Z. Souguir, A. Nonat and R. J. Flatt, Surface and Intercalation Chemistry of Polycarboxylate Copolymers in Cementitious Systems, J. Am. Ceram. Soc., 2009, 92, 2471–2488

[52] J. F. Young, A review of the mechanisms of set-retardation in portland cement pastes cotaining organic admixtures, Cem. Concr. Res., 1972, 2, 415–433.

[53] C. Nalet and A. Nonat, Retarding effect of organic molecules on tricalcium silicate hydration: relation with their adsorption on calcium silicate hydrates and their ion complexing power, Proceedings of the 14th International Congress on the Chemistry of Cement, Beijing, 2015.

[54] O. Chaudhari, J. J. Biernacki and S. Northrup, Effect of carboxylic and hydroxycarboxylic acids on cement hydration: experimental and molecular modeling study, J. Mater. Sci., 2017, 52, 13719–13735.

[55] S. J. T. Pollard, D. M. Montgomery, C. J. Sollars and R. Perry, Organic compounds in the cement-based stabilisation/solidification of hazardous mixed wastes—Mechanistic and process considerations, J. Hazard. Mater., 1991, 28, 313–327.

[56] F. Winnefeld, S. Becker, J. Pakusch and T. Götz, Effects of the molecular architecture of comb-shaped superplasticizers on their performance in cementitious systems, Cem. Concr. Compos., 2007, 29, 251–262.

[57] A. Zingg, F. Winnefeld, L. Holzer, J. Pakusch, S. Becker and L. Gauckler, Adsorption of polyelectrolytes and its influence on the rheology, zeta potential, and microstructure of various cement and hydrate phases, J. Colloid Interface Sci., 2008, 323, 301–312.

[58] D. García, M. Grivé, L. Duro, S. Brassinnes and J. de Pablo, The potential role of the degradation products of cement superplasticizers on the mobility of radionuclides, Appl. Geochem., 2018, 98, 1–9

[59] (ohne Autor), Concrete Admixtures and the Environment, Deutsche Bauchemie e.V., Frankfurt am Main, 2016.

[60] J. Tits, E. Wieland, C. J. Müller, C. Landesman and M. H. Bradbury, Strontium binding by calcium silicate hydrates, J. Colloid Interface Sci., 2006, 300, 78–87.

[61] N. D. M. Evans, Binding mechanisms of radionuclides to cement, Cem. Concr. Res., 2008, 38, 543–553.

[62] V. Häußler, S. Amayri, A. Beck, T. Platte, T. A. Stern, T. Vitova and T. Reich, Uptake of actinides by calcium silicate hydrate (C-S-H) phases, Appl. Geochem., 2018, 98, 426–434.

[63] F. T. Ewart, F. P. Glasser, G. Groves, T. Jappy, R. McCrohon, P. T. Moseley, S. Rodger and I. Richardson, Mechanisms of sorption in the near field. Task 3. Characterization of radioactive waste forms. (1985-89), Belgium, 1991.

[64] T. Stumpf, J. Tits, C. Walther, E. Wieland and T. Fanghänel, Uptake of trivalent actinides (curium(III)) by hardened cement paste: a time-resolved laser fluorescence spectroscopy study, J. Colloid Interface Sci., 2004, 276, 118–124.

[65] P. Mandaliev, R. Dähn, B. Wehrli and E. Wieland, Macro- and Microspectroscopic Study of Nd (III) Uptake Mechanisms Ain Hardened Cement Paste, Environ. Sci. Technol., 2009, 43, 8462–8468.

[66] N. Macé, E. Wieland, R. Dähn, J. Tits and A. C. Scheinost, EXAFS investigation on U(VI) immobilization in hardened cement paste: influence of experimental conditions on speciation, Radiochim. Acta, 2013, 101, 379–389.

[67] W. Hummel, U. Berner, E. Curti, F. J. Pearson and T. Thoenen, Nagra / PSI Chemical Thermodynamic Data Base 01/01, NAGRA/ PSI, Switzerland, 2002

[68] J. Tits, X. Gaona, A. Laube and E. Wieland, Influence of the redox state on the neptunium sorption under alkaline conditions: Batch sorption studies on titanium dioxide and calcium silicate hydrates, Radiochim. Acta, 2014, 102, 385-400.

[69] V. Neck and J. I. Kim, An electrostatic approach for the prediction of actinide complexation constants with inorganic ligands-application to carbonate complexes, Radiochim. Acta, 2000, 88, 815–822.

[70] M. L. Schlegel, I. Pointeau, N. Coreau and P. Reiller, Mechanism of europium retention by calcium silicate hydrates: an EXAFS study, Environ. Sci. Technol., 2004, 38, 4423–4431.

[71] P. Mandaliev, R. Dähn, J. Tits, B. Wehrli and E. Wieland, EXAFS study of Nd(III) uptake by amorphous calcium silicate hydrates (C–S–H), J. Colloid Interface Sci., 2010, 342, 1–7.

[72] P. Mandaliev, E. Wieland, R. Dähn, J. Tits, S. V. Churakov and O. Zaharko, Mechanisms of Nd(III) uptake by 11Å tobermorite and xonotlite, Appl. Geochem., 2010, 25, 763–777.

[73] X. Gaona, R. Dähn, J. Tits, A. C. Scheinost and E. Wieland, Uptake of Np(IV) by C–S–H Phases and Cement Paste: An EXAFS Study, Environ. Sci. Technol., 2011, 45, 8765–8771.

[74] J. Tits, G. Geipel and N. Macé, Determination of uranium(VI) sorbed species in calcium silicate hydrate phases: A laser-induced luminescence spectroscopy and batch sorption study, J. Colloid Interface Sci., 2011, 359, 248–256.

[75] J. Tits, C. Walther, T. Stumpf, N. Macé and E. Wieland, A luminescence line-narrowing spectroscopic study of the uranium(VI) interaction with cementitious materials and titanium dioxide, Dalton Trans., 2015, 44, 966–976.

[76] I. Pointeau, B. Piriou, M. Fedoroff, M.-G. Barthes, N. Marmier and F. Fromage, Sorption Mechanisms of Eu3+ on CSH Phases of Hydrated Cements, J. Colloid Interface Sci., 2001, 236, 252–259.

[77] Tits, T. Stump, E. Wieland and T. Fanghanel, Uptake of trivalent actinides (Cm(III)) and lanthanides (Eu(III)) by cement-type minerals: a wet chemistry and time-resolved laser fluorescence spectroscopy (TRLFS) study, Vol. IV Nucl. Energy Saf., 2003, 105.

[78] E. Wieland and L. R. Van Loon, Cementitious Near-Field Sorption Data Base for Performance Assessment of an ILW Repository in Opalinus Clay, Paul Scherrer Institut, NAGRA, Villigan, Schweiz, 2002.

[79] F. T. Ewart, F. P. Glasser, G. Groves, T. Jappy, R. McCrohon, P. T. Moseley, S. Rodger and I. Richardson, Mechanisms of sorption in the near field. Task 3. Characterization of radioactive waste forms. (1985-89), Belgium, 1991.

[80] L. Abrahamsen, T. Arnold, H. Brinkmann, N. Leys, M. Merroun, K. Mijnendonckx, H. Moll, P. Polvika, A. Sevcu, J. Small, M. Vikman and K. Wouters, A Review of Anthropogenic Organic Wastes and Their Degradation Behaviour, MIND Project, 2015.

[81] S. Larreur-Cayol, A. Bertron and G. Escadeillas, Degradation of cement-based materials by various organic acids in agro-industrial waste-waters, Cem. Concr. Res., 2011, 41, 882–892.

[82] L. De Windt, A. Bertron, S. Larreur-Cayol and G. Escadeillas, Interactions between hydrated cement paste and organic acids: Thermodynamic data and speciation modeling, Cem. Concr. Res., 2015, 69, 25–36.

[83] L. R. Van Loon and M. A. Glaus, Experimental and Theoretical Studies on Alkaline Degradation of Cellulose and its Impact on the Sorption of Radionuclides, Paul Scherrer Institut, Würenlingen und Villigen, 1998.

[84] M. H. Bradbury and L. R. Van Loon, Cementitious near-field sorption data bases for performance assessment of a L/ILW repository in a Palfris marl host rock., Paul Scherrer Institut, Würenlingen und Villigen, 1998.

[85] X. Gaona, V. Montoya, E. Colàs, M. Grivé and L. Duro, Review of the complexation of tetravalent actinides by ISA and gluconate under alkaline to hyperalkaline conditions, J. Contam. Hydrol., 2008, 102, 217–227.

[86] E. Wieland, M. H. Bradbury and L. Van Loon, Development of a sorption data base for the cementitious near-field of a repository for radioactive waste, Czechoslov. J. Phys., 2003, 53, A629–A638.

[87] L. R. Van Loon, M. A. Glaus, S. Stallone and A. Laube, Sorption of isosaccharinic acid, a cellulose degradation product, on cement, Environ. Sci. Technol., 1997, 31, 1243–1245.

[88] K. Vercammen, M. A. Glaus and L. R. Van Loon, Evidence for the Existence of Complexes between Th(IV) and alpha-Isosaccharinic Acid under Alkaline Conditions, Radiochim. Acta, 1999, 84, 221–224.

[89] D. Rai, N. J. Hess, Y. Xia, L. Rao, H. M. Cho, R. C. Moore and L. R. Van Loon, Comprehensive thermodynamic model applicable to highly acidic to basic conditions for isosaccharinate reactions with Ca (II) and Np (IV), J. Solut. Chem., 2003, 32, 665–689.

[90] D. Rai, M. Yui, D. A. Moore and L. Rao, Thermodynamic Model for ThO2(am) Solubility in Isosaccharinate Solutions, J. Solut. Chem., 2009, 38, 1573–1587.

[91] P. Warwick, N. Evans and S. Vines, Studies on some divalent metal alpha-isosaccharinic acid complexes, Radiochim. Acta, 2006, 94, 363– 368.

[92] J. Tits, E. Wieland and M. H. Bradbury, The effect of isosaccharinic acid and gluconic acid on the retention of Eu(III), Am(III) and Th(IV) by calcite, Appl. Geochem., 2005, 20, 2082–2096.

[93] E. Wieland, A. Jakob, J. Tits, B. Lothenbach and D. Kunz, Sorption and diffusion studies with low molecular weight organic compounds in cementitious systems, Appl. Geochem., 2016, 67, 101–117.

[94] A. Kitamura, K. Fujiwara, M. Mihara, M.Cowper and G.Kamei, Thorium and americium solubilities in cement pore water containing superplasticiser compared with thermodynamic calculations, J. of Radioanal. and Nuclear Chemistry, 2013, 298, 485–493.

[95] A. Courdouan, I. Christl, S. Meylan, P. Wersin and R. Kretzschmar, Isolation and characterization of dissolved organic matter from the Callovo–Oxfordian formation, Appl. Geochem., 2007, 22, 1537–1548.

[96] A. Courdouan, I. Christl, S. Meylan, P. Wersin and R. Kretzschmar, Characterization of dissolved organic matter in anoxic rock extracts and in situ pore water of the Opalinus Clay, Appl. Geochem., 2007, 22, 2926–2939.

[97] A. Courdouan, I. Christl, T. Rabung, P. Wersin and R. Kretzschmar, Proton and Trivalent Metal Cation Binding by Dissolved Organic Matter in the Opalinus Clay and the Callovo-Oxfordian Formation, Environ. Sci. Technol., 2008, 42, 5985–5991.

[98] K. Hänninen and K. Niemelä, Alkaline degradation of Peat Humic Acids. Part II. Identification of hydrophilic products., Acta Chem. Scand., 1992, 46, 459– 463.

[99] K. Kawamura and I. R. Kaplan, Dicarboxylic acids generated by thermal alteration of kerogen and humic acids, Geochim. Cosmochim. Acta, 1987, 51, 3201–3207.

[100] C. H. Gammons and S. A. Wood, The aqueous geochemistry of REE. Part 8: Solubility of ytterbium oxalate and the stability of Yb(III)-oxalate complexes in water at 25°C to 80°C, Chem. Geol., 2000, 166, 103–124.

[101] P. Hoth, Endlagerung radioaktiver Abfälle in Deutschland, Bundesanstalt für Geowissenschaften und Rohstoffe, Hannover/ Berlin, 2007.

[102] W. Hummel, G. Anderegg, I. Puigdomènech, L. Rao and O. Tochiyama, Chemical Thermodynamics, Chemical thermodynamics of compounds and complexes of U, Np, Pu, Am, Tc, Se, Ni, and Zr with selected organic ligands, OECD, NEA-TDB, North Holland: Amsterdam, 2005.

[103] R. Prados, L. G. Stadtherr, H. Donato Jr and R. B. Martin, Lanthanide complexes of amino acids, J. Inorg. Nucl. Chem., 1974, 36, 689–693.

[104] H. G. Brittain and F. S. Richardson, pH Dependence of circularly polarized emission and total emission from europium (III)/L-malic acid and europium (III)/L-malic acid/terbium (III) complexes in water and water-d2 solutions, Inorg. Chem., 1976, 15, 1507–1511.

[105] H. G. Brittain, Stereoselectivity in the transfer from Terbium(III) to europium(III) complexes of malic acid, J. Inorg. Nucl. Chem., 1979, 41, 721–724.

[106] S. A. Ali, N. A. Dobrynina, L. I. Martynenko and V. I. Spitsyn, Spectrographic investigation of neodymium malates in aqueous solutions, Russ. Chem. Bull., 1980, 29, 1022–1025.

[107] M. Cefola, A. S. Tompa, A. V. Celiano and P. S. Gentile, Coordination Compounds. 11. Trends in the Stability of Some Rare Earth Chelates, Inorg. Chem., 1962, 1, 290–293.

[108] S. R. Sushrutha and S. Natarajan, Rare-earth carboxylates, $[Ln_2(III)(\mu 3\text{-}OH)(C_4H4O_5)_2(C_4H_2O_4)]\cdot 2H_2O$ [Ln = Ce, Pr and Nd]: synthesis, structure and properties, CrystEngComm, 2014, 16, 4774–4782.

[109] B. Weaver and F. A. Kappelmann, TALSPEAK: A new method of separating americium and curium from the lanthanides by extraction from an aqueous solution of an aminopolyacetic acid complex with a monoacidic organophosphate or phosphonate, Oak Ridge National Lab., Tenn., 1964.

[110] A. Barkleit, J. Kretzschmar, S. Tsushima and M. Acker, Americium(III) and Europium(III) Complex Formation with Lactate at Elevated Temperatures Studied by Spectroscopy and Quantum Chemical Calculations, Dalton Trans., 2014, 43, 11221–11232.

[111] G. R. Choppin and J. A. Chopoorian, Complexes of the lanthanide elements with α-hydroxy carboxylate ligands, J. Inorg. Nucl. Chem., 1961, 22, 97–113.

[112] H. Deelstra and F. Verbeek, The determination of the stability constants of the lanthanide α-hydroxyisobutyrate and lactate complexes by potentiometric titration, Anal. Chim. Acta, 1964, 31, 251–257.

[113] A. Aziz and S. J. Lyle, Americium(III) and europium(III) complexes with lactate, pyruvate and α-alaninate in aqueous solutions—A comparison of equilibrium constants, J. Inorg. Nucl. Chem., 1971, 33, 3407–3408.

[114] K. Bukietynska, A. Mondry and E. Osmęda, Application of the Oscillation Strength of 'Hypersensitive' Transitions to the investigation of Complex Equilibria of Lanhtanide Ions - I, J Inorg Nucl Chem, 1981, 43, 1311–1319.

[115] P. R. Danesi, C. Cianetti and E. P. Horwitz, Distribution Equilibria of Eu(III) in the System: Bis(2-ethylhexyl)phosphoric Acid, Organic Diluent—NaCl, Lactic Acid, Polyaminocarboxylic Acid, Water, Sep. Sci. Technol., 1982, 17, 507–519.

[116] R. Lundqvist, J. F. Lu and I. Svantesson, Hydrophilic complexes of the actinides. 3. Lactates of Am(III), Eu(III), U(IV) and UO2(II), Acta Chem. Scand Phys Inorg Chem, 1984, 38, 501–512.

[117] G. Tian, L. R. Martin and L. Rao, Complexation of Lactate with Neodymium(III) and Europium(III) at Variable Temperatures: Studies by Potentiometry, Microcalorimetry, Optical Absorption, and Luminescence Spectroscopy, Inorg. Chem., 2010, 49, 10598–10605.

[118] B. Kienzler, Geochemische begründete Eingangsparameter für Kritikalitätsuntersuchungen, Karlsruhe, 2003.

[119] D. R. Froehlich, A. Skerencak-Frech, U. Kaplan, C. Koke, A. Rossberg and P. J. Panak, An EXAFS spectroscopic study of Am(III) complexation with lactate, J. Synchrotron Radiat., 2015, 22, 1469–1474.

[120] L. De Almeida, S. Grandjean, N. Vigier and F. Patisson, Insights into the Thermal Decomposition of Lanthanide(III) and Actinide(III) Oxalates - from Neodymium and Cerium to Plutonium, Eur. J. Inorg. Chem., 2012, 31, 4986–4999.

[121] B. A. Crawford, S. A. Lott, L. D. Sparks, G. Van Soest and B. McInroy, Tuscon, Arizona, 2006.

[122] P. Thakur, J. N. Mathur, C. J. Dodge, A. J. Francis and G. R. Choppin, Thermodynamics and the structural aspects of the ternary complexes of Am(III), Cm(III) and Eu(III) with Ox and EDTA + Ox, Dalton Trans., 2006, 4829–4837.

[123] A. Skerencak-Frech, M. Maiwald, M. Trumm, D. R. Froehlich and P. J. Panak, The Complexation of Cm(III) with Oxalate in Aqueous Solution at T = 20–90 °C: A Combined TRLFS and Quantum Chemical Study, Inorg. Chem., 2015, 54, 1860–1868.

[124] D. R. Foehlich, M. M. Maiwald, F. Taube, J. Plank and P. J. Panak, A thermodynamical and structural study on the complexation of trivalent lanthanides with a polycarboxylate based concrete superplasticizer, Dalton Transaction, 2017, 46, 4093-4100.

[125] D. R. Foehlich, C. Koke, M. M. Maiwald, C. Chomy, J. Plank and P. J. Panak, A spectroscopic study of the complexation reaction of trivalent lanthanides with a synthetic acrylate based PCE-superplasticizer, Spectrochim. Acta Part A: molecular and Biomolecular Spectroscopy, 2019, 207, 270-275.

[126] D. R. Froehlich and P. J. Panak, The complexation of Eu(III) and Cm(III) with polyacrylate as a model compound for complex polycarboxylates studied by laser fluorescence spectroscopy, J. of Luminescence, 2019, 212, 166-170.

[127] M. Altmaier, V. Metz, V. Netz, R. Müller and T. Fanghänel, Solid-liquid equilibria of Mg(OH)2(cr) and Mg2(OH)3Cl·4H2O(cr) in the system Mg-Na-H-OH-Cl-H2O at 25°C, Geochim. Cosmochim. Acta, 2003, 67, 3595–3601.

[128] X. Gaona, D. Fellhauer and M. Altmaier, Thermodynamic description of Np(VI) solubility, hydrolysis, and redox behavior in dilute to concentrated alkaline NaCl solutions, Pure Appl. Chem., 2013, 85, 2027–2049.

[129] J. Tits, M. Bradbury, P. Eckert, A. Schaible and E. Wieland, The Uptake of Eu(III) and Th(IV) by Calcite under Hyperalkaline Conditions: The Influence of Gluconic and Isosaccharinic Acid, Paul Scherrer Institut, Switzerland, 2002.

[130] T. Stumpf, H. Curtius, C. Walther, K. Dardenne, K. Ufer and T. Fanghänel, Incorporation of Eu(III) into Hydrotalcite: A TRLFS and EXAFS Study, Environ. Sci. Technol., 2007, 41, 3186–3191.

[131] M. A. Denecke, Synchrotron applications to f-element research in the nuclear fuel cycle, Dalton Trans., 2015, 44, 2606–2612.

[132] T. Stumpf, M. Marques Fernandes, C. Walther, K. Dardenne and T. Fanghänel, Structural characterization of Am incorporated into calcite: A TRLFS and EXAFS study, J. Colloid Interface Sci., 2006, 302, 240–245.

[133] T. Reich, G. Bernhard, G. Geipel, H. Funke, C. Hennig, A. Rossberg, W. Matz, N. Schell and H. Nitsche, The Rossendorf Beam Line ROBL – a dedicated experimental station for XAFS measurements of actinides and other radionuclides, Radiochim. Acta, 2000, 88, 633–637.

[134] K. Holliday, S. Handley-Sidhu, K. Dardenne, J. Renshaw, L. Macaskie, C. Walther and T. Stumpf, A New Incorporation Mechanism for Trivalent Actinides into Bioapatite: A TRLFS and EXAFS Study, Langmuir, 2012, 28, 3845–3851.

[135] C. Hennig, S. Takao, K. Takao, S. Weiss, W. Kraus, F. Emmerling, M. Meyer and A. C. Scheinost, Identification of hexanuclear Actinide(IV) carboxylates with Thorium, Uranium and Neptunium by EXAFS spectroscopy, J. Phys. Conf. Ser., 2013, 430, 012116.

[136] M. G. Ferrier, B. W. Stein, S. E. Bone, S. K. Cary, A. S. Ditter, S. A. Kozimor, J. S. Lezama Pacheco, V. Mocko and G. T. Seidler, The coordination chemistry of CmIII , AmIII , and AcIII in nitrate solutions: an actinide L 3-edge EXAFS study, Chem. Sci., 2018, 9, 7078–7090.

[137] M. G. Ferrier, B. W. Stein, S. E. Bone, S. K. Cary, A. S. Ditter, S. A. Kozimor, J. S. Lezama Pacheco, V. Mocko and G. T. Seidler, The coordination chemistry of CmIII , AmIII , and AcIII in nitrate solutions: an actinide L 3-edge EXAFS study, Chem. Sci., 2018, 9, 7078–7090.

[138] A. Bhattacharyya, A. Leoncini, R. J. M. Egberink, P. K. Mohapatra, P. K. Verma, A. S. Kanekar, A. K. Yadav, S. N. Jha, D. Bhattacharyya, J. Huskens and W. Verboom, First Report on the Complexation of Actinides and Lanthanides Using 2,2′,2″-(((1,4,7-Triazonane-1,4,7-triyl)tris(2-oxoethane-2,1-diyl)) tris(oxy)) tris(N , N -dioctylacetamide): Synthesis, Extraction, Luminescence, EXAFS, and DFT Studies, Inorg. Chem., 2018, 57, 12987–12998.

[139] F. Taube, A. Rossberg, K. Kammerlander, M. Acker, T. Stumpf et. al., A spectroscopic study of the An(III)/Ln(III) uptake by calcium silicate hydrates under the influence of malate, in preparation, to be published in 2020

[140] G. N. George and I. J. Pickering, EXAFSPAK: A Suite of Computer Programs for Analysis of X-Ray Absorption Spectra, Stanf. Synchrotron Radiat. Lab. CA US

[141] A. L. Ankudinov, B. Ravel, J. J. Rehr and S. D. Conradson, Real-space multiple-scattering calculation and interpretation of x-ray-absorption near-edge structure, Phys. Rev. B, 1998, 58, 7565.

[142] S. Merlino, E. Bonaccorsi and T. Armbruster, The real structure of tobermorite 11A: normal and anomalous forms, OD character and polytypic modifications, Eur. J. Mineral., 2001, 13, 577–590

[143] W. Horrocks and D. R. Sudnick, Lanthanide Ion Probes of Structure in Biology. Laser-Induced Luminescence Decay Constants Provide a Direct Measure of the Number of Metal-Coordinated Water Molecules, J. Am. Chem. Soc., 1979, 101, 333–340.

[144] T. Kimura and G. R. Choppin, Luminescence study on determination of the hydration number of Cm(III), J. Alloys Compd., 1994, 213-214, 313–317.

[145] Kimura and Y. Kato, Luminescence study on determination of the inner-sphere hydration number of Am(III) and Nd(III), J. Alloys Compd., 1998, 271–273, 867–871.

[146] C. A. Andersson and R. Bro, The N-way Toolbox for MATLAB, Chemom. Intell. Lab. Syst., 2000, 52, 1–4.

[147] R. Bro, PARAFAC. Tutorial and applications, Chemom. Intell. Lab. Syst., 1997, 38, 149–171.

[148] T. Saito, H. Sao, K. Ishida, N. Aoyagi, T. Kimura, S. Nagasaki and S. Tanaka, Application of Parallel Factor Analysis for Time-Resolved Laser Fluorescence Spectroscopy: Implication for Metal Speciation Study, Environ. Sci. Technol., 2010, 44, 5055–5060.

[149] B. Drobot, R. Steudtner, J. Raff, G. Geipel, V. Brendler and S. Tsushima, Combining luminescence spectroscopy, parallel factor analysis and quantum chemistry to reveal metal speciation – a case study of Uranyl(VI) hydrolysis, Chem Sci, 2015, 6, 964–972.

[150] J. Schott, J. Kretzschmar, M. Acker, S. Eidner, M. U. Kumke, B. Drobot, A. Barkleit, S. Taut, V. Brendler and T. Stumpf, Formation of a Eu(III) borate solid species from a weak Eu(III) borate complex in aqueous solution, Dalton Trans, 2014, 43, 11516–11528.

[151] B. Drobot, A. Bauer, R. Steudtner, S. Tsushima, F. Bok, M. Patzschke, J. Raff and V. Brendler, Speciation Studies of Metals in Trace Concentrations: The Mononuclear Uranyl(VI) Hydroxo Complexes, Anal. Chem., 2016, 88, 3548–3555.

[152] M. Bader, K. Müller, H. Foerstendorf, B. Drobot, M. Schmidt, N. Musat, J. S. Swanson, D. T. Reed, T. Stumpf and A. Cherkouk, Multistage bioassociation of uranium onto an extremely halophilic archaeon revealed by a unique combination of spectroscopic and microscopic techniques, J. Hazard. Mater., 2017, 327, 225–232.

[153] P. Gans, A. Sabatini and A. Vacca, Simultaneous Calculation of Equilibrium Constants and Standard Formation Enthalpies from Calorimetric Data for Systems with Multiple Equilibria in Solution, J. Solut. Chem., 2008, 37, 467–476.

[154] L. D. Hansen, G. W. Fellingham and D. J. Russell, Simultaneous determination of equilibrium constants and enthalpy changes by titration calorimetry: Methods, instruments, and uncertainties, Anal. Biochem., 2011, 409, 220–229.

[155] Origin, OriginLab, Version8.6 Corporation, Northampton, USA.

[156] S. Keller, C. Vargas, H. Zhao, G. Piszczek, C. A. Brautigam and P. Schuck, High-Precision Isothermal Titration Calorimetry with Automated Peak-Shape Analysis, Anal. Chem., 2012, 84, 5066–5073.

[157] T. H. Scheuermann and C. A. Brautigam, High-precision, automated integration of multiple isothermal titration calorimetric thermograms: New features of NITPIC, Methods, 2015, 76, 87–98.

[158] V. H. Le, R. Buscaglia, J. B. Chaires and E. A. Lewis, Modeling complex equilibria in isothermal titration calorimetry experiments: Thermodynamic parameters estimation for a three-binding-site model, Anal. Biochem., 2013, 434, 233–241.

[159] H. Zhao, G. Piszczek and P. Schuck, SEDPHAT – A platform for global ITC analysis and global multi-method analysis of molecular interactions, Methods, 2015, 76, 137-148.

[160] D. Massiot, F. Fayon, M. Capron, I. King, S. Le Calvé, B. Alonso, J.-O. Durand, B. Bujoli, Z. Gan and G. Hoatson, Modelling one-and two-dimensional solid-state NMR spectra, Magn. Reson. Chem., 2002, 40, 70–76.

[161] E. L'Hôpital, B. Lothenbach, G. Le Saout, D. Kulik and K. Scrivener, Incorporation of aluminium in calcium-silicate-hydrates, Cem. Concr. Res., 2015, 75, 91–103.

[162] B. Lothenbach, D. Nied, E. L'Hôpital, G. Achiedo and A. Dauzères, Magnesium and calcium silicate hydrates, Cem. Concr. Res., 2015, 77, 60–68.

[163] TURBOMOLE V6.4 2012. A Development of University of Karlsruhe and Forschungszentrum Karlsruhe GmbH, TURBOMOLE GmbH, since 2007. Available at http://www.turbomole.com, 1989

[164] S. Nosé, A unified formulation of the constant temperature molecular dynamics methods, J. Chem. Phys., 1984, 81, 511–519.

[165] X. Cao and M. Dolg, Segmented contraction scheme for small-core lanthanide pseudopotential basis sets, J. Mol. Struct. THEOCHEM, 2002, 581, 139–147.

[166] M. Dolg, H. Stoll, A. Savin and H. Preuss, Energy-adjusted pseudopotentials for the rare earth elements, Theor. Chem. Acc. Theory Comput. Model. Theor. Chim. Acta, 1989, 75, 173–194.

[167] J. P. Perdew, Density-functional approximation for the correlation energy of the inhomogeneous electron gas, Phys. Rev. B, 1986, 33, 8822.

[168] A. D. Becke, Density-functional exchange-energy approximation with correct asymptotic behavior, Phys. Rev. A, 1988, 38, 3098–3100.

[169] J. Aupiais, L. Bonin, C. Den Auwer, P. Moisy, B. Siberchicot and S. Topin, On the use of speciation techniques and ab initio modelling to understand tetravalent actinide behavior in a biological medium: An(IV) DTPA case, Dalton Trans., 2016, 45, 3759–3770.

[170] L. Léost, J. Roques, A. Van Der Meeren, L. Vincent, N. Sbirrazzuoli, C. Hennig, A. Rossberg, J. Aupiais, S. Pagnotta, C. Den Auwer and C. Di Giorgio, Towards the development of chitosan nanoparticles for plutonium pulmonary decorporation, Dalton Trans., 2018, 47, 11605–11618.

[171] F. Lahrouch, A. C. Chamayou, G. Creff, M. Duvail, C. Hennig, M. J. Lozano Rodriguez, C. Den Auwer and C. Di Giorgio, A Combined Spectroscopic/Molecular Dynamic Study for Investigating a Methyl-Carboxylated PEI as a Potential Uranium Decorporation Agent, Inorg. Chem., 2017, 56, 1300–1308.

[172] C. Lucks, A. Rossberg, S. Tsushima, H. Foerstendorf, A. C. Scheinost and G. Bernhard, Aqueous Uranium(VI) Complexes with Acetic and Succinic Acid: Speciation and Structure Revisited, Inorg. Chem., 2012, 51, 12288–12300.

[173] M. Acker, J. Schott, F. Taube, A. Barkleit, M. Müller, S. Taut and T. Stumpf, Spectroscopic and thermodynamic studies on the interaction of An(III) and Ln(III) with complexing ligands in saline media, in Final Report of the BMWi Joint research project: Retention of Radionuclides relevant for final disposal in natural clay rock and saline system, KIT scientific report 2017

[174] P. R. Zalupski, K. L. Nash and L. R. Martin, Thermodynamic Features of the Complexation of Neodymium(III) and Americium(III) by Lactate in Trifluoromethanesulfonate Media, J. Solut. Chem., 2010, 39, 1213–1229.

[175] R. J. Motekaitis, NIST Standard Reference Database 46 vers. 8 – NIST critically selected constants of metal complexes, US Dep. Commer. Wash. DC.

[176] T. Keleti, Errors in the evaluation of Arrhenius and van't Hoff plots, Biochem. J., 1983, 209, 277–280.

[177] I. Jelesarov and H. R. Bosshard, Isothermal titration calorimetry and differential scanning calorimetry as complementary tools to investigate the energetics of biomolecular recognition, J. Mol. Recognit., 1999, 12, 3–18.

[178] L. Rao, Thermodynamics of actinide complexation in solution at elevated temperatures: application of variable-temperature titration calorimetry, Chem. Soc. Rev., 2007, 36, 881.

[179] A. DeRobertis, C. DeStefano and C. Foti, Medium Effects on the Protonation of Carboxylic Acids at Different Temperatures, J. Chem. Eng. Data, 1999, 44, 262–270.

[180] L. Ciavatta, The specific interaction theory in evaluating ionic equilibria, Ann Chim, 1980, 70, 551–567.

[181] L. D. Pettit and K. J. Powell, The IUPAC Stability Constants Database, release 5, IUPAC Academic Software: Otley, U.K., 2005.

[182] D. R. Froehlich, M. Trumm, A. Skerencak-Frech and P. J. Panak, The Complexation of Cm(III) with Succinate Studied by Time-Resolved Laser Fluorescence Spectroscopy and Quantum Chemical Calculations, Inorg. Chem., 2016, 55, 4504–4511.

[183] L. Ciavatta, The specific interaction theory in equilibrium analysis: Some empirical rules for estimating interaction coefficients of metal ion complexes, Ann Chim Roma, 1990, 80, 255– 263

[184] C. De Stefano, C. Foti, O. Giuffrè and S. Sammartano, Dependence on Ionic Strength of Protonation Enthalpies of Polycarboxylate Anions in NaCl Aqueous Solution, J. Chem. Eng. Data, 2001, 46, 1417–1424.

[185] A. Skerencak-Frech, F. Taube, P. L. Zanonato, M. Acker, P. J. Panak and P. Di Bernardo, A Potentiometric and Microcalorimetric Study of the Complexation of Trivalent Europium with Lactate: The Ionic Strength Dependency of log β'n, ΔrHm,n and ΔrSm,n., Thermochim. Acta, 2019, 679, 178316.

[186] F. Taube, B. Drobot, A. Rossberg, H. Foerstendorf, M. Acker, M. Patzschke, M. Trumm, S. Taut and T. Stumpf, Thermodynamic and Structural Studies on the Ln(III)/An(III) Malate Complexation, Inorg. Chem., 2019, 58, 368–381.

[187] A. Heller, A. Barkleit, H. Foerstendorf, S. Tsushima, K. Heim and G. Bernhard, Curium(III) citrate speciation in biological systems: a Europium(III) assisted spectroscopic and quantum chemical study, Dalton Trans., 2012, 41, 13969–13983.

[188] D. R. Froehlich, A. Skerencak-Frech, M.-L. K. Morkos and P. J. Panak, A spectroscopic study of Cm(III) complexation with propionate in saline solutions at variable temperatures, New J. Chem., 2013, 37, 1520.

[189] D. R. Froehlich, A. Skerencak-Frech, M.-L. K. Morkos and P. J. Panak: A spectroscopic study on the Formation of Cm(III) complexes a Elevated Temperature, Dalton Trans., 2014, 43, 3958.

[190] R. J. Silva, G. Bidolio, M. H. Rand, P. B. Robouch, H. Wenner, I. Puigdomenech, Chemical Thermodynamics of Americium, OECD nuclear Energy Agency Data, North Holland Elsevier Science Publishers B. V., Amsterdam, 1995.

[191] G. Montavon, M. Bouby, S. Huclier-Markai, B. Grambow, H. Geckeis, T. Rabung, I. Pashalidis, B. Amekraz, C. Moulin, Quantitative description and local struktures of trivalent metal ions Eu(III) and Cm(III) complexed with polyacrylic acid, J. of Colloid and Interface Science, 2008, 327, 324-332.

[192] R. Hahn, C. Hein, J. M. Sander, R. Kautenburger, Complexation of europium and uranium with natural organic matter (NOM) in highly saline water matrices analysed by ultrafiltration and inductively coupled plasma mass spectrometry (ICP-MS), Applied Geochemistry, 2017, 78, 241-249.

[193] H. Lippold, M. Becker, Complexation of Eu(III) with a polymeric cement additive as a potential carrier of actinides, Annual Report, Institute of Resource Ecology, Helmholtz-Zentrum Dresden-Rossendorf, 2016, 33

[194] J. I. Kim and K. R. Czerwinski, Complexation of metal ions with humic acid: metal ion charge neutralization model, Radiochim. Acta, 1996, 73, 5-10.

[195] S. A. Cotton, Lanthanide and Actinide Chemistry, John Wiley & Sons, Ltd, Uppingham School, Uppingham, Rutland, UK, 2006.

[196] K. B. Yatsimirskii and N. K. Davidenko, Absorption spectra and structure of lanthanide coordination compounds in solution, Coord. Chem. Rev., 1979, 27, 223–273.

[197] I. V. Sukhno, V. Y. Buzko, V. T. Panushkin and M. B. Gavriluk, Different Complexation of Nd3+ and Sm3+ with L-Malic Acid, Russ. J. Coord. Chem., 2004, 30, 591–598.

[198] S. A. Ali, N. A. Dobrynina, L. I. Martynenko and A. P. Borisova, Mixed complexes Formed by the Lanthanides with Nitrilotriacetic and Malic Acids, Russ. J. Inorg. Chem., 1980, 25, 1781–1783.

[199] H. Kitano, Y. Onishi, A. Kirishima, N. Sato and O. Tochiyama, Determination of the thermodynamic quantities of complexation between Eu(III) and carboxylic acids by microcalorimetry, Radiochim. Acta, 2006, 94, 541–547.

[200] M. A. Brown, A. J. Kropf, A. Paulenova and A. V. Gelis, Aqueous complexation of citrate with neodymium(III) and americium(III): a study by potentiometry, absorption spectrophotometry, microcalorimetry, and XAFS, Dalton Trans., 2014, 43, 6446.

[201] X.-Y. Chen, G. S. Goff, W. C. Ewing, B. L. Scott and W. Runde, Solid-State and Solution-State Coordination Chemistry of Lanthanide(III) Complexes with α-Hydroxyisobutyric Acid, Inorg. Chem., 2012, 51, 13254–13263.

[202] D. M. Roitershtein, A. A. Vinogradov, K. A. Lyssenko and I. E. Nifant'ev, Self-assembly of heteroleptic tetranuclear carboxylate complexes of yttrium and lanthanides during hydrolysis and oxidation of rare earth homoleptic carboxylates, Inorg. Chem. Commun., 2017, 84, 225–228.

[203] C. M. Andolina, R. A. Mathews and J. R. Morrow, Solution chemistry of europium (III) aqua ion at micromolar concentrations as probed by direct excitation luminescence spectroscopy, Helv. Chim. Acta, 2009, 92, 2330–2348.

[204] S. Kuke, B. Marmodée, S. Eidner, U. Schilde and M. U. Kumke, Intramolecular deactivation processes in complexes of salicylic acid or glycolic acid with Eu(III), Spectrochim. Acta. A. Mol. Biomol. Spectrosc., 2010, 75, 1333–1340.

[205] T. Kimura, Luminescence study on Solvation of americium(III), curium(III) and several lanthanide(III) ions in nonaqueous and binary mixed solvents, Radiochim. Acta, 2001, 89, 125–130.

[206] G. R. Choppin and D. R. Peterman, Applications of lanthanide luminescence spectroscopy to solution studies of coordination chemistry, Coord. Chem. Rev., 1998, 174, 283–299.

[207] J. I. Kim, R. Klenze, H. Wimmer, W. Runde and W. Hauser, A study of the carbonate complexation of Cm(III) and Eu(III) by time-resolved laser fluorescence spectroscopy, J. Alloys Compd., 1994, 213/214, 333–340.

[208] J.-C. G. Bünzli and G. R. Choppin, Lanthanide Probes in Life, Chemical and Earth Sciences- Theory and Practice, Elsevier, Amsterdam, 1989.

[209] M. Kakihana, T. Nagumo, M. Okamoto and H. Kakihana, Coordination structures for uranyl carboxylate complexes in aqueous solution studied by IR and carbon-13 NMR spectra, J. Phys. Chem., 1987, 91, 6128–6136.

[210] J. Kuduk-Jaworska and K. Waszkiewicz, Malatoplatinum (II) complexes–carboplatin analogs, Transit. Met. Chem., 2000, 25, 443–449.

[211] G. B. Deacon and R. J. Phillips, Relationships between the carbon-oxygen stretching frequencies of carboxylato complexes and the type of carboxylate coordination, Coord. Chem. Rev., 1980, 33, 227–250.

[212] A. Rossberg, T. Reich and G. Bernhard, Complexation of Uranium(VI) with protocatechuic acid - application of iterative transformation factor analysis to EXAFS spectroscopy, Anal. Bioanal. Chem., 2003, 376, 631–638.

[213] D. R. Froehlich, A. Skerencak-Frech, N. Bauer, A. Rossberg and P. J. Panak, The pH dependence of Am(III) complexation with acetate: an EXAFS study, J. Synchrotron Radiat., 2015, 22, 99–104.

[214] D. R. Froehlich, A. Kremleva, A. Rossberg, A. Skerencak-Frech, C. Koke, S. Krueger, N. Roesch and P. J. Panak, Combined EXAFS Spectroscopic and Quantum Chemical Study on the Complex Formation of Am(III) with Formate, Inorg. Chem., 2017, 56, 6820–6829.

[215] B. A. Roscoe and P. K. Hopke, Error estimates for factor loadings and scores obtained with target transformation factor analysis, Anal. Chim. Acta, 1981, 132, 89–97.

[216] B. A. Roscoe and P. K. Hopke, Error estimates for factor loadings and scores obtained by target transformation factor analysis: A Clarification, Anal. Chim. Acta, 1982, 135, 379–380.

[217] K. E. Knope and L. Soderholm, Solution and Solid-State Structural Chemistry of Actinide Hydrates and Their Hydrolysis and Condensation Products, Chem. Rev., 2013, 113, 944–994.

[218] W. Runde, Spectroscopies for Environmental Studies of Actinide Species, Los Alamos Sci., 2000, 26, 412–415.

[219] M. Riri, M. Hor, F. Serdaoui and M. Hlaibi, Complexation of trivalent lanthanide cations by different chelation sites of malic and tartric acid (Composition, Stability and probable structure), Arab. J. Chem., 2016, 9, S1478–S1486.

[220] D. K. Unruh, K. Gojdas, E. Flores, A. Libo and T. Z. Forbes, Synthesis and Structural Characterization of Hydrolysis Products within the Uranyl Iminodiacetate and Malate Systems, Inorg. Chem., 2013, 52, 10191–10198.

[221] R.-H. Zhang, Q.-M. Hong, J.-M. Yang, H.-L. Zhang, G. Michael Blackburnb and Z.-H. Zhou, Syntheses, spectroscopies and structures of zinc complexes with malate, Inorganica Chim. Acta, 2009, 362, 2643–2649.

[222] R. F. D'Vries, I. Camps and J. Ellena, Exploring the System Lanthanide/Succinate in the Formation of Porous Metal–Organic Frameworks: Experimental and Theoretical Study, Cryst. Growth Des., 2015, 15, 3015–3023.

[223] R. C. Reynolds, The effect of particle size on apparent lattice spacings, Acta Crystallogr. A, 1968, 24, 319–320.

[224] E. L'Hôpital, B. Lothenbach, K. Scrivener and D. A. Kulik, Alkali uptake in calcium alumina silicate hydrate (C-A-S-H), Cem. Concr. Res., 2016, 85, 122–136.

[225] B. Lothenbach, P. Durdzinski and K. De Weerdt, in A practical guide to microstructural analysis of cementitious materials, CRC press Boca Raton, FL, 2016, pp. 177–212.

[226] T. Mitsuda and H. F. W. Taylor, Normal and anomalous tobermorites, Mineral. Mag., 1978, 42, 229–235.

[227] R. J. Myers, E. L'Hôpital, J. L. Provis and B. Lothenbach, Effect of temperature and aluminium on calcium (alumino)silicate hydrate chemistry under equilibrium conditions, Cem. Concr. Res., 2015, 68, 83–93.

[228] V. Morales-Florez, N. Findling and F. Brunet, Changes on the nanostructure of cementitius calcium silicate hydrates (C–S–H) induced by aqueous carbonation, J. Mater. Sci., 2012, 47, 764–771.

[229] S. Monkman, P. A. Kenward, G. Dipple, M. MacDonald and M. Raudsepp, Activation of cement hydration with carbon dioxide, J. Sustain. Cem.-Based Mater., 2018, 7, 160–181.

[230] X. Pardal, F. Brunet, T. Charpentier, I. Pochard and A. Nonat, 27Al and 29Si Solid-State NMR Characterization of Calcium-Aluminosilicate-Hydrate, Inorg. Chem., 2012, 51, 1827–1836.

[231] C. A. Orozco, B. W. Chun, G. Geng, A. H. Emwas and P. J. M. Monteiro, Characterization of the Bonds Developed between Calcium Silicate Hydrate and Polycarboxylate-Based Superplasticizers with Silyl Functionalities, Langmuir, 2017, 33, 3404–3412.

[232] X. Qu, Z. Zhao and X. Zhao, Microstructure and characterization of aluminum-incorporated calcium silicate hydrates (C–S–H) under hydrothermal conditions, RSC Adv., 2018, 8, 28198–28208.

[233] X. Cong and R. J. Kirkpatrick, 29Si MAS NMR Study of the Structure of Calcium Silicate Hydrate, Adv. Cem. Based Mater., 1996, 3, 144–156.

[234] A. Barkleit, G. Geipel, M. Acker, S. Taut and G. Bernhard, First fluorescence spectroscopic investigation of Am(III) complexation with an organic carboxylic ligand, pyromellitic acid, Spectrochim. Acta. A. Mol. Biomol. Spectrosc., 2011, 78, 549–552.

[235] B. Raditzky, S. Sachs, K. Schmeide, A. Barkleit, G. Geipel and G. Bernhard, Spectroscopic study of americium(III) complexes with nitrogen containing organic model ligands, Polyhedron, 2013, 65, 244–251.

[236] N. Huittinen, A. C. Scheinost, Y. Ji, P. M. Kowalski, Y. Arinicheva, A. Wilden, S. Neumeier and T. Stumpf, A Spectroscopic and Computational Study of Cm^{3+} Incorporation in Lanthanide Phosphate Rhabdophane ($LnPO_4{\cdot}0.67\ H_2O$) and Monazite ($LnPO_4$), Inorg. Chem., 2018, 57, 6252–6265.

[237] K. Binnemans, Interpretation of europium(III) spectra, Coord. Chem. Rev., 2015, 295, 1-45.

[238] S. Merlino, E. Bonaccorsi and T. Armbruster, The real structure of tobermorite 11A: normal and anomalous forms, OD character and polytypic modifications, Eur. J. Mineral., 2001, 13, 577–590.

[239] P. Mandaliev ,T. Stumpf, J. Tits, R. Dähn, C. Walther, E. Wieland, Uptake of Eu(III) by 11A ˚ tobermorite and xonotlite: A TRLFS and EXAFS study, Geochimica et Cosmochimica Acta 2011, 75, 2017–2029.

[240] P. Yu, R. J. Kirkpatrick, B. Poe, P. F. McMillan, X. Cong, Structure of Calcium Silicate Hydrate (C-S-H):Near-, Mid-, and Far-Infrared Spectroscopy, J. Am. Ceram. Soc., 1999, 82, 742–48.

[241] L.Zhang, C. Zhao, Y. Jiang, Y. Wang, W. Yang, T. Cheng, G. Zhou, Effect of sodium dodecyl benzene sulfonate on morphology and structure of calcium silicate hydrate prepared via precipitation method, Colloids and Surfaces A 2018, 540, 249–255.

[242] P. Yu,.R. J. Kirkpatrick, B. Poe, P. F. McMillan and X. Cong, Structure of Calcium Silicate Hydrate (C-S-H): Near-, Mid-, and Far-Infrared Spectroscopy, J. Am. Ceram. Soc., 1999, 82, 742–48.

[243] V. Lilkov, E. Dimitrova and O. E. Petrov, Hydration Process of Cement Containing Fluy Ash and Silica Flume: The first 24 hours, Cement and Concrete Research, 1997, 27, 577-588.

[244] R. Roulet, J. Feuz and T. Vu Duc, Stabilité des carboxylates de terres rares, III) Maléates, méthylsuccinates et malates, Helvetica Chim. Acta, 1970, 53, 1876–1879.

[245] S. N. Limaye and M. C. Saxena, Relative complexing tendencies of O-O, O-N, and O-S donor (secondary) ligands in some lanthanide-EDTA mixed-ligand complexes, Can. J. Chem., 1986, 64, 865–870.

[246] Z. Konteatis and H. G. Brittain, Stereoselectivity in Lanthanide Complexes of Malic Acid, Inorg Chim. Acta, 1980, 40, 51–57.

[247] P. G. Manning, Tartrate Complexes Of The Rare-Earth Elements: I. The D-, DL-, and meso-Tartrate Complexes Of Tb And Eu, Can. J. Chem., 1963, 41, 2557–2565.

[248] A. Skerencak-Frech, M. Trumm, D. R. Froehlich and P. J. Panak, Coordination and Thermodynamics of Trivalent Curium with Malonate at Increased Temperatures: A Spectroscopic and Quantum Chemical Study, Inorg. Chem., 2017, 56, 10172–10180.

[249] J.-M. Wolter, K. Schmeide, N. Huittinen and T. Stumpf, Cm(III) retention by calcium silicate hydrate (C-S-H) gel and secondary alteration phases in carbonate solutions with high ionic strength: A site-selective TRLFS study, Sci. Rep., 2019, 9, 14255.

Berichtsblatt

1. ISBN oder ISSN geplant als Verbundbericht	2. Berichtsart (Schlussbericht oder Veröffentlichung) Schlussbericht

3. Titel
BMWi-Verbundvorhaben
Geochemische Radionuklidrückhaltung an Zementalterationsphasen (GRaZ)
Teilprojekt G
Wechselwirkung von dreiwertigen Actiniden/Lanthaniden mit Zementadditiven und Calcium-Silikat-Hydratphasen

4. Autor(en) [Name(n), Vorname(n)]
Taube, Franziska; Acker, Margret; Zimmermann, Thomas; Drobot, Björn; Taut, Steffen; Stumpf, Thorsten

5. Abschlussdatum des Vorhabens
31.05.2020

6. Veröffentlichungsdatum
geplant 2021

7. Form der Publikation
Karlsruher Institut für Technologie, Wissenschaftliche Berichte

8. Durchführende Institution(en) (Name, Adresse)
1) TU Dresden
Sachgebiet Strahlenschutz
01062 Dresden

2) TU Dresden
Bereich für Mathematik und Naturwissenschaften
Fachbereich Chemie und Lebensmittelchemie
Professur für Radioökologie und Radiochemie
01062 Dresden

9. Ber. Nr. Durchführende Institution

10. Förderkennzeichen
02 E 11415G

11. Seitenzahl
108

12. Fördernde Institution (Name, Adresse)

Bundesministerium für Wirtschaft und Energie (BMWi)
11019 Berlin

13. Literaturangaben
249

14. Tabellen
29

15. Abbildungen
45

16. Zusätzliche Angaben

17. Vorgelegt bei (Titel, Ort, Datum)

18. Kurzfassung
Bei Kontakt mit Wasser (ein hypothetisches Störfallszenario) werden die betonbasierten Materialien in einem nuklearen Endlager über einen langen Zeitraum hinweg sich langsam auflösen. Auch die technischen Behälter können korrodieren. Während der Betondegradation wird im Nahfeld des Endlagers ein stark alkalisches und stark salzhaltiges chemisches Milieu vorherrschen, da Natrium- und Kaliumhydroxidlösungen, später Portlandit und Zementphasen aus dem Zement ausgelaugt werden. Mittlere bis hohe Ionenstärken (bis zu 4 M), die für potentielle Endlager in norddeutschen Tonformationen besonders relevant sind, sowie der Einfluss von Zementzusätzen wurden in früheren Studien zur Rückhaltung von Radionukliden an Zementalterationsphasen nicht oder nur unzureichend berücksichtigt. Im Fokus dieses Berichtes stehen spektroskopische und thermodynamische Untersuchungen zur Wechselwirkung von dreiwertigen Actiniden/Lanthaniden im ternären System An^{3+}/Ln^{3+}- Malat - Calcium-Silikat-Hydratphasen (CSH-Phasen). Malat (Salz der 2-Hydroxybernsteinsäure) ist neben Citrat und Gluconat ein typischer Vertreter von Zementadditiven auf Basis von Hydroxycarboxylaten, die als Erstarrungsverzöger wirken. CSH-Phasen sind die Hauptkomponenten von erhärtetem Zementstein und im Wesentlichen verantwortlich für die Actinidenretention. Folgende Ergebnisse wurden erzielt: Hydroxycarboxylate mit mittleren Komplexierungsstärken (Beispiel Malat, β_1^0 ~ 6) haben keinen Einfluss auf die quantitative An^{3+}/Ln^{3+}-Rückhaltung an CSH-Phasen. Die Anwesenheit von solchen Liganden führt nicht zu einer erhöhten Mobilisierung der An^{3+}/Ln^{3+}. Malat zeigt eine Ca^{2+} vermittelte schwache, *outer-sphere* Sorption, während An^{3+}/Ln^{3+} eine nahezu quantitative Sorption (*inner-sphere* Sorption) aufweisen und dabei strukturell in die CSH-Phasen eingebaut werden. Die Sorption und Inkorporation der An/Ln und des Liganden an/in die CSH-Phasen erfolgen unabhängig voneinander. Die Struktur und Kristallinität der CSH-Phasen werden durch die Anwesenheit des Liganden deutlich beeinflusst. Polycarboxylatether (Zementfließmittel) bilden ebenfalls mittelstarke 1:1 Komplexe mit An(III)/Ln(III) (K_1 ~ 4.5 bis 5.5, I = 0.1 m). Die Komplexierungsreaktionen von An^{3+}/Ln^{3+} mit (Hydroxy)carboxylaten und Polycarboxylatethern verlaufen überwiegend endotherm und entropiegetrieben. Die Enthalpie nimmt mit zunehmender Ionenstärke ab. Es scheint, dass bei höheren Ionenstärken die Komplexbildungsreaktionen durch höhere Temperaturen weniger begünstigt werden. Die thermodynamischen Standarddaten zur Komplexierung von An^{3+}/Ln^{3+} mit Malat wurden bestimmt, ein verbessertes Prozessverständnis (bis auf die molekulare Ebene) für das ternäre System An^{3+}/Ln^{3+}-Ligand-Zementphase konnte erhalten und bestehende Datenlücken geschlossen werden.

19. Schlagwörter
Zementadditive, Calcium-Silikat-Hydratphasen, Komplexierung, Sorption, Malat, dreiwertige Actinide/Lanthanide, hohe Ionenstärke, Spektroskopie, Thermodynamik und Specific Ionic Interaction Theorie (SIT), isotherme Mikro-Titrationskalorimetrie

20. Verlag

21. Preis

Document Control Sheet

1. ISBN or ISSN	2. type of document (e.g. report, publication) report

3. title
BMWi joint project
Geochemical radionuclide retention on cement alteration phases (GRaZ)
Subproject G
Interaction of trivalent actinides/lanthanides with cement additives and calcium silicate hydrate phases

4. author(s) (family name, first name(s))	5. end of project
Taube, Franziska; Acker, Margret; Zimmermann, Thomas; Drobot, Björn; Taut, Steffen; Stumpf, Thorsten	31.05.2020
	6. publication date scheduled 2021
	7. form of publication Karlsruher Institut für Technologie, Wissenschaftliche Berichte
8. performing organization(s) (name, address) 1) TU Dresden Sachgebiet Strahlenschutz 01062 Dresden 2) TU Dresden Bereich für Mathematik und Naturwissenschaften Fachbereich Chemie und Lebensmittelchemie Professur für Radioökologie und Radiochemie 01062 Dresden	9. originator's report no.
	10. reference no. 02 E 11415G
	11. no. of pages 108
12. sponsoring agency (name, address) Bundesministerium für Wirtschaft und Energie (BMWi) 11019 Berlin	13. no. of references 249
	14. no. of tables 29
	15. no. of figures 45

16. supplementary notes

17. presented at (title, place, date)

18. abstract
In case of water ingress (the hypothetical "worst case scenario") into a repository, the concrete will slowly dissolve over a long time. The technical containers may also corrode. During the concrete degradation, a highly alkaline and highly saline chemical milieu will prevail in the near field of the repository due to the leaching of sodium and potassium hydroxide solutions and later leaching of portlandite and cement phases from the cement. Medium to high ionic strengths (up to 4 M), which are particularly relevant for potential repositories in North German clay formations, as well as the influence of cement additives are not or only insufficiently considered in previous studies on the retention of radionuclides at cement alteration phases. The focus of this report is on spectroscopic and thermodynamic investigations of the interaction of trivalent actinides/lanthanides in the ternary system An^{3+}/Ln^{3+}- malate - calcium silicate hydrate phases (CSH phases). Besides citrate and gluconate, malate (salt of 2-hydroxysuccinic acid) is a typical representative of cement additives based on hydroxycarboxylates, which are used as retarders. CSH phases are the main components of hardened cement paste and are responsible for actinide retention. The following results were obtained: Hydroxycarboxylates with medium complexation strengths (example malate, β_1^0 ~ 6) have no influence on the quantitative An(III)/Ln(III) retention on CSH phases. The presence of such ligands does not result in an increased mobilization of An(III)/Ln(III). Malate shows a Ca^{2+} mediated weak outer sphere sorption, while the An(III)/Ln(III) show a nearly quantitative sorption (inner sphere sorption) and an incorporation into the CSH phases. The sorption and incorporation processes of the An(III)/Ln(III) and the ligand on/in the CSH phases occur independently of each other. The structure and crystallinity of the CSH phases are influenced by the presence of the ligand. Polycarboxylate-ethers (superplasticizer) form medium strength 1:1 complexes with An(III)/Ln(III) (K_1 ~ 4.5 bis 5.5, I = 0.1 m). Their complex strength is comparable with similar An(III)/Ln(III) complexes with naturally occurring polycarboxylates like humic substances. The complexation reactions of An(III)/Ln(III) with (hydroxy)carboxylates and polycarboxylate- ethers are mainly endothermic and entropy driven. The enthalpy decreases with increasing ionic strength. It seems that at higher ionic strengths the complex formation reactions are less favored by higher temperatures. The standard thermodynamic data on the complexation of An^{3+}/Ln^{3+}- with malate were determined, an improved process understanding (up to the molecular level) for the ternary system An^{3+}/Ln^{3+}-ligand-cement phase was obtained and existing data gaps were closed.

19. keywords
cement additives, calcium silicate hydrate phases, complexation, sorption, malate, trivalent actinides/lanthanides, high ionic strength, spectroscopy, thermodynamics and specific ionic interaction theory (SIT), isothermal micro-titration calorimetry

20. publisher	21. price